Optical and X-ray Characterization of the Magnetic Properties of Gold Capped Cobalt Nanowires Grown on Pt(997)

John Patrick Cunniffe

Student number: 05172926

20/03/11

Declaration

This thesis has been submitted to the University of Dublin for examination for the degree of Doctor in Philosophy by the undersigned.

This thesis has not been submitted as an exercise for a degree to any other university.

With the exception of the assistance noted in the acknowledgments, this thesis is entirely my own work.

I agree that the Library of the University of Dublin may lend or copy this thesis upon request.

John Cunniffe October 2010

School of Physics,

University of Dublin,

Trinity College,

Dublin

Abstract

X-ray magnetic circular dichroism (XMCD), magnetic second harmonic generation (MSHG) and reflection anisotropy spectroscopy-magneto optical Kerr effect (RAS-MOKE) studies were carried out on a range of Au-capped Co nanowires grown on a vicinal Pt(997) crystal. A four-pole electromagnet was constructed to enable RAS-MOKE measurements to be made at normal incidence. XMCD studies at the Co L-edge of six, four and three atom wide Co wires capped with three, six and nine monolayers of Au provided a range of different data: XMCD spectra were used to calculate orbit-spin moment ratios, angular dependent hysteresis measurements gave easy axis direction information, and temperature dependent studies provided qualitative information about Curie temperature and quantitative information about aspects of the magnetization dynamics of the system. While the orbit-spin moment ratios were found to agree with previously published measurements of uncapped wires, all measured samples showed ferromagnetic behaviour at substantially higher temperatures than in the uncapped case. The orbit-spin moment ratio agreement provided strong evidence that the wires had been capped without disturbing the morphology of the wire structure. The easy axis direction showed large deviations from the behaviour reported for the uncapped samples, with the easy axis aligning with the terrace normal (-6° $\pm$3° from surface normal). A superparamagnetic phase was measured on the three atom wide wire, and an interesting temperature dependence of the coercivity was seen in all samples. This was attributed to domain wall pinning, with a kink in the steps being the most likely candidate for the pinning site. Some measurements were made with 3, 6 or 9 monolayers of Au on 3 and 6 atom wide Co wires. The different capping layer thicknesses caused large changes in the relative coercivities. RAS-MOKE measurements were performed at room temperature on the six and four atom wide wires capped with 6 monolayers of Au. A field rotation method was developed to simultaneously measure the easy axis direction, coercivity and stiffness of a ferromagnetic system. While the easy axis measurements agreed with the XMCD results, the RAS-MOKE measurements found slightly larger coercivities, and significantly smaller stiffnesses than the XMCD measurements. While the difference in coercivities could be partially explained by the temperature dependence of the coercivity, no significant temperature dependence was observed in the stiffness. As a result, this difference was attributed to the difference between the two measurement techniques: while the Co

L-edge XMCD will only measure the magnetic response of the Co, the MOKE effect will also measure any induced magnetization in the Pt or Au. RAS-MOKE has been shown to be a sensitive probe of magnetic nanostructures possessing the technologically important property of perpendicular magnetic anisotropy.

MSHG studies at normal incidence detected no magnetic signal in the Co wire samples. This was attributed to the large crystallographic signal of 3m symmetry overwhelming the magnetic signal. However, some additional analysis was done on previous measurements of Au-capped Fe structures grown on a vicinal W(110) crystal. Unlike the Au/Co/Pt(997) system, there is only a single crystallographic contribution to the signal for this system, coming from the 1m symmetry steps, for normal incidence geometry. As a result, the magnetic contribution is comparable to the crystallographic one. Due to the highly symmetry dependent nature of the second harmonic response, hysteresis loops from magnetic regions of differing symmetry can be separated via careful choice of input polarization angle. In the course of this work, the results of concurrent fitting of these hysteresis loops and temperature curves are presented. For Fe coverages of 0.75 and 2 monolayers, two distinct magnetic regions were identified, each with distinct coercivities, stiffnesses and, apparently, Curie temperatures. The two regions are most likely associated with step and terrace magnetization, although this remains speculative.

Contents

List of acronyms

2D	2-Dimensional
AES	Auger Electron Spectroscopy
AFM	Atomic Force Microscopy
AMR	Anisotropic Magnetoresistance
BBO	Beta Barium Borate
EPU	Elliptical Polarization Undulator
EXAFS	Extended X-ray Absorption Fine Structure
GMR	Giant Magnetoresistance
IC	Integrated Circuit
IR	Infrared
LBO	Lithium Triborate
LEED	Low Energy Electron Diffraction
MAE	Magnetic Anisotropy Energy
ML	Monolayer
MOKE	Magneto Optical Kerr Effect
OPA	Optical Parametric Amplifier
MBE	Molecular Beam Epitaxy
MSHG	Magnetic Second Harmonic Generation
PEEM	Photoemission Electron Microscopy
PEM	Photo-Elastic Modulator
PID	Proportional-Integral-Differential
PMA	Perpendicular Magnetic Anisotropy
PMT	Photo Multiplier Tube
RAS	Reflection Anisotropy Spectroscopy
RAS-MOKE	Reflection Anisotropy Spectroscopy-Magneto Optical Kerr Effect
RegA	Regenerative Amplifier
RFA	Retarding Field Analyser
RKKY	Ruderman-Kittel-Kasuya-Yosida
SHG	Second Harmonic Generation
SMOKE	Surface Magneto Optical Kerr Effect
SNR	Signal-to-Noise Ratio
SPED	Spin Polarized Electron Diffraction

STM	Scanning Tunneling Microscopy
TMR	Tunneling Magnetoresistance
UHV	Ultra High Vacuum
UV	Ultraviolet
VSM	Vibrating Sample Magnetometry
XAS	X-ray Absorption Spectroscopy
XMCD	X-ray Magnetic Circular Dichroism
XMLD	X-ray Magnetic Linear Dichroism

1 Introduction

1.1 Magnetic nanostructures

In the past 20 years, miniaturization in industries in the area of information and communication technology (ICT) has combined with advances in analytic techniques to generate large interest in the properties and morphology of nanostructures, surfaces and interfaces. In particular, the electronic and magnetic properties of thin films and low dimensional systems are of interest for technological applications, more generally in terms of surface and size effects in shrinking existing device architecture, and in particular in future novel devices which make use of the new physics which appears in low dimensional systems.

Magnetic nanostructures are of particular interest, both in magnetic storage and in novel devices. Magnetic storage has existed in various forms for over a century, an early example being the "telegraphones" invented in 1898 by the Danish telephone engineer Valdemar Poulsen. All magnetic storage works on the same basic principle, whereby a series of magnetic domains or particles in a recording medium are magnetized in a certain direction to hold information, and this information is then read by detecting the stray field above the medium using some form of read head. While the basic principle of operation remains unchanged, magnetic storage has gone through a number of iterations over the years. In terms of recording media, the stainless steel discs of the "telegraphones" were replaced with acetate tape coated in ferromagnetic iron oxide. Tape based analogue recording has been used since the thirties for both audio and video recording, with only iterative changes to the recording medium allowing for sufficient storage densities for commercial applications. In fact, tape recording with digital recording schemes is still used in specialist high volume recording applications today. However, the introduction of digital computers in the 1970s required a digital recording solution with higher read/write speeds then possible with tape based systems. This lead to the introduction of disc based storage devices, where data is encoded on a rotating magnetic disc. The disc consists of a thin film of magnetic domains or particles which are then read from or written to by a read/write head as the disc spins underneath it.

The storage density of digital magnetic disc storage devices (where spin-up and spin-down domains are assigned as boolean zero and one respectively) has followed a similar

trend to that of transistor densities on integrated circuits, where densities roughly double every 2 years (fig 1.1). This trend has been driven by the scalability of such technologies, where transistor and magnetic domain dimensions have been progressively shrunk to yield increased performance. As the dimensions of the magnetic bits have been reduced, the read/write head has changed to keep pace. Early read/write heads were essentially small electromagnets. A write function was performed by passing current through the magnet windings, resulting in a magnetic field which switched the bit lying underneath the head. A read was performed by measuring the inductive current in the coils generated as the disc spun underneath the head. While write heads still work in essentially the same manner, read heads have been improved over the years, as the magnetic bits, and the stray field produced by them, has shrunk. Anisotropic magneto-resistance (AMR) read heads, where the impedance of the head material depended on the external magnetic field, replaced inductive read heads in 1991. These were replaced with giant magneto-resistance (GMR) heads, which took advantage of the GMR effect, which won Grunberg [1] and Fert [2] the Nobel prize in physics in 2007. This effect is seen in samples which consist of 2 ferromagnetic films separated by a non-magnetic metallic spacer layer, which results in huge changes in the electrical resistance of the stack depending on the relative magnetization states of the 2 ferromagnetic layers. Thus, if one ferromagnetic layer is pinned such that its magnetization does not change, and the other has a low enough coercivity that it can be flipped by the stray field of the magnetic bits, then a high/low resistance in the head corresponds to an up/down bit. GMR heads have given way to tunnel magneto-resistance (TMR) heads in perpendicular recording schemes.

The continual shrinkage of magnetic bit dimensions in magnetic disc drives has driven a change from longitudinal to perpendicular recording. In older hard drives, the magnetic bits had an easy axis in the plane of the recording media. This is common with magnetic thin films, as the shape anisotropy tends to force the magnetization into the plane of the film. However, such a scheme limits the areal density of bits possible on the disc, and so the switch to perpendicular magnetization, where the easy axis of the bits is normal to the plane of the recording media, was necessary to increase the storage density of these devices. However, this change put pressure on the GMR read/write heads used at that point.

Magneto-optic recording was investigated at the end of the twentieth century as a possible perpendicular storage scheme. Read functions are performed via the magneto

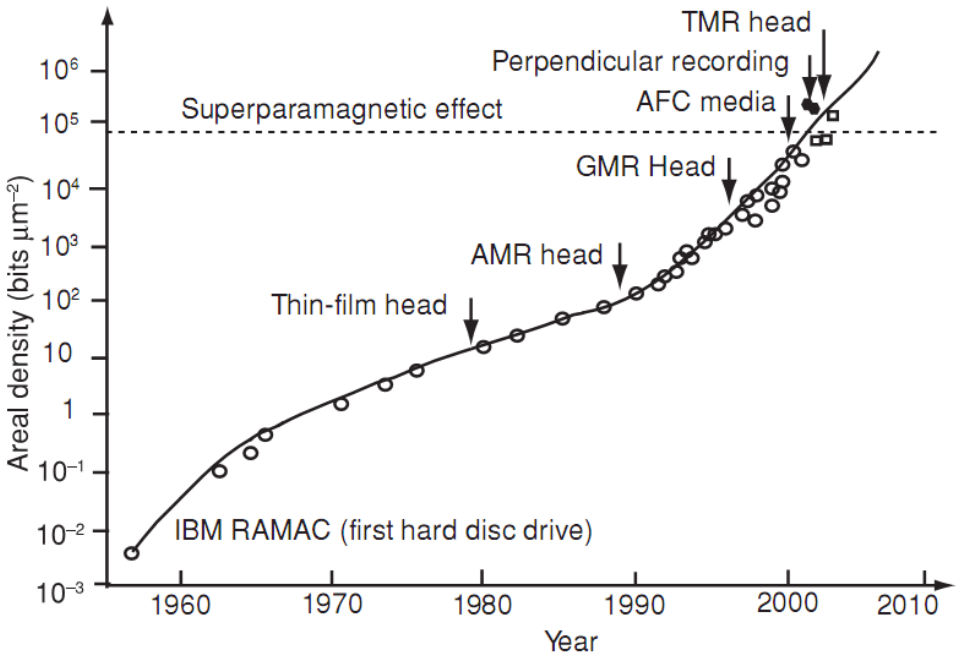

Figure 1.1: Increase of storage density in magnetic disc drives over the past 50 years, after [3].

optic Kerr effect (MOKE), whereby linearly polarized light undergoes a rotation of polarization upon reflection from a magnetized material (discussed in detail in section 2). Write functions are performed by locally heating a magnetic bit to a temperature where its coercivity is small using a pulsed laser, and then cooling again in a small magnetic field. This allows for a stable bit (with a large coercive field) which can still be written to with small magnetic fields. Magneto-optic recording was compatible with perpendicular recording schemes, which made it favourable to existing longitudinal schemes, but it was ultimately limited by the wavelength of the light used. The implementation of a perpendicular recording scheme with a TMR read head, and a soft magnetic underlayer to enhance the effect of the write head proved more efficient, and magneto-optic recording was no longer competitive.

Another area which raises interesting questions about the magnetic properties of low dimensional systems is the emerging field of spintronics. Spintronics is a proposed system of electronic devices whose function depends not only on the charge of the electron, as in existing integrated circuits (ICs), but also on the spin of the electron. The field of spintronics has arisen due to the fact that the trend of miniaturization of current IC design will eventually lead to devices where the dimensions of the active areas will approach that of a single atom. At this point, one must look in directions other than

miniaturization for further improvements in speed and energy efficiency. However, for spintronics to be viable, it is necessary to integrate magnetism and magnetic materials into the semiconductor based electronics present in modern ICs. As a result, the properties of low dimensional magnetic systems is of paramount importance to the design and fabrication of spintronic devices.

The advancement of magnetic storage technology and spintronics has driven research into the fundamental properties of magnetic thin films and low dimensional structures, which has in turn driven further technological advancements. The most obvious example of this feedback between industry and research is the previously discussed discovery of GMR, which lead to the creation of more efficient hard drive read heads. This effect was first observed in stacks consisting of two ferromagnetic iron (Fe) layers of around 10 nm thickness, separated by a chromium (Cr) or gold (Au) layer of varying thickness [1]. This study found that in the Cr case, the two Fe layers were, for certain Cr thicknesses, coupling through the Cr layer in an anti-ferromagnetic fashion. The magneto-resistance of similar stacks was later measured [2], and it was found that the electrical resistance of such structures was hugely different when the two ferromagnetic layers were ferromagnetically coupled compared to when they were anti-ferromagnetically coupled. GMR is one example of the many interesting effects that arise from studies of low dimensional magnetism, and demonstrates the possible technological applications for such systems.

When looking at the properties of low dimensional magnetic systems, it is worthwhile to consider the theory of bulk magnetization, and how it evolves in the case where the system tends towards reduced dimensionality. The Heisenberg model of magnetism, when calculated for a three dimensional lattice, predicts a quasi-particle based on a spin-wave excitation called a magnon. The number of magnons excited at a temperature T is:

$$n_m = \int_0^\infty \frac{N(\omega_q)d\omega_q}{e^{\hbar\omega_q/kT} - 1} \tag{1.1}$$

where $N(\omega_q)$ is the density of states for magnons, which varies as $\omega_q^{-1/2}$, ω_q^0 and $\omega_q^{1/2}$ for one, two and three dimensions, respectively [3]. By evaluating the integral for $x = \hbar\omega_q/kT$, we get a $T^{3/2}$ dependence, but for two or one dimensions, the integral diverges, which implies that there can be no spontaneous magnetization in a system with dimensionality lower then 3. This is the Mermin-Wagner theorem. However,

this theory does not take into account magneto-crystalline anisotropy (MAE). With the introduction of anisotropy, ferromagnetic order is possible in lower dimensional systems, as has been experimentally observed even in one-dimensional systems [4].

In order to study the effect of dimensionality on a magnetic system, thin films of the ferromagnetic elements Fe, cobalt (Co) and nickel (Ni) deposited on non-magnetic metallic substrates such as copper (Cu), tungsten (W), and platinum (Pt) have been studied extensively [5]. Two systems in particular have been widely studied due to their rich magnetic behavior and their relative ease of preparation. Fe on W(110) has been studied with a range of techniques such as Spin Polarized Electron Diffraction (SPED) and Scanning Tunneling Microscopy (STM) [6], MOKE [7], spin polarized STM [8], and Magnetic Second Harmonic Generation (MSHG) [9–13], due in part to the fact that, upon deposition of Fe in ultra high vacuum (UHV) conditions on a clean W(110) surface, a stable, well ordered, ferromagnetic monolayer of Fe(110) is obtained. On top of this, using suitable preparation conditions, Fe nanostripes can be formed on suitable vicinal offcuts of W(110) [7]. The other system to attract significant attention is that of Co on Pt(111). Similarly to the Fe/W(110) system, deposition of Co on Pt(111) substrates forms a well-ordered pseudomorphic Co(111) monolayer, as studied by Extended X-ray Absorption Fine Structure (EXAFS) techniques [14]. At coverages above $\sim$1 nm, the Co starts to relax to its bulk hexagonal close packed structure [15]. Particularly interesting in the Co/Pt(111) system is the phenomenon of perpendicular magnetic anisotropy (PMA) whereby the easy axis of a thin film is normal to the crystal surface. This effect has also been seen in, for example, Co films on Palladium (Pd) (111) substrates [16], Co/Pd multilayers [17], Ni/W electro-deposited films [18], Fe/terbium (Tb) multilayers [19], and Co films on Au [20]. For most elemental magnetic films, the shape anisotropy forces the easy axis into the plane of the film. This implies that the MAE must be significantly different in these thin film systems in order to produce the observed PMA. There is good evidence to suggest that the MAE of the interface is important here from the thickness dependence of the effect (figure 1.2), and the effect of small amounts of adatoms [20–22]. This suggests that the MAE is related to the spin-orbit coupling, which is altered at surfaces and interfaces due to the reduced coordination between adjacent magnetic atoms.

Another useful property of the Co/Pt system is that, similar to the Fe/vicW(110) system, the use of a vicinal offcut of Pt(111) as a substrate can lead to the formation of nanostripes of Co in certain temperature regimes (figure 1.3). In fact, ferromagnetism

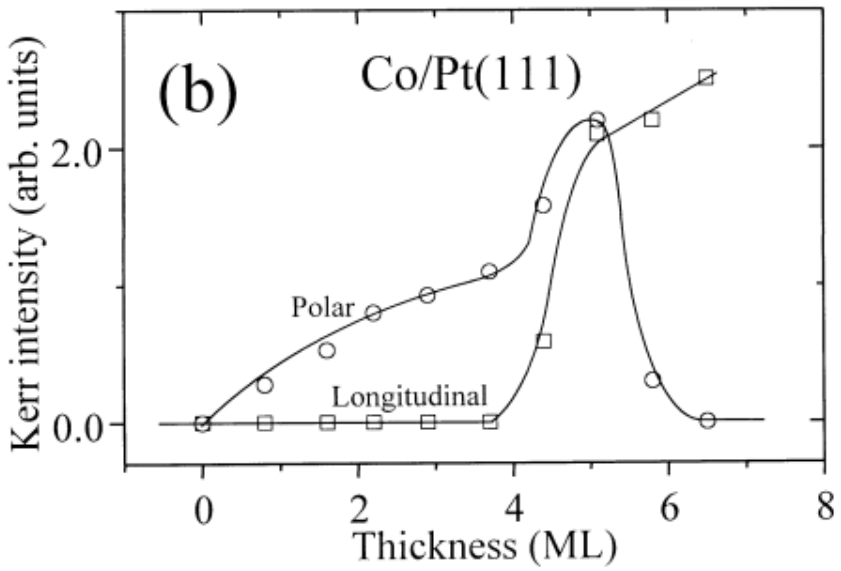

Figure 1.2: Dependence of Polar (out-of-plane) and longitudinal (in-plane) MOKE signals on Co thickness, after [21].

was recently recorded in a one atom thick wire grown on Pt(997) [4], (figure 1.4)! The magnetic anisotropy of isolated Co atoms on Pt(111) has also recently been measured [23]. As such, the Co/Pt(997) system can provide access to the very limit of any proposed magnetic storage or spintronic device, where feature sizes are comparable to that of an atom, and as such offers an opportunity to explore the limits of future technological advances.

Also of interest for future applications is the protection of these low dimensional systems, and the control of their magnetic properties. Both of these can be achieved with a non-magnetic metallic capping layer. Magnetic moments can couple over short distances through a Ruderman-Kittel-Kasuya-Yoshida (RKKY) exchange coupling mechanism. This mechanism was originally proposed as an explanation of the coupling of nuclear spin moments through conduction electrons by Ruderman and Kittel [25], and was later adapted to include electronic spin moments in ferromagnets by Kasuya [26] and Yosida [27]. The coupling that arises from RKKY is due to the fact that when free electrons are scattered from a scattering center, they will re-arrange themselves to minimize the effect of the scattering center. This applies for both spin scattering and charge scattering events, and results in a spin or charge polarization which oscillates as one moves away from the scattering center (in the case of charge scattering, these oscillations are referred to as Friedel oscillations [28]). Figure (1.6) shows the behavior of the RKKY function, $F(\xi) = (\sin\xi - \xi\cos\xi)/\xi^4)$. $\xi = 2k_f r$, where k_f is the Fermi

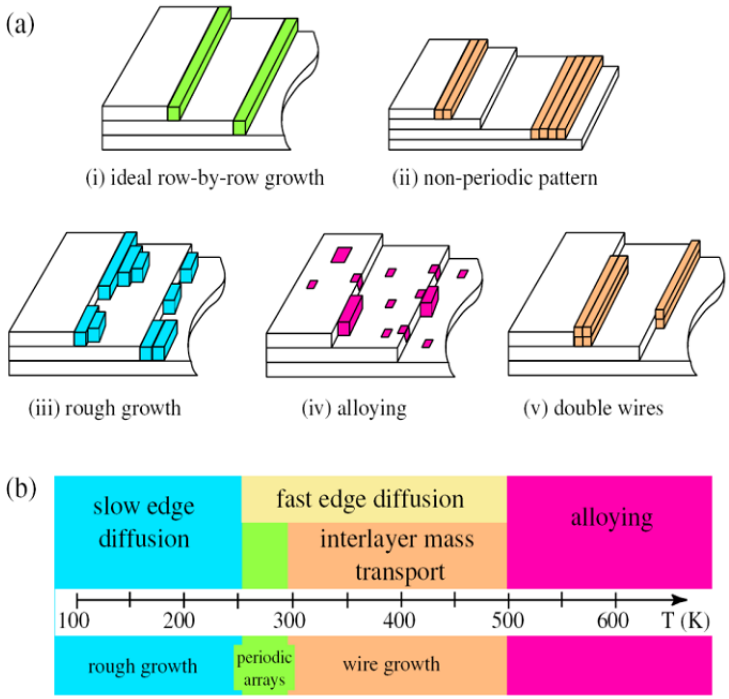

Figure 1.3: Digram of the different growth modes possible in the Co on Pt(997) system, after [23].

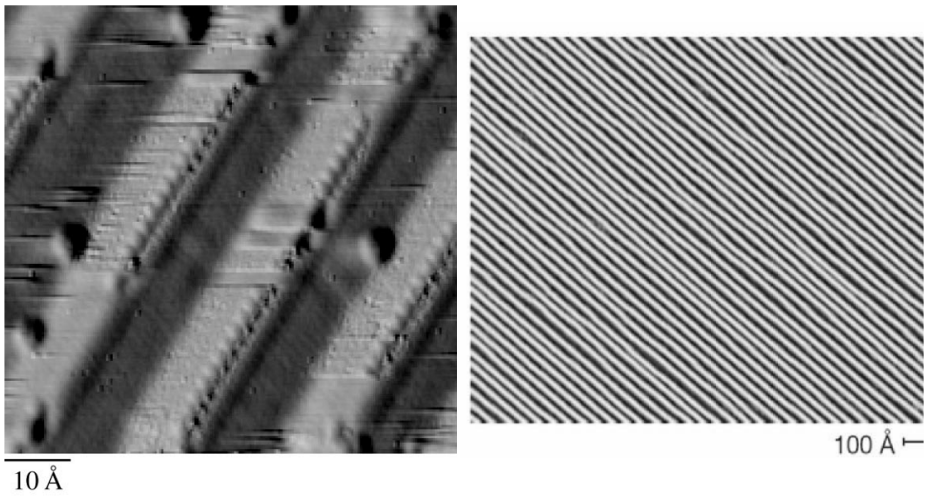

Figure 1.4: STM image of single atomic chain of Co grown on Pt(997) (left) and clean, ordered Pt(997) (right), after [24].

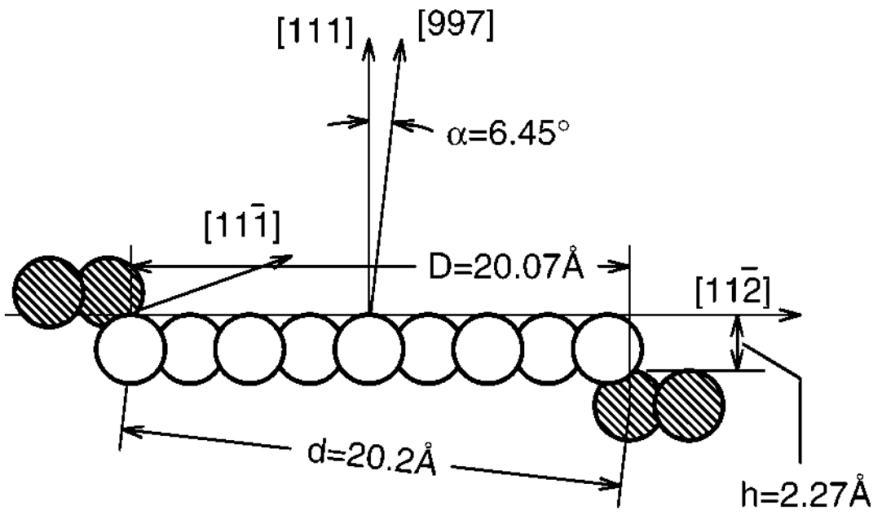

Figure 1.5: Diagram of Pt(997) surface, after [24].

wave vector and r is distance from a magnetic point impurity embedded in a non-magnetic metal. This function has been used to calculate the effect of a Cu capping layer of varying thickness on the Curie temperature of Fe and Co monolayers on a Cu substrate [29] (fig. 1.7). The effect of the capping layer thickness on the underlying magnetic layer can be understood if the capping layer is treated as a potential well. As the thickness of the layer is changed, the size of the potential well changes, as do the positions of the quantized energy levels within the well. When these energy levels approach the same energy as the Fermi energy in the magnetic layer, they contribute to the density of states at the Fermi level in the magnetic system, and as a result, enhance the magnetic properties.

As previously mentioned, recently published results showed ferromagnetism in one to four atom wide chains of Co atoms deposited on Pt(997) [4]. The results showed a non-monatomic behavior of the easy axis direction and coercivity. This work also found very low Curie temperatures and relatively large coercivities. So far, no studies have been reported on similar systems with a capping layer.

1.2 Scope of thesis

The magnetic properties of capped Fe and Co wires will be investigated. It might be expected that capping will affect both the Curie temperature and the hysteretic behavior. In addition, new approaches to characterizing these buried nanostructures will be explored. To this end, chapter 2 gives an overview of the main measurement

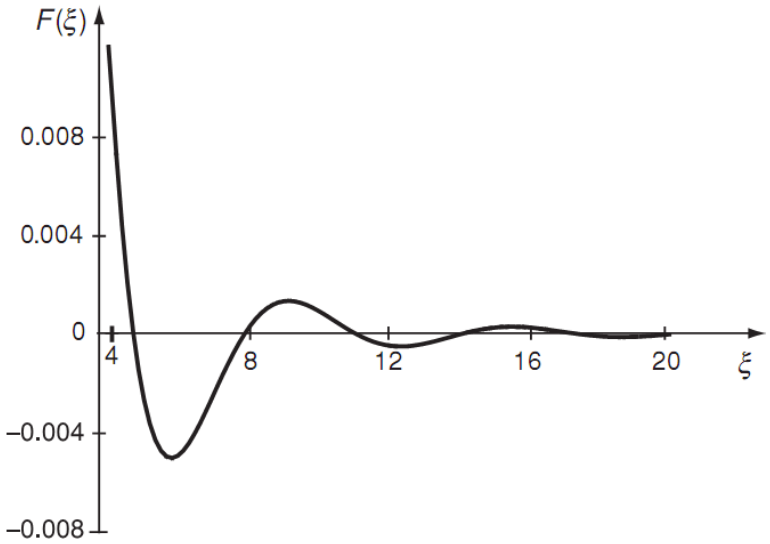

Figure 1.6: Graph of RKKY function, where $\xi = 2k_f r$, after [3].

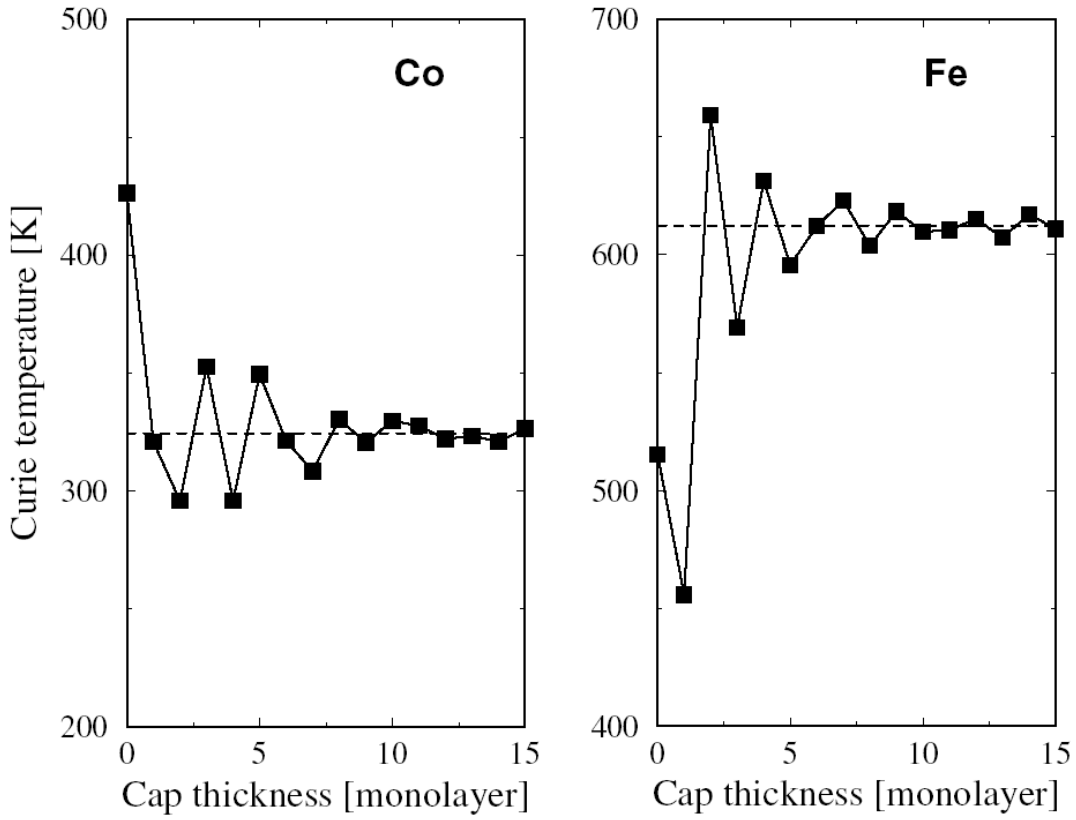

Figure 1.7: Calculated relationship between Curie temperature and capping layer thickness due to RKKY coupling for Fe and Co monolayers capped with Cu, after [29].

techniques used to characterize the samples. Chapter 3 describes the setups used for the techniques described in chapter 2, as well as describing sample preparation, and the construction and calibration of a suitable electromagnet for use with the measurement techniques. Chapter 4 presents the results of XMCD measurements of Au-capped Co nanostructures grown on Pt(997). Chapter 5 presents results of room temperature MOKE measurements of Au-capped Co nanostuctures grown on Pt(997), and compares the results to those of the XMCD measurements. Chapter 6 presents the results of MSHG measurements on Au-capped Co nanostructures grown on Pt(997), and presents extended analysis of a Au-capped Fe on W(110) system measured previously [10]. Chapter 7 provides an overview of the work presented in the thesis, and outlines further measurements which would provide useful information on the Co nanowire system.

2 Principles and phenomenology of the experimental techniques

2.1 Overview

In order to determine the magnetic properties of Au-capped Co nanowires, three main techniques will be utilized: XMCD, MSHG and MOKE. All three of these techniques use polarization dependent interactions of electromagnetic radiation with magnetic samples. While XMCD uses radiation in the energy range 50-1000 eV, both MOKE and MSHG use radiation in the optical energy range (from 1.5 eV to 5 eV). It should be noted that in discussing these techniques, a number of different parameters are discussed: in the description of MOKE, the electric permittivity, ϵ, is used to describe the interaction between light and matter, while in the description of MSHG, the susceptibility, χ, is used instead. This is purely for reasons of convention, and in fact, these two values have a close fixed relationship. In the case of X-ray measurements, ϵ approaches unity for most materials, and as such, measurements based on the resulting inelastic electronic excitations, such as electron emission yield or fluorescence yield, are preferred over reflection or transmission measurements.

2.2 X-ray magnetic circular dichroism

XMCD takes advantage of the different absorption cross-sections of circularly polarized light when the magnetization of a sample is either parallel or anti-parallel to the angular momentum vector of the light. In order to understand this interaction, and its relation to the sample magnetization, it is instructive to understand the mechanism of the absorption of an x-ray photon and the subsequent relaxation of the exited system. For the case of Co L-edge absorption, an electron is excited from a core $2p_{1/2}$ (L_2 edge) or $2p_{3/2}$ (L_3 edge) state to the conduction band. Upon relaxation of the core hole, another photon or an Auger electron can be emitted. The conduction band states that the core electron can be excited into are determined by the selection rules $\Delta l = \pm 1$ and $\Delta j = 0, \pm 1$. This gives the following allowed transitions:

$$2p_{3/2} \rightarrow 3d_{3/2}, 3d_{5/2}, 4s \tag{2.1}$$

$$2p_{1/2} \rightarrow 3d_{3/2}, 4s \tag{2.2}$$

The introduction of a magnetic moment into the system requires two more quantum numbers, m_l and m_s. Additional selection rules are then introduced depending on whether the magnetic moment and the angular momentum vector are parallel ($\Delta m_l = +1, \Delta m_s = 0$) or anti-parallel ($\Delta m_l = -1, \Delta m_s = 0$).

The cumulative rates of these transitions will determine the absorptions for the two different cases, and therefore, the dichroism. In order to simplify the analysis of these multiple transitions, a two step model has been suggested [28]. The first step is the absorption of a photon by an electron. In the process of this absorption, the x-ray angular momentum is transferred to the electron. Thus, if the angular momentum of the photon changes sign, so will the polarization state of the created photo-electron. This angular momentum is then partially transferred to the photo-electron spin through spin-orbit coupling, resulting in a photo-electron with both polarized spin and angular momentum. The second step then involves the absorption of the spin polarized photo-electron into the unoccupied conduction band of the 3d shell (figure 2.1). In order to have a high probability of the electron filling a state in the conduction band, the electron moment must be in the same direction as the sample magnetization, such that the Stoner band splitting creates a higher density of unoccupied states with the preferred values of m_l and m_s. The allowed transitions for right or left polarized light are illustrated in figure 2.2. Thus, if either the polarization of the light or the magnetization of the sample is reversed, the absorption is also reversed. The L_3 and L_2 edges have opposite responses due to the opposite nature of the spin-orbit coupling in the $2p_{3/2}$ and $2p_{1/2}$ states respectively.

The XMCD effect can be used to obtain a range of useful parameters. The observed intensity at the L_3 or L_2 edge, I, in a dichroism measurement is proportional to a number of factors:

$$I \propto P(\hat{k} \cdot \hat{M}) \tag{2.3}$$

where $\hat{M}$ is the sample magnetization, $\hat{k}$ is the x-ray wave vector, and P is the percentage polarization of the x-ray. The linear dependence of the intensity on the sample magnetization allows hysteresis loops to be measured, which gives access to information such as the coercivity, remanence magnetization and softness (discussed further in section 2.3). The dependence of the intensity on the angle between the magnetization and the x-ray wave vector allows the measurement of the easy axis direction via angle scans. XMCD also allows separation of the spin and orbital magnetization, due to the

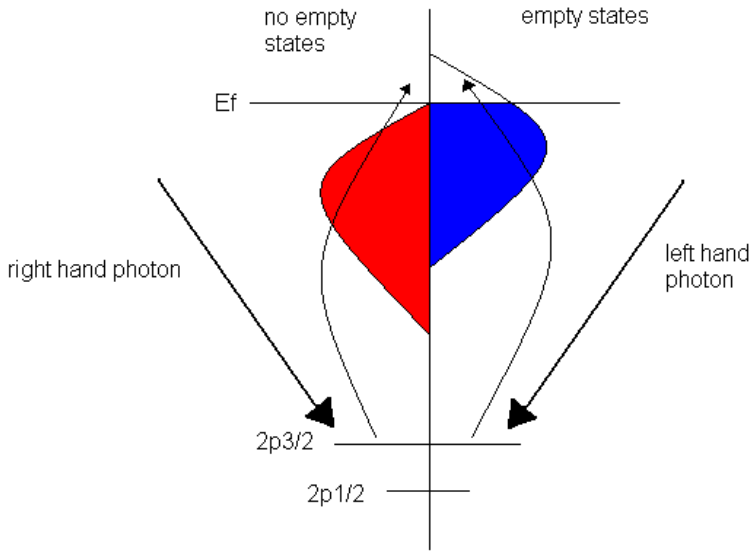

Figure 2.1: Diagram of XMCD excitation process in magnetized material. The direction of the magnetization will determine which spin-split band has empty states, and the x-ray photon polarization will determine the spin and angular moment of the excited photoelectron.

fact that they contribute in different proportions to the L_3 and L_2 edges. The spin contribution to the L_3 and L_2 edges, A_s and B_s can be written as:

$$A_s = -\frac{2}{3}.2C.\frac{\mu_s}{\mu_b}.\left(+\frac{1}{4}\right) \tag{2.4}$$

$$B_s = -\frac{1}{3}.2C.\frac{\mu_s}{\mu_b}.\left(-\frac{1}{2}\right) \tag{2.5}$$

where C is an experimentally determined constant representing the number of atoms contributing to the dichroism, μ_s is the spin magnetic moment per atom, and μ_b is the Bohr magneton. Similarly, the orbital contributions to the L_3 and L_2 edges, A_l and B_l can be written as:

$$A_l = -\frac{2}{3}.2C.\frac{\mu_l}{\mu_b}.\left(+\frac{3}{4}\right) \tag{2.6}$$

$$B_l = -\frac{1}{3}.2C.\frac{\mu_l}{\mu_b}.\left(+\frac{3}{4}\right) \tag{2.7}$$

where μ_l is the angular moment per atom. These equations can be combined to arrive at expressions for the experimentally measured total dichroism at the L_3 or L_2 edge, A or B (figure 2.3):

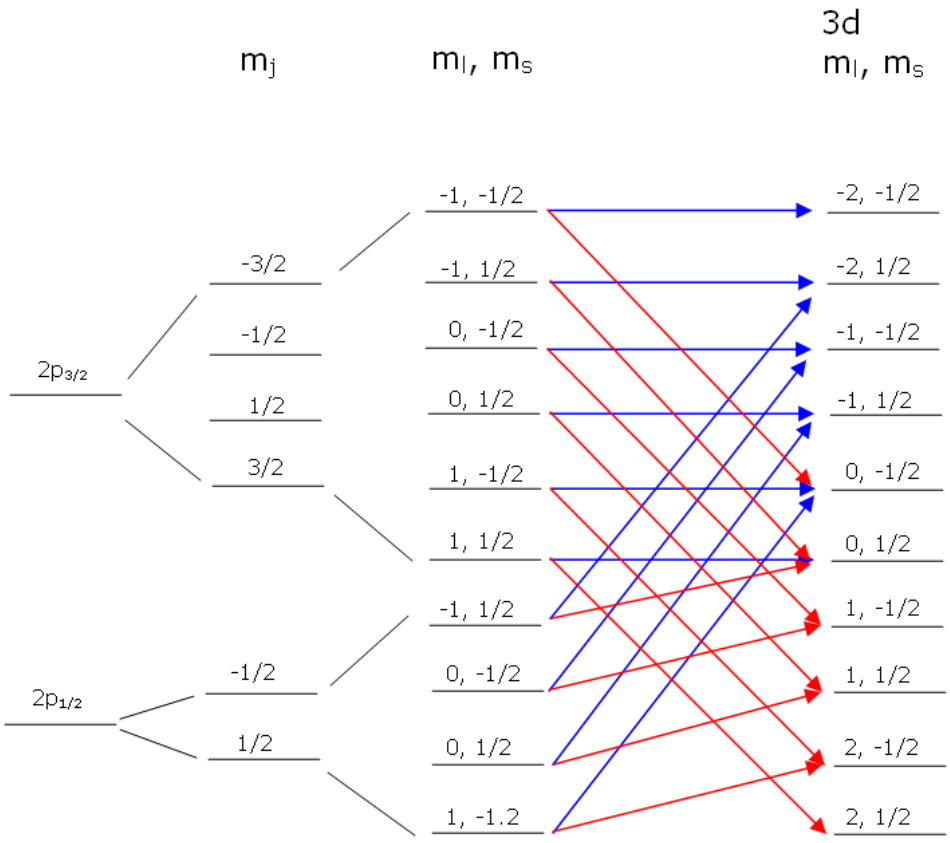

Figure 2.2: Diagram of second step of XMCD process. Red and blue arrows correspond to allowed transitions for right ($\Delta m_l = +1, \Delta m_s = 0$) and left ($\Delta m_l = -1, \Delta m_s = 0$) circularly polarized light respectively.

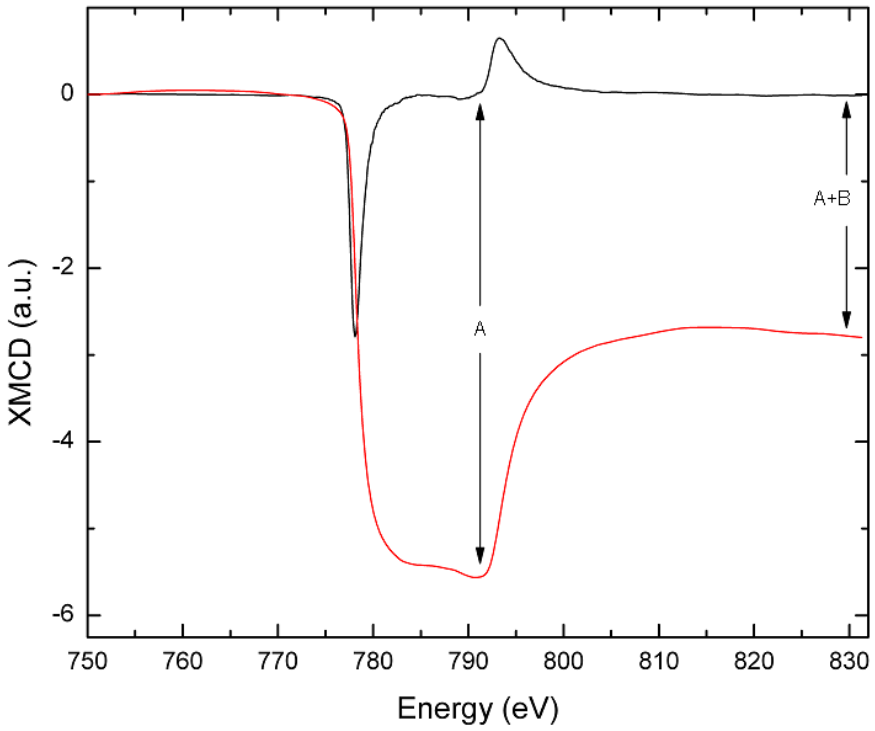

Figure 2.3: XMCD asymmetry (black) and integration of asymmetry (red). A and B are the areas of the L_3 and L_2 edges respectively, after [30].

$$A = A_s + A_l = \frac{2}{3}.2C.\left(-\frac{1}{4}.\frac{\mu_s}{\mu_b} - \frac{3}{4}.\frac{\mu_l}{\mu_b}\right) \tag{2.8}$$

$$B = B_s + B_l = \frac{1}{3}.2C.\left(+\frac{1}{2}.\frac{\mu_s}{\mu_b} + \frac{3}{4}.\frac{\mu_l}{\mu_b}\right) \tag{2.9}$$

expressed in terms of μ_s and μ_l, these equations are the XMCD sum rules:

$$\mu_s = -\frac{1}{C}.(A - 2B).\mu_b \tag{2.10}$$

$$\mu_l = -\frac{2}{3C}.(A + B).\mu_b \tag{2.11}$$

A and B can be obtained from experimental data by integrating over the L_3 and L_2 edge respectively. The XMCD asymmetry is defined as the difference between the two absorption spectra when either the magnetization direction or the photon circular polarization direction is reversed. It is thus generally unaffected by extraneous experimental signals such as unwanted backgrounds and it is then relatively easy to extract the ratio of the spin moment to the orbital moment:

$$\frac{\mu_s}{\mu_l} = \frac{3}{2}.\frac{A - 2B}{A + B} \tag{2.12}$$

Separation of the spin and orbital moments is more challenging due to the constant, C. C can be determined from the x-ray absorption scans, based on the difference in pre- and post-edge background levels. However, in any x-ray scan, there are a number of contributions to the background. Changes in the x-ray intensity can be normalized out by taking a reference signal from a gold mesh placed in the beam before the sample, but any contributions from any non-magnetic sample area can not be experimentally removed, and must be modeled. In situations where the magnetic content of the sample is small, and therefore the background is mostly that of the non-magnetic areas of the sample, it can become impossible to calculate C, and therefore impossible to separate μ_s and μ_l.

2.3 Magneto-optical Kerr effect

The term "magneto-optical Kerr effect" refers to the change in the polarization state of light reflected from a magnetic material due to the magnetization of the material. In the case of linearly polarized incident light, the magnetization causes both a rotation

(generally referred to as the Kerr rotation) in the polarization upon reflection, and a change in the ellipticity of the light (the Kerr ellipticity). Both of these components are proportional to the magnetization. As such, a MOKE measurement generally involves the measurement of the polarization state of the light reflected from a sample while the magnetization of the sample is swept from positive to negative, producing a hysteresis loop with an arbitrary y axis which is proportional to the magnetization. Since most of the interesting characteristics of a magnetic system (such as the coercivity, remanence, saturation field, softness) do not require an absolute measurement of the magnetization, this simple polarization measurement is sufficient for a wide range of applications.

The first order interaction of light with a material is described by the dielectric tensor of the material. In general, the dielectric tensor can be written as a 3×3 matrix:

$$\begin{pmatrix} \epsilon_{xx} & \epsilon_{xy} & \epsilon_{xz} \\ \epsilon_{xy} & \epsilon_{yy} & \epsilon_{yz} \\ \epsilon_{xz} & \epsilon_{yz} & \epsilon_{zz} \end{pmatrix} \tag{2.13}$$

For a non-magnetic isotropic medium, all off diagonal elements are zero and $\epsilon_{xx} = \epsilon_{yy} = \epsilon_{zz}$. In the case of a beam of light incident from a non-magnetic medium on an isotropic magnetic medium, the dielectric tensor can be generalized:

$$\epsilon = \epsilon_{xx} \begin{pmatrix} 1 & -iQm_z & iQm_y \\ iQm_z & 1 & -iQm_x \\ -iQm_y & iQm_x & 1 \end{pmatrix} \tag{2.14}$$

where m_x, m_y and m_z are the direction cosines of the magnetization vector, $\hat{M}$. Q is the Voight magneto-optical constant, which is proportional to the magnetization $\hat{M}$, and is defined as:

$$Q = i\frac{\epsilon_{xy}}{\epsilon_{xx}} \tag{2.15}$$

The reflectance of a solid is described by the Fresnel reflection matrix, obtained by solving Maxwell's equations for the dielectric tensor:

$$\hat{R} = \begin{pmatrix} r_{pp} & r_{ps} \\ r_{sp} & r_{ss} \end{pmatrix} \tag{2.16}$$

where p and s denote the component of the incident electric field in the plane and perpendicular to the optical plane of incidence respectively, and r_{ij} is the ratio of the incident j polarized electric field and reflected i polarized electric field. For simple non-magnetic materials with spherical symmetry, r_{ps} and r_{sp} are zero. r_{pp}, r_{ss}, r_{ps} and

r_{sp} can be expressed in terms of the angle of incidence θ_0, the angle of refraction in the magnetic medium θ_1, and the complex refractive indices of the non-magnetic and magnetic medium, n_0 and n_1:

$$r_{pp} = \frac{n_1 \cos\theta_0 - n_0 \cos\theta_1}{n_1 \cos\theta_0 + n_0 \cos\theta_1} - \frac{i2n_0 n_1 \cos\theta_0 \sin\theta_1 m_x Q}{n_1 \cos\theta_0 + n_0 \cos\theta_1} \tag{2.17}$$

$$r_{ss} = \frac{n_0 \cos\theta_0 - n_1 \cos\theta_1}{n_0 \cos\theta_0 + n_1 \cos\theta_1} \tag{2.18}$$

$$r_{sp} = \frac{in_0 n_1 \cos\theta_0 (m_z \cos\theta_1 + m_y \sin\theta_1) Q}{(n_1 \cos\theta_0 + n_0 \cos\theta_1)(n_0 \cos\theta_0 + n_1 \cos\theta_1) \cos\theta_1} \tag{2.19}$$

$$r_{ps} = \frac{in_0 n_1 \cos\theta_0 (m_z \cos\theta_1 - m_y \sin\theta_1) Q}{(n_1 \cos\theta_0 + n_0 \cos\theta_1)(n_0 \cos\theta_0 + n_1 \cos\theta_1) \cos\theta_1} \tag{2.20}$$

The complex Kerr rotations for incident p and s oriented waves, θ_K^p and θ_K^s, are defined as:

$$\theta_K^p = r_{sp}/r_{pp} \tag{2.21}$$

$$\theta_K^s = r_{ps}/r_{ss} \tag{2.22}$$

By substituting for r_{sp}, r_{ps}, r_{ss} and r_{pp}, we get expressions for the Kerr response for an arbitrary magnetization direction and angle of incidence. Three simple geometries for MOKE measurements can be identified (figure 2.4), which differ only in the direction of the magnetization in relation to the plane of incidence: polar ($m_z = 1, m_y = m_x = 0$), longitudinal ($m_y = 1, m_z = m_x = 0$) and transverse ($m_x = 1, m_y = m_z = 0$). Expressions for the complex Kerr rotations can then be obtained for the commonly used polar and longitudinal cases by substitution into equations 2.21 and 2.22:

$$(\theta_K^p)^{pol.} = \frac{\cos\theta_0}{\cos(\theta_0 + \theta_1)} \cdot \frac{in_0 n_1 Q}{(n_1^2 - n_0^2)} \tag{2.23}$$

$$(\theta_K^s)^{pol.} = \frac{\cos\theta_0}{\cos(\theta_0 - \theta_1)} \cdot \frac{in_0 n_1 Q}{(n_1^2 - n_0^2)} \tag{2.24}$$

$$(\theta_K^p)^{long.} = \frac{\cos\theta_0 \tan\theta_1}{\cos(\theta_0 + \theta_1)} \cdot \frac{in_0 n_1 Q}{(n_1^2 - n_0^2)} \tag{2.25}$$

$$(\theta_K^s)^{long.} = \frac{\cos\theta_0 \tan\theta_1}{\cos(\theta_0 - \theta_1)} \cdot \frac{in_0 n_1 Q}{(n_1^2 - n_0^2)} \tag{2.26}$$

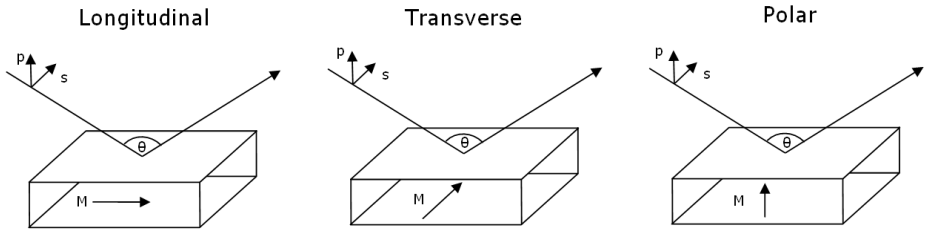

Figure 2.4: Diagram of the three common MOKE geometries.

There are a number of important observations which can be made from this analysis. The first is that, at normal incidence, only the polar component of the magnetization is probed. This is due to the fact that all of the m_x and m_y terms in the reflection matrix appear with a $\sin\theta_1$ term. This is equivalent to the $\hat{k} \cdot \hat{M}$ dependence seen in the XMCD signal in section 2.2. The second observation is that at normal incidence, $\theta_K^p = \theta_K^s$:

$$\theta_K^p = \theta_K^s = \frac{in_0 n_1 Q}{(n_1^2 - n_0^2)} \tag{2.27}$$

The importance of these normal incidence properties to the current work will become apparent in section 3.5. The third observation is that in all cases, the Kerr rotation is proportional to the sample magnetization. While the above formalism applies only to an optically thick magnetic film, it is useful for showing the broad dependencies of the Kerr signal on experimental factors. A full multilayer system has been described by Zak *et al.* [31, 32] using medium boundary matrices and medium propagation matrices to account for multiple reflections. However, the only significant phenomenological addition of the full calculation is the introduction of the wavelength of the incident light and the refractive indices of the additional layers.

Due to the proportionality between the measured Kerr rotation and the sample magnetization it is possible to extract useful information from hysteresis loops measured using the Kerr effect, an example of which is shown in figure 2.5. In many cases Kerr loops can be fitted, assuming centrosymmetric loops, to a sigmoidal equation of the form:

$$M^{\pm}(H) = -M_{sat} + \frac{2M_{sat}}{1 + exp[-s(H \mp H_c)]} \tag{2.28}$$

where $M^+(H)$ has the applied magnetic field increasing from an initial negative value, and conversely for $M^-(H)$, M_{sat} is the saturation magnetization, s is the stiffness, and H_c is the coercivity. The remanence magnetization can be expressed as the magnetization at zero field as a percentage of the saturation magnetization, which removes the

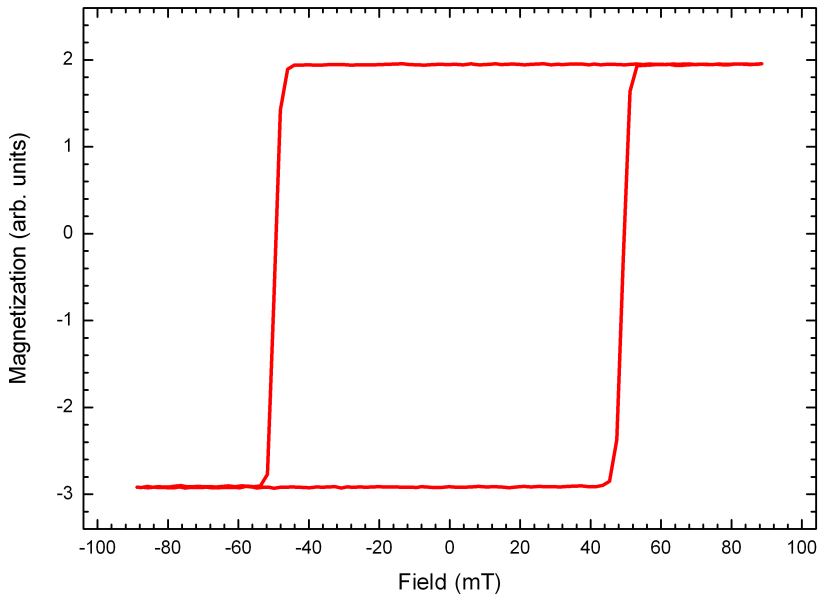

Figure 2.5: Example of a MOKE loop from a thin Co film. The y axis is in arbitrary units which are proportional to the Kerr ellipticity.

need for an absolute magnetization measurement. The same methodology can be used for hysteresis loops measured via XMCD.

In the consideration of the MOKE measurement, we have considered samples which are isotropic i.e. $\epsilon_{xx} = \epsilon_{yy} = \epsilon_{zz}$. The MOKE measurements in this study are conducted using a reflection anisotropy spectroscopy (RAS) setup. RAS is a normal incidence spectroscopic polarization measurement which is usually used to measure systems where $\epsilon_{xx} \neq \epsilon_{yy}$, and ϵ_{zz} is effectively zero due to the normal incidence geometry. However, the effect of the inequality of ϵ_{xx} and ϵ_{yy} on the polarization of light upon reflection is the same as in MOKE - the light polarization goes through a complex rotation upon reflection. Thus, for the Fresnel reflection matrix in a RAS measurement, on an anisotropic, non-magnetic surface at normal incidence, $r_{ps} = r_{sp} = 0$, and r_{pp} and r_{ss} become dependent on the orientation of the anisotropic axes of the surface. These complex Fresnel reflection coefficients are replaced with r_x and r_y, with the RAS signal defined in terms of r_x, r_y and the mean reflectance, $r = r_x + r_y$:

$$RAS = \frac{2(r_x - r_y)}{r_x + r_y} = \frac{\Delta r}{r} \tag{2.29}$$

Although there are a number of ways to measure the RAS signal, one popular method is the use of a photo-elastic modulator (PEM). The use of a PEM for both RAS and MOKE has been described elsewhere [33, 34]. Briefly, using the Jones matrix formalism, and assuming normal incidence, the light traveling through the measurement setup

passes through a polarizer, a PEM, reflects from the sample, and passes an analyzer polarizer. The effect of these components on the amplitude of a plane polarized light wave (A) can be described as:

$$A \propto \begin{pmatrix} 1 & 0 \\ 0 & 0 \end{pmatrix} \begin{pmatrix} \cos\left(\frac{\Gamma}{2}\right) & i\sin\left(\frac{\Gamma}{2}\right) \\ i\sin\left(\frac{\Gamma}{2}\right) & \cos\left(\frac{\Gamma}{2}\right) \end{pmatrix} \begin{pmatrix} r_x & 0 \\ 0 & r_y \end{pmatrix} \begin{pmatrix} 1 \\ 1 \end{pmatrix} \tag{2.30}$$

where $\Gamma = \Gamma_0 \sin(\omega t)$ is the retardation caused by the PEM, and r_x and r_y are Fresnel reflection coefficients which are not equal in the presence of magnetization or reflectance anisotropy. It follows that the I, the intensity of light at the detector, is a harmonic series $I_0 + I_\omega + I_{2\omega}$....., where I_0 is time-independent and the remaining terms are root-mean-square oscillations at the angular frequencies indicated in sub-scripts. Setting Γ_0 to 2.405 radians ensures $J_0(\Gamma_0) = 0$, where J_n is a Bessel function of order n, and leads to

$$\frac{I_{n\omega}}{I_0} = \frac{2J_n(\Gamma_0)Im[\Delta r/r]}{1 + |\Delta r/r|^2/4} \approx 2J_n(\Gamma_0)Im\left[\frac{\Delta r}{r}\right] \tag{2.31}$$

where n is an odd integer, and

$$\frac{I_{n\omega}}{I_0} = \frac{2J_n(\Gamma_0)Re[\Delta r/r]}{1 + |\Delta r/r|^2/4} \approx 2J_n(\Gamma_0)Re\left[\frac{\Delta r}{r}\right] \tag{2.32}$$

where n is an even integer. Thus, a lock-in amplifier can be used to obtain the first and second harmonic signals, which correspond to the real and imaginary parts on the complex rotation the light has undergone. This rotation contains both magnetic and structural information; however, the magnetic part will only change in response to changes in the sample magnetization, and the structural part will only change if the sample is rotated with respect to the instrument. These properties can be used to separate structural (RAS) responses from magnetic (MOKE) responses.

2.4 Second Harmonic Generation

In general terms, the interaction of an electromagnetic wave with a solid can be described in terms of a polarization amplitude, P, induced in the solid by the incident electric field:

$$P(\omega, 2\omega, ...) = \epsilon_0 \left[\chi^{(1)}.E(\omega) + \chi^{(2)}.E^2(\omega) + \chi^{(3)}.E^3(\omega) + ...\right] \tag{2.33}$$

where the radiated intensity, $I \propto |P|^2$. While linear techniques are governed by the first order susceptibility tensor, $\chi^{(1)}$, three wave mixing processes such as SHG are

governed by the second order optical susceptibility tensor, $\chi^{(2)}$. SHG is a special case of three wave mixing whereby $E_j = E_k$, and as a result, the third rank susceptibility tensor can be written as a 6×3 matrix. Thus, the polarization due to the SHG at the surface of a crystal can be described as

$$\begin{pmatrix} P_x \\ P_y \\ P_z \end{pmatrix} = \epsilon_0 \begin{pmatrix} \chi^{(2)}_{xxx} & \chi^{(2)}_{xyy} & \chi^{(2)}_{xzz} & \chi^{(2)}_{xzy} & \chi^{(2)}_{xzx} & \chi^{(2)}_{xxy} \\ \chi^{(2)}_{yxx} & \chi^{(2)}_{yyy} & \chi^{(2)}_{yzz} & \chi^{(2)}_{yzy} & \chi^{(2)}_{yzx} & \chi^{(2)}_{yxy} \\ \chi^{(2)}_{zxx} & \chi^{(2)}_{zyy} & \chi^{(2)}_{zzz} & \chi^{(2)}_{zzy} & \chi^{(2)}_{zzx} & \chi^{(2)}_{zxy} \end{pmatrix} \begin{pmatrix} E_x(\omega))E_x(\omega) \\ E_y(\omega)E_y(\omega) \\ E_z(\omega)E_z(\omega) \\ 2E_z(\omega)E_y(\omega) \\ 2E_z(\omega)E_x(\omega) \\ 2E_x(\omega)E_y(\omega) \end{pmatrix} \tag{2.34}$$

Equation 2.34 is general, and simplifies based on the geometry of the measurement and the symmetry of the system being probed. For the 2D point groups, figure 2.7 lists the non-zero $\chi^{(2)}$ components. However, in real experiments there are a range of other factors to take into account before modeling of the system is possible. Sipe *et al.* [35] have provided a detailed phenomenological model of the SHG response on reflection which includes electric dipole and quadrupole contributions from both the surface and the bulk, Fresnel factors etc. to provide equations for the SHG response of a (110), (111) or (001) cubic crystal face, E_{mn}, where m is the output polarization and n is the input polarization, with an angle ψ between the plane of incidence and the crystal x axis, in vacuum:

$$E_{pp}(2\omega) = (a_1 + c_1 \cos\kappa\psi)E_p^2(\omega)A_p \tag{2.35}$$

$$E_{ps}(2\omega) = (a_2 + c_2 \cos\kappa\psi)E_s^2(\omega)A_p \tag{2.36}$$

$$E_{sp}(2\omega) = (b_1 \sin\kappa\psi)E_p^2(\omega)A_s \tag{2.37}$$

$$E_{ss}(2\omega) = (b_2 \sin\kappa\psi)E_s^2(\omega)A_s \tag{2.38}$$

The a_i terms represent both bulk and surface isotropic contributions, b_i and c_i are bulk and surface anisotropic contributions, A_i are Fresnel coefficients, and κ is a symmetry related constant (which is 3 in the case of the (111) face). All coefficients have been tabulated for (110), (111) or (001) faces by Sipe *et al.* [35].

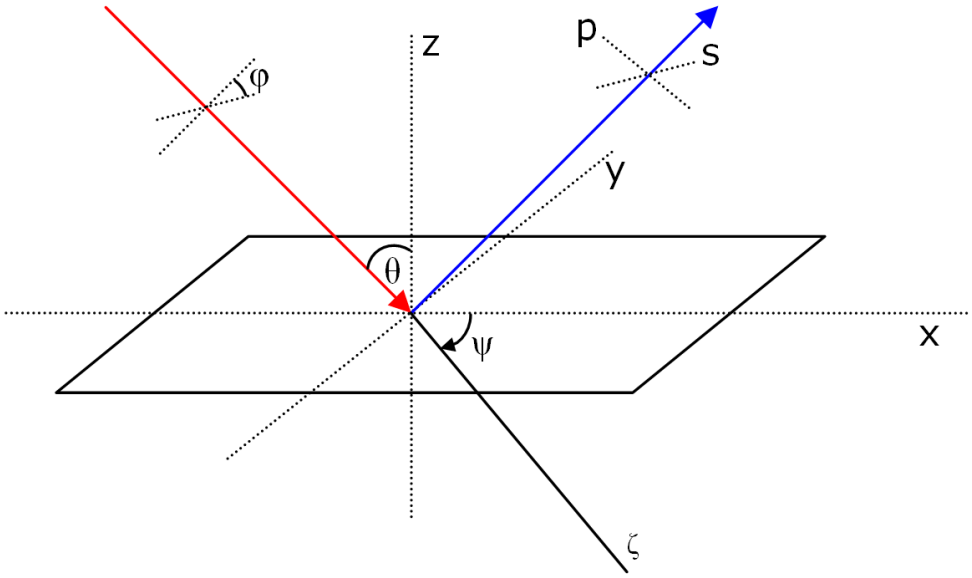

Figure 2.6: Diagram of SHG geometry. θ is the angle of incidence, φ is the angle between the incident polarization vector and the x axis and ψ is the angle between the x axis and the major symmetry axis of the sample, ζ.

The above equations provide a phenomenological model for a sample rotation measurement on a centrosymmetric crystal face at an arbitrary angle of incidence. Since the bulk and surface χ components are mixed into arbitrary coefficients, however, it is necessary to verify that bulk contributions are negligible, in which case it is possible to replace the arbitrary coefficients with χ components. Sample rotation measurements, while useful, can be problematic in certain situations (i.e. when the sample is in a cryostat or vacuum chamber). In these instances, it can be useful to explore a geometry where the input polarization is rotated. In this instance, the incident electric field can be described in terms of an angle, φ:

$$\begin{pmatrix} E_x(\omega) \\ E_y(\omega) \\ E_z(\omega) \end{pmatrix} = \begin{pmatrix} a\cos\varphi \\ b\sin\varphi \\ c\cos\varphi \end{pmatrix} E(\omega) \tag{2.39}$$

where a, b, and c are Fresnel coefficients. The p and s components of the reflected SH wave, $E_p(2\omega)$ and $E_s(2\omega)$, can then be written as:

$$E_p(2\omega) = (A\cos^2\varphi + B\sin^2\varphi + C\sin 2\varphi)E(\omega)^2 \tag{2.40}$$

Symmetry class	Independent non-zero elements of χ^{s}_{ijk}
1	*xxx, xxy, xyy, yxx, yxy, yyy, xxz, xyz, yxz, yyz, zxx, zxy, zyy, xzz, yzz, zxz, zyz, zzz*
1m	*xxx, xyy, xzz, xzx, yzy, yxy, zxx, zyy, zxz, zzz*
2	*xzx, xyz, yxz, yzy, zxx, zyy, zxy, zzz*
2mm	*xzx, yzy, zxx, zyy, zzz*
3	*xxx = -xyy = -yyx , yyy = -yxx = -xyx , yzy = xzx , zxx = zyy , xyz = -yxz , zzz*
3m	*xxx = -xyy = -yxy , xzx = yzy , zxx = zyy , zzz*
4, 6, ∞	*xxz = yyz , zxx = zyy , xyz = -yxz , zzz*
4mm, 6mm, ∞m	*xxz = yyz , zxx = zyy , zzz*

Figure 2.7: Independent non-zero elements of $\chi^{(2)}$ for a range of symmetry classes.

$$E_s(2\omega) = (F\cos^2\varphi + G\sin^2\varphi + H\sin 2\varphi)E(\omega)^2 \tag{2.41}$$

where A, B, C, F, G and H are functions of χ and the Fresnel coefficients. Further simplification is possible when a normal incidence geometry is used, as the Fresnel coefficients become simple scaling factors, and all z dependent χ components become zero.

The second order tensor elements are highly symmetry dependent. In the case of a bulk centrosymmetric system, all dipole contributions to $\chi^{(2)}$ are zero, and only when the centrosymmetry is broken (at surfaces and interfaces) is there a non-zero dipole contribution. The response of the surface or interface is also highly symmetry dependent, with the contributing elements of $\chi^{(2)}$ determined by the point group of the surface or interface (figure 2.7). While it is possible that higher order quadrupolar contributions from the bulk may appear in the signal, they should be, at worst, of similar magnitude to that of the surface dipole response [36]. A similar argument can be made for the magnetic response discussed later, since magnetism, as an axial vector, also has no bulk dipolar contribution in a centrosymmetric system.

The introduction of a magnetization to the system introduces a second magnetiza-

tion induced second order susceptibility tensor, χ^M_{ijkL}. The total SH response from the system is then the sum of the crystallographic (χ^C_{ijk}) and magnetic (χ^M_{ijkL}) contributions:

$$P(2\omega, M) = \left[\chi^C_{ijk}.E^2(\omega) + \chi^M_{ijkL}.E^2(\omega).M\right] \tag{2.42}$$

The capitalization of L indicates that this tensor index relates to the magnetization direction. While, initially, the introduction of a fourth rank tensor may appear to massively complicate measurements, similar arguments to those used in the crystallographic case reduces the number of contributing tensor components. For instance, if the magnetization is along a principle axis of the system, many of the tensor elements are zero; with polar magnetization, only χ^M_{ijkZ} elements will contribute. Carroll *et al.* [10] used a normal incidence polarization rotation geometry to measure the MSHG response from capped Fe nanostripes on vicinal W(110). Due to the symmetry of the system and the geometry of the measurement, the response consisted of three components; χ^C_{yxy}, χ^M_{yxxX} and χ^M_{yyyX}, as the easy axis of the system was in the x-direction. Since at normal incidence, Fresnel factors become scaling components, they can be included in these effective tensor components. Further isolation of components is possible when one looks at the dependence of the y polarized response on the angle between the incident polarization and the x direction, φ [10]:

$$I_y(2\omega, \varphi, \pm M_x) \propto \left|\chi^C_{yxy} \sin 2\varphi \pm \left\{\chi^M_{yxxX} \cos^2\varphi + \chi^M_{yyyX} \sin^2\varphi\right\} M_x\right|^2 \tag{2.43}$$

Since all three components have different dependencies on φ, it is possible to probe the two different magnetic components separately by choosing a value of φ and doing hysteresis measurements. The presence of two magnetic tensor components is significant in that these will help to distinguish different magnetic regions at the surface or interface, in contrast to linear techniques with a single magneto-optic coefficient.

However, unlike hysteresis loops taken via MOKE or XMCD, the change in MSHG intensity is not linearly proportional to the magnetization. This means that a methodology for extracting the hysteresis loops is required. Looking again at equation 2.43, it is obvious that there will be terms which are dependent on both M and M^2. In general, the magnetic contribution will be small relative to the crystallographic contribution, and as such, the quadratic term can be neglected. However, the signal-to-noise ratio

(SNR) of loops measured in this way is inherently limited because the intensity is dominated by the non-magnetic crystallographic contribution. In certain systems, however, specific measurement geometries can result in the magnetic and crystallographic terms being of similar magnitude. While this will increase the SNR, a method of dealing with the quadratic term is then required. To this end, we must look at the more general form of equation 2.43. Since $I \propto P^2$, equation 2.42 gives:

$$I(2\omega, M_L) \propto \left| \chi^{eff}_{even} E(\omega)E(\omega) + \chi^{eff}_{odd} E(\omega)E(\omega)M(H) \right|^2 \tag{2.44}$$

Squaring out gives:

$$I(2\omega, M_L) = |\chi^{eff}_{even}|^2 + \{|\chi^{eff}_{odd}|M_L\}^2 + 2|\chi^{eff}_{even}|\{|\chi^{eff}_{odd}|M_L\}\cos\delta \tag{2.45}$$

Where δ is the phase difference between the even crystallographic and the odd magnetic contributions. Reversal of the magnetization thus produces a phase shift of π, which has been experimentally observed for a multilayer system [37]. Solving for $|\chi^{eff}_{odd} M_L|$ gives:

$$\{|\chi_{odd}|M\} = -\gamma \pm \sqrt{I(M) + \gamma^2 - |\chi_{even}|^2} \tag{2.46}$$

Where *eff* and L are dropped for simplicity, $\gamma = |\chi_{even}|\cos\delta$ and the root is real. In a general system, the hysteresis curve can be deduced from this expression if $|\chi_{even}|$ and δ are known. For a system where the saturation magnetization is equal and opposite when the field is reversed, these values can be calculated from measured data:

$$\gamma = \frac{1}{2}\sqrt{I^{sat+} - I^{tp}} - \sqrt{I^{sat-} - I^{tp}},\ \tan\delta = \frac{\sqrt{I^{tp}}}{\gamma} \tag{2.47}$$

Where $I^{sat\pm}$ are the saturation intensities and I^{tp} is the intensity at the turning point of the MSHG curve (see figure 2.8). Thus a quantitative extraction is possible where a turning point can be identified, and χ_{even} and δ can also be determined. In the case of a small relative magnetic term, where the quadratic term can be neglected, symmetric saturation conditions give:

$$|\chi_{odd}|M\cos\delta = \frac{I(M) - \frac{1}{2}(I^{sat+} + I^{sat-})}{\sqrt{2(I^{sat+} + I^{sat-})}} \tag{2.48}$$

This expression is equivalent to previous linearized expressions [38]. In an intermediate case, where the magnetic contribution is large enough such that the quadratic term cannot be excluded, but the MSHG intensity does not show a turning point, a simple approximation is where $I^{tp} = 0$, giving:

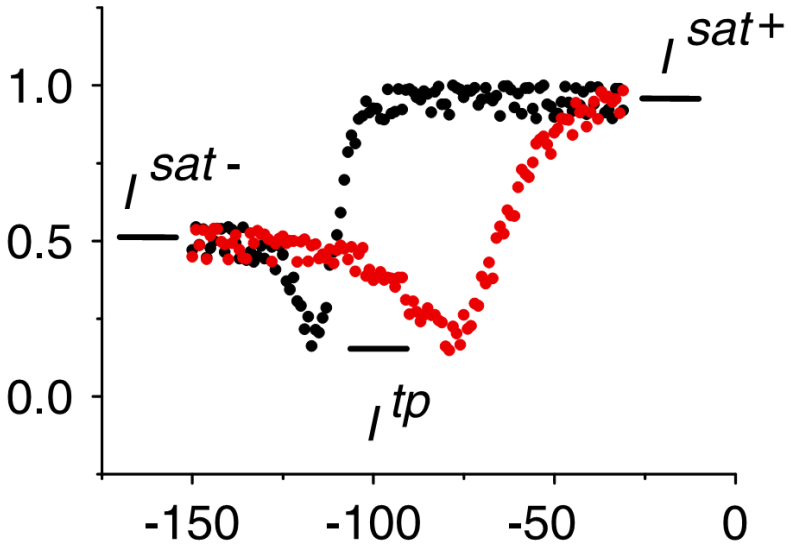

Figure 2.8: Example of shape of magnetization curves obtained via MSHG when the quadratic term is large relative to the crystallographic term.

$$\gamma = \frac{1}{2}\sqrt{I^{sat+}} + \sqrt{I^{sat-}},\ |\chi_{even}| = \gamma \tag{2.49}$$

Another, simpler method of extracting the loop is to assume a symmetric, non-biased hysteresis loop. In such a case, one can remove the quadratic effect by decomposing the hysteresis curve into a right-hand curve, where the applied field, H is increasing from an initial negative value, and a left hand curve, where H is decreasing from an initial positive value. These curves can be described as:

$$I^{\pm}(2\omega, H) = |\chi_{even}|^2 + \{|\chi_{odd}|M^{\pm}(H)\}^2 + 2|\chi_{even}|\{|\chi_{odd}|M^{\pm}(H)\}\cos\delta \tag{2.50}$$

Where the superscript + and - refer to the right-hand and left-hand curves, respectively. For centrosymmetric loops, $M^{+}(H) = -M^{-}(H)$. Applying this identity gives:

$$I^{\pm}(2\omega, H) = |\chi_{even}|^2 + \{|\chi_{odd}|M^{\mp}(-H)\}^2 + 2|\chi_{even}|\{|\chi_{odd}|M^{\mp}(-H)\}\cos\delta \tag{2.51}$$

it follows that:

$$I^{\mp}(2\omega, -H) = |\chi_{even}|^2 + \{|\chi_{odd}|M^{\pm}(H)\}^2 + 2|\chi_{even}|\{|\chi_{odd}|M^{\pm}(H)\}\cos\delta \tag{2.52}$$

Subtracting the expression for $I^{\mp}(2\omega, -H)$ from $I^{\pm}(2\omega, H)$ gives:

$$I^{\pm}(2\omega, H) - I^{\mp}(2\omega, -H) = 4|\chi_{even}|\{|\chi_{odd}|M^{\pm}(H)\}\cos\delta \tag{2.53}$$

And hence:

$$M^{\pm}(H) \propto I^{\pm}(2\omega, H) - I^{\mp}(2\omega, -H) \tag{2.54}$$

This shows, under the assumption that the hysteresis behaviour is centrosymmetric, that the loop can be extracted by subtracting the right-hand curve from the left-hand curve. This removes the quadratic term, leaving only the linear cross term. This method, while less general, is a quicker way of extracting hysteresis data from MSHG magnetization curves.

3 Experimental details

3.1 Overview

This chapter discusses techniques used in sample preparation, and experimental details for the principal measurement techniques used during the course of the work.

3.2 Sample preparation

The majority of the work in this thesis was carried out on two circular 99.9996% purity Pt(997) crystals of 8 mm diameter and 1 mm thickness, aligned to 0.1° and polished at 0.03 μm roughness. The samples were mounted on tungsten wire of 0.25 mm diameter via two cylindrical holes cut in the crystals by the manufacturer (Surface Preparation Laboratory, Zaandam, The Netherlands). An additional hole is used to insert a type R thermocouple in order to measure sample temperature. The thermocouple was read out to a computer via an isolated thermocouple amplifier (Keithley MB37-R). The samples were then mounted on a sample holder on the end of a manipulator by spot welding the tungsten wire to two molybdenum rods, which formed part of the sample holder (figure 3.1). Sample heating was performed via radiative heating from a tungsten filament mounted less than 1 mm behind the sample. The manipulator was then mounted in a UHV system for processing.

Sample preparation involved two main processes: sample cleaning and deposition. Sample cleaning was achieved using a combination of argon ion etching and annealing. The ion etching was used to remove unwanted contaminants e.g. C, O, or S, and the annealing step was used to recrystallize the sample surface, to form a well ordered periodic stepped structure, and to remove damage caused during the ion etching process. The cleanliness of the sample was characterised using an Omicron Spectaleed four grid LEED/Auger electron spectroscopy (AES) system (Omicron Nanotechnology GmbH, Taunusstein, Germany). LEED and AES are standard surface science techniques for characterizing surfaces in UHV conditions. Both derive their surface sensitivity from the fact that the mean free path of 10-1000 eV electrons for most solids is $\sim$1 nm. LEED involves measuring the spatial distribution of electrons which are coherently elastically backscattered from the sample surface. Since the wavelength of a 150 eV electron is about 0.1 nm, which is of the order of the atomic spacing, the electrons undergo Bragg diffraction from the sample, and the backscattered electrons form an

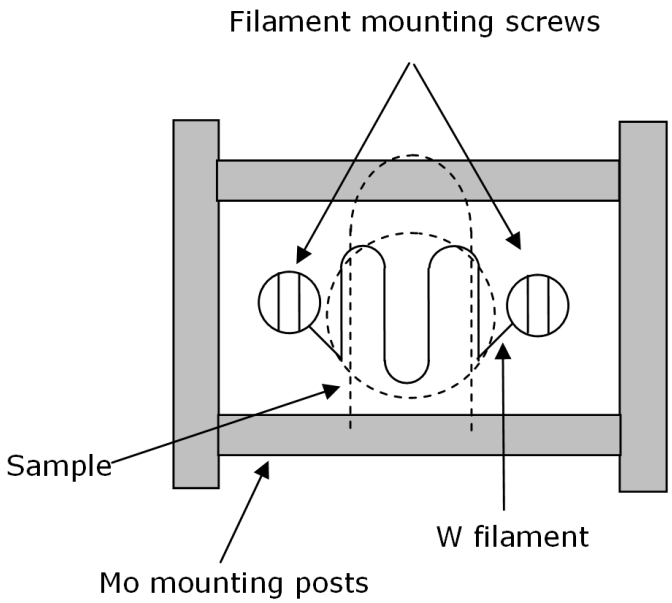

Figure 3.1: Diagram of the sample holder. The sample is mounted above the filament by spot welding the tungsten mounting wires to the molybdenum mounting rods. The entire assembly is mounted on a stainless steel plate and attached to the end of the manipulator.

image of the surface crystallographic point group in inverse space.

AES involves bombarding the sample with electrons with an energy of 3 keV, and detecting electrons emitted from the sample as a result of the decay of the core hole created by the incident electron beam. These electrons have kinetic energies characteristic of among other things, the electronic states of the atoms emitting the electrons, and thus provide information on the elemental composition of the surface.

The rear view Spectaleed system consists of an electron gun mounted in the center of a retarding field analyser (RFA) and a phosphor screen. For LEED measurements, electrons with energies between 20 and 250 eV are typically used, and the back-scattered electrons are accelerated towards a phosphor screen by a high positive voltage at the screen. For the AES measurements, the electron gun is set to a fixed energy of 3000 eV, and a modulating voltage of 1-10 V peak to peak is applied to the middle grids. The second derivative of the secondary electron yield is then measured using a lock-in amplifier for a range of energies. The resolution and signal-to-noise ratio can be adjusted by changing the modulating voltage, and the gain and time-constant of the lock-in amplifier.

In order to clean the sample, the vacuum chamber was backfilled to 5×10^{-6} mbar of argon via a leak valve on the ion gun and the sample was cycled between 10 minute

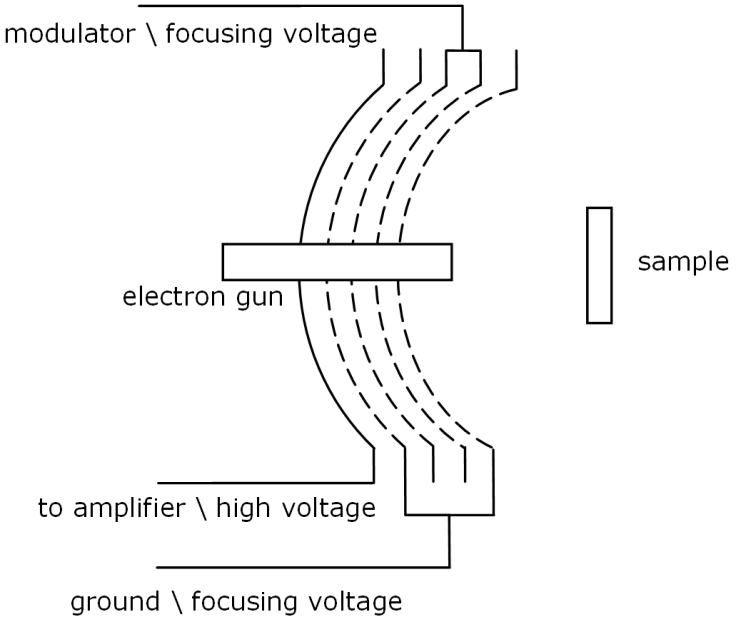

Figure 3.2: Diagram of Spectaleed system. The grids perform different functions depending on whether an AES or LEED measurement is required.

sputter sessions at 750 K with a beam energy of 500 eV, and 20 minute annealing sessions at 850 K. A Labview program was written to control the process, using the voltage output of the R-type thermocouple mounted in the sample to calibrate sample temperature. This process was repeated until the Auger spectrum showed only peaks attributed to Pt (figure 3.3) and the LEED pattern showed a sharp six-fold pattern with step-induced spot splitting (figure 3.4).

Once the sample was clean, Co and Au were deposited using two high temperature Knudsen cells supplied by MBE Komponenten (Dr. Eberl MBE-Komponenten GmbH, Weil der Stadt, Germany) (figure 3.5). The cells consisted of a polycrystalline Al_2O_3 crucible suspended in a tungsten filament assembly, which is then encased in a water cooled shroud. A tungsten shutter mounted on a rotary feed-through allows the cell to be opened and closed to the sample, and the filament current was controlled via a PID controller and a C-type thermocouple mounted close to the crucible. Cell deposition rates were calibrated via deposition onto a quartz crystal oscillator, which was moved close to the sample position on a linear translation drive. In order to deposit areas of different thicknesses onto a single crystal, a stainless steel flag was mounted on a stepper motor driven linear translation drive, and was moved in front of portions of the sample as needed. For the majority of the measurements, 2 different crystals were prepared with varying coverages of Co and Au (figure 3.6). Figure 3.7 shows a LEED

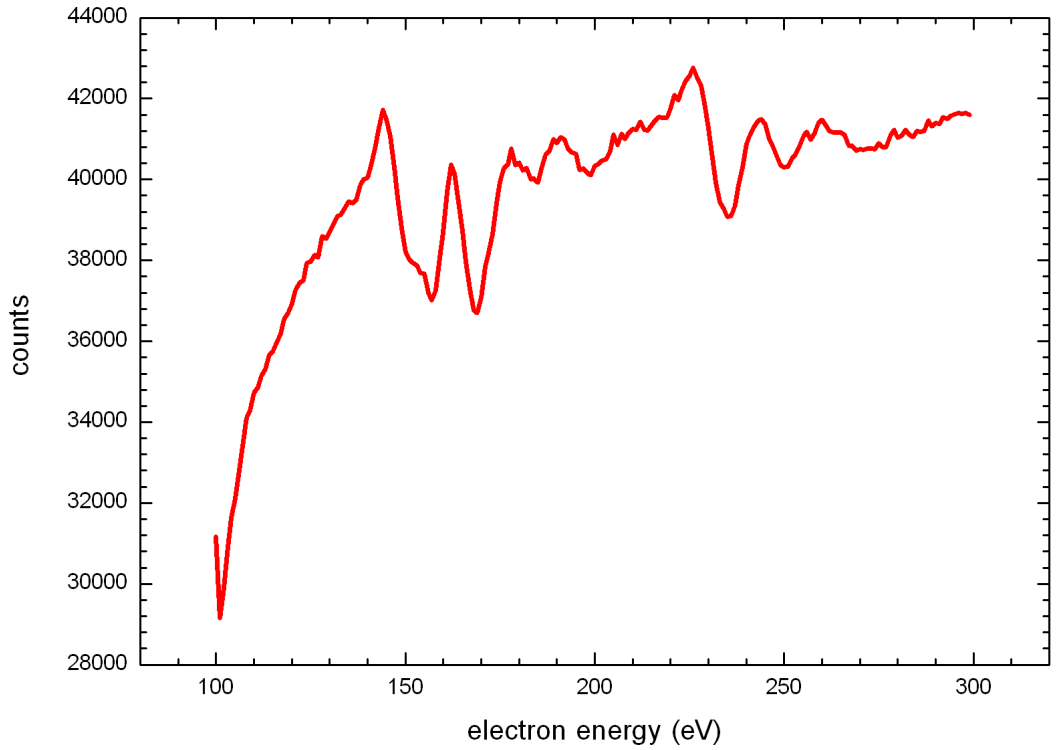

Figure 3.3: AES of clean Pt(997), from 100-300 eV. All peaks are attributed to Pt via reference spectra [39].

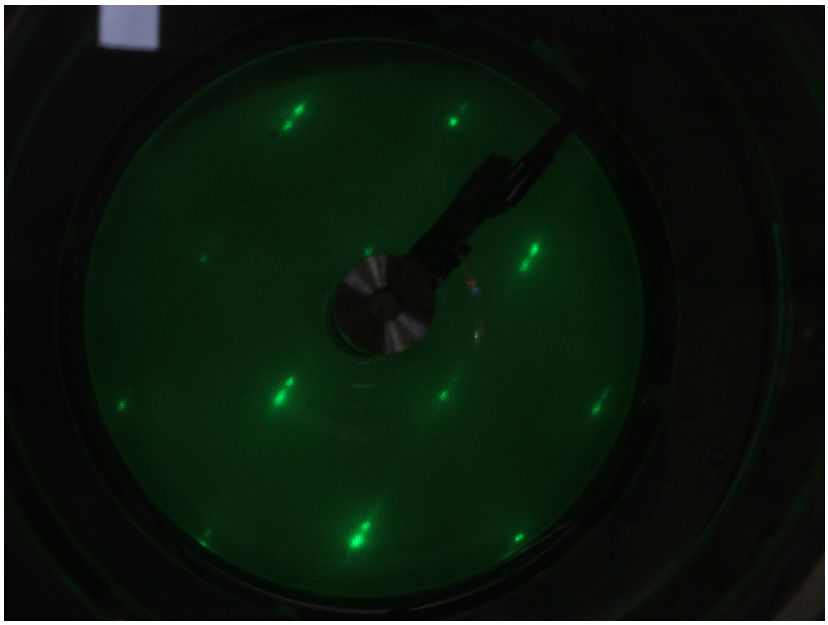

Figure 3.4: LEED image of clean, well-ordered Pt(997) crystal

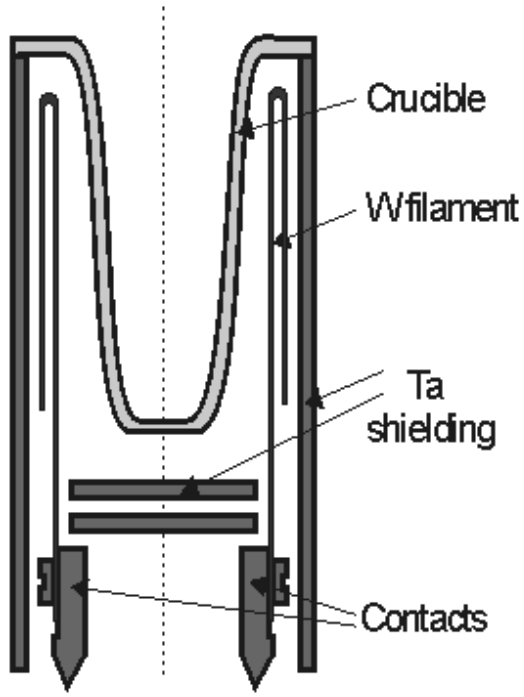

Figure 3.5: Diagram of a high temperature MBE cell (Dr. Eberl MBE-Komponenten GmbH, Weil der Stadt, Germany)

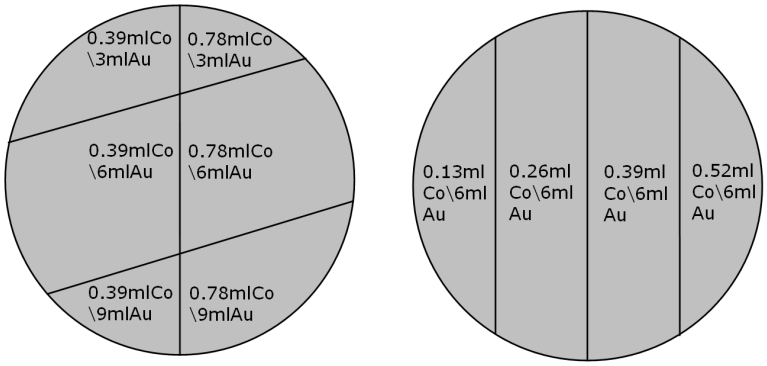

Figure 3.6: Diagram of the main samples used in the measurements. 0.13ml of Co on Pt(997) corresponds to a single atom thick wire.

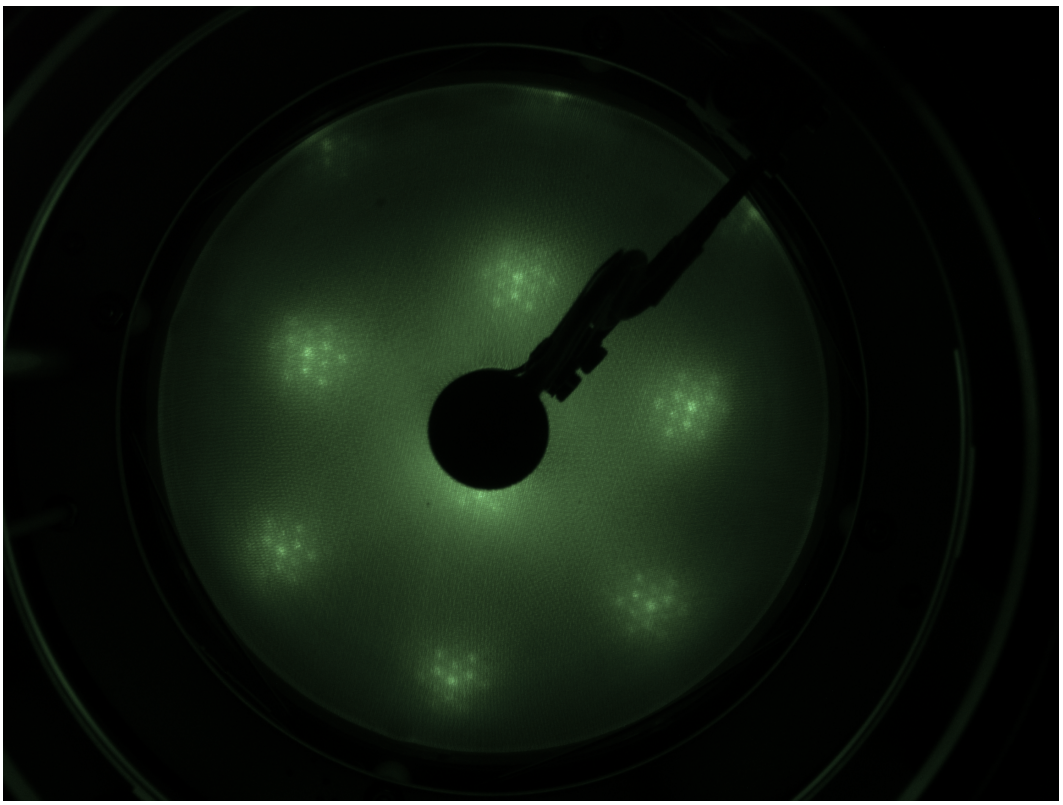

Figure 3.7: LEED image of two monolayers of Co deposited on Pt(111), taken at 121 eV. Image shows Co satellite spots around Pt(111) spots, consistent with [40].

image of a two monolayer Co film deposited on a clean Pt(111) crystal. The image mirrors published results [40], suggesting a clean well ordered Co film, with a lattice constant of bulk Co, as expected at this coverage. Figure 3.8 shows a LEED image from a 9mlAu/0.78MLCo/Pt(997) sample. The relatively sharp spots and step induced spot splitting, even in the presence of a high backround, suggest a relatively ordered capping layer, even with nearly a monolayer of Co between the substrate Pt and the Au capping layer.

3.3 Quadrupole electromagnet

In order to apply an external magnetic field to samples while measuring either the MOKE or MSHG response, some form of variable magnet was required. There were two main choices in this respect: a permanent magnet based system, such as a double Halbach cylinder, or an electromagnet of some form. The permanent magnet systems have the advantage of relatively large achievable field (up to ~ 1.5 T). The major downsides to permanent magnet systems are twofold: they are relatively expensive, and due to the bulk of these systems, sample access is limited. Conversely, while electromagnets

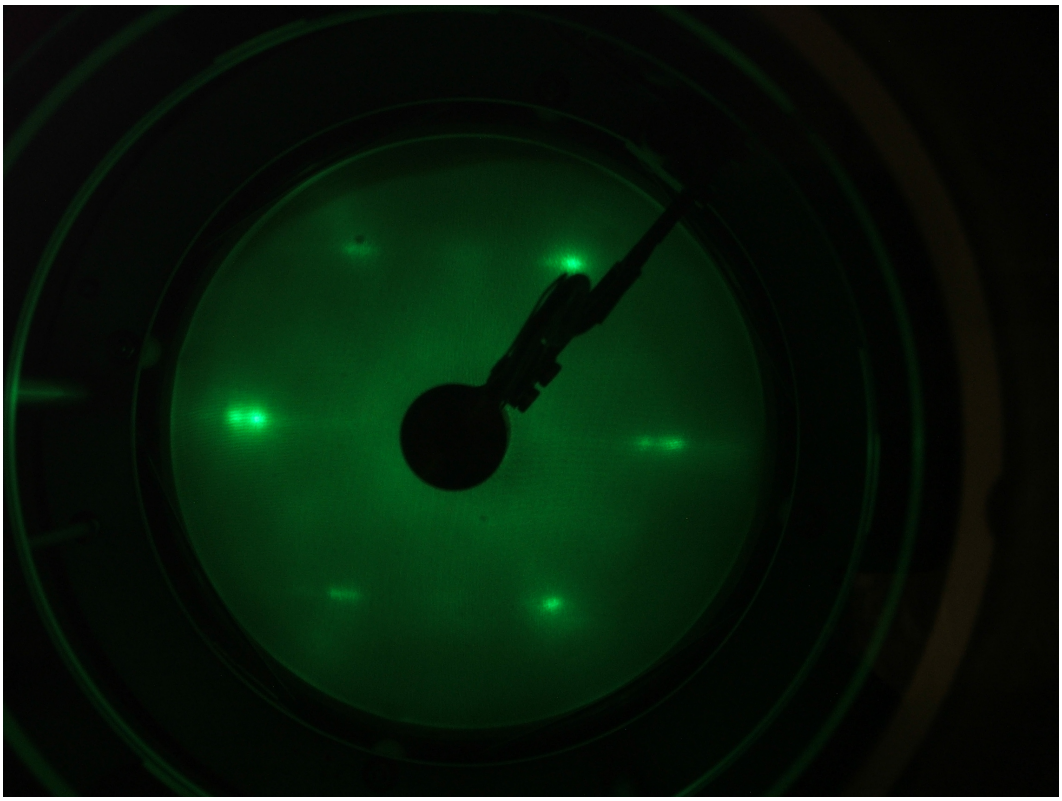

Figure 3.8: LEED image of Pt(997) crystal with 0.78 ML of Co followed by 9 ML of Au, taken at 166 eV. Image shows sharp (111) spots and step induced spot splitting, suggesting an ordered Au overlayer.

can only achieve limited fields without requiring water cooling or restrictively small air gaps, they can be built from relatively cheap materials, in geometries that allow for adequate sample access for the chosen measurement techniques.

For samples consisting of capped Co nanowires, the requirements were that measurements be made in a normal incidence geometry, with a relatively large air gap. To this end, a quadrupole electromagnet was built (figure 3.9). This design had the advantage of being relatively cheap, computer controllable, and flexible enough to rotate the magnetic field without any mechanical movement which might disturb measurements. The magnet consisted of four soft iron pole pieces mounted on a soft iron cross piece. Eight separate coils were wound on plastic coil formers. Each coil consisted of 400 turns of 1.2 mm diameter enamel insulated copper wire. The coils were then mounted on the magnet poles. Each pole pair had an air gap of 40 mm. A pair of computer controlled power supplies were used to energize the coils (Delta Elektronika ES030-10). Each power supply powered 4 coils, or 1600 turns of wire. The constructed magnet was then calibrated with a Hall probe (figure 3.10). The uniform area of the magnet was also checked by translating the Hall probe in three orthogonal directions for a fixed coil current. It was found that the field was within ± 1 mT for a cube of 4 mm^3 volume in the center of the magnet (figure 3.11).

In order to control the magnet, a program was written in Labview. The program calculated the currents required to obtain a given field magnitude and direction based on the calibration curves shown in figure 3.10. The program was then tested by requesting a rotating field of fixed magnitude and measuring the response of a Hall probe in the center of the magnet. Since the Hall probe measured the component of the magnetic field in one direction, a cosine shaped curve was measured (figure 3.12). Due to the remanence of the soft iron used for the pole pieces, certain requested angles resulted in anomalies, which were taken into account during subsequent measurements. It should be noted that, due to the hysteretic behaviour of the applied field induced by the soft iron pole pieces, a direct field measurement is always preferable, particularly in the low field limit (figure 3.13).

3.4 XMCD

The XMCD work was recorded at two different beamlines: D1011 on the MAX-II ring at MAXLAB in Lund, Sweden and beamline 4.0.2 at the advanced light source (ALS)

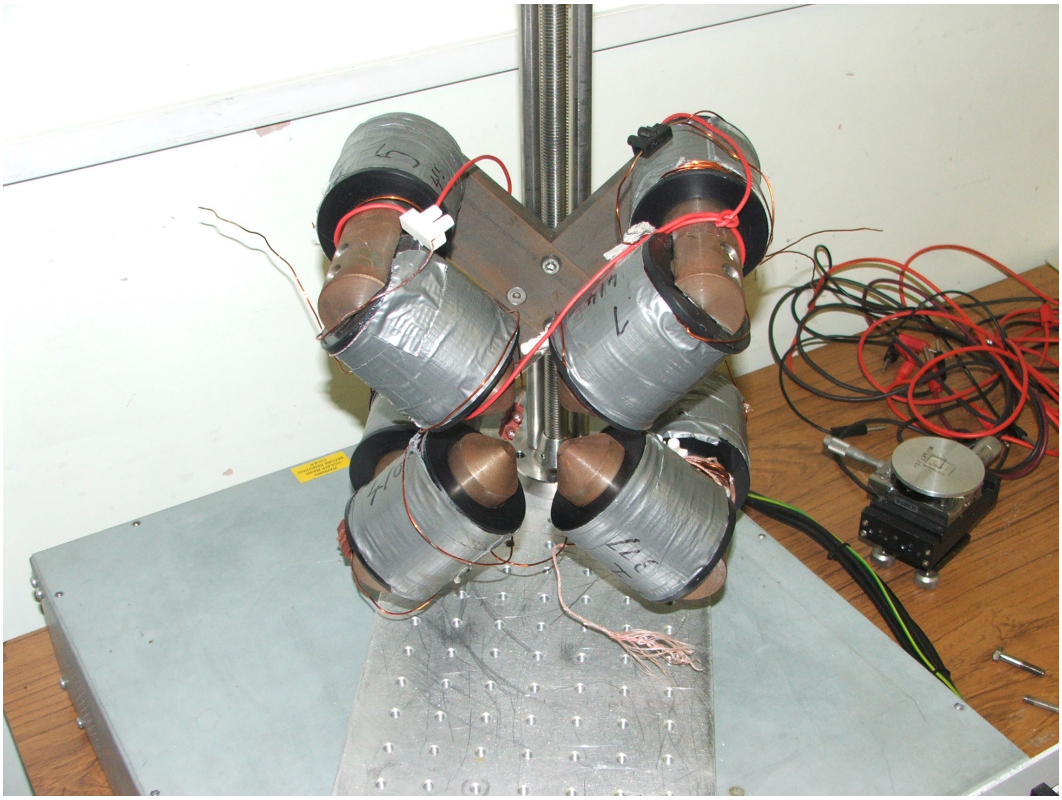

Figure 3.9: Picture of quadrupole electromagnet.

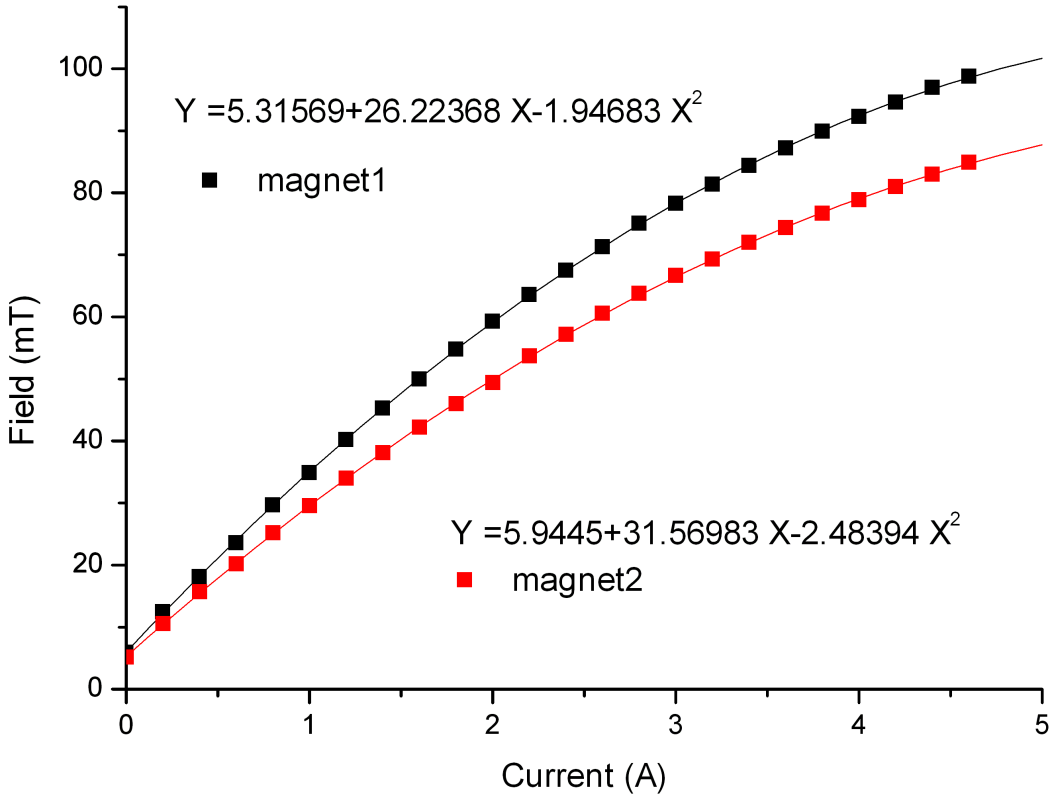

Figure 3.10: Calibration curves for two separate magnets in four pole magnet. Solid lines correspond to polynomial fits of data.

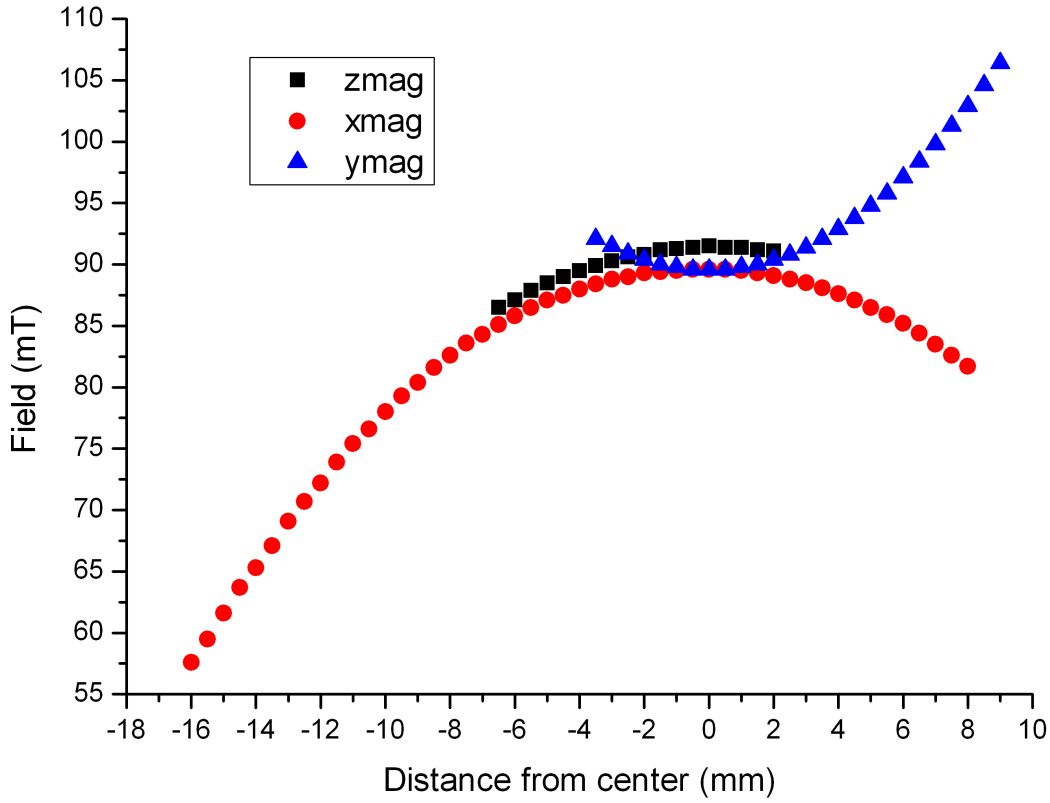

Figure 3.11: Magnet uniformity in three orthogonal directions.

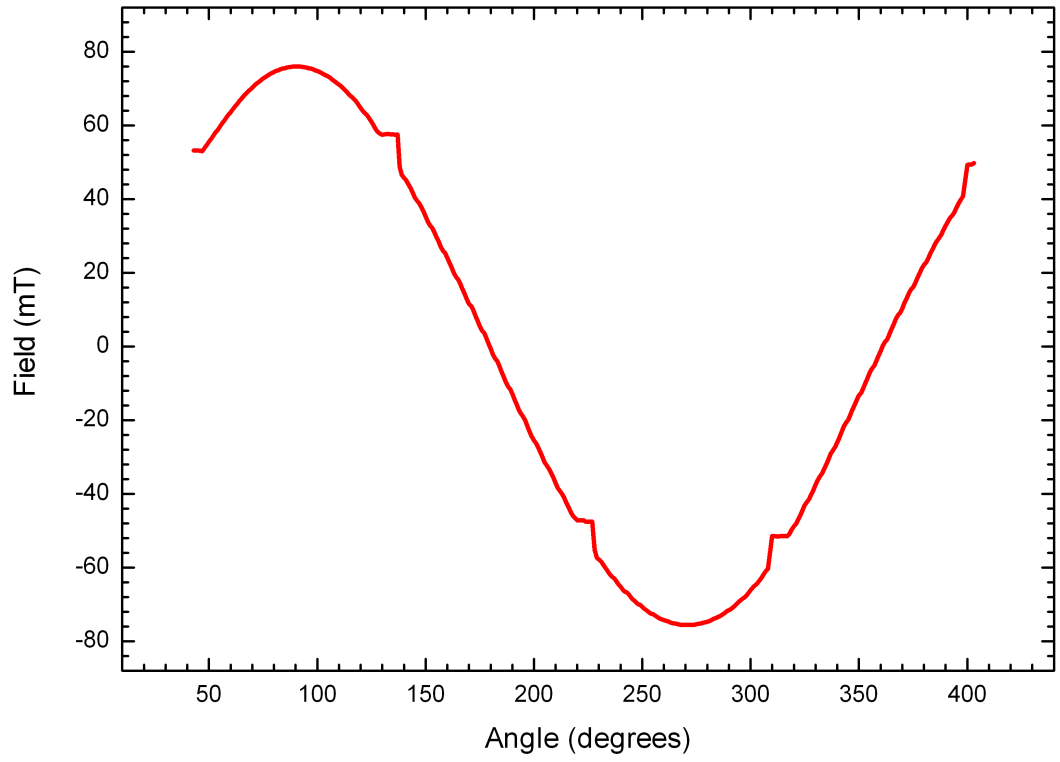

Figure 3.12: Plot of Hall probe response to a rotating magnetic field. Due to the remanence of the soft iron pole pieces, certain field angle are not achievable. This effect manifests as deviations from the cosine behavior at 45° 135°, 225° and 315°.

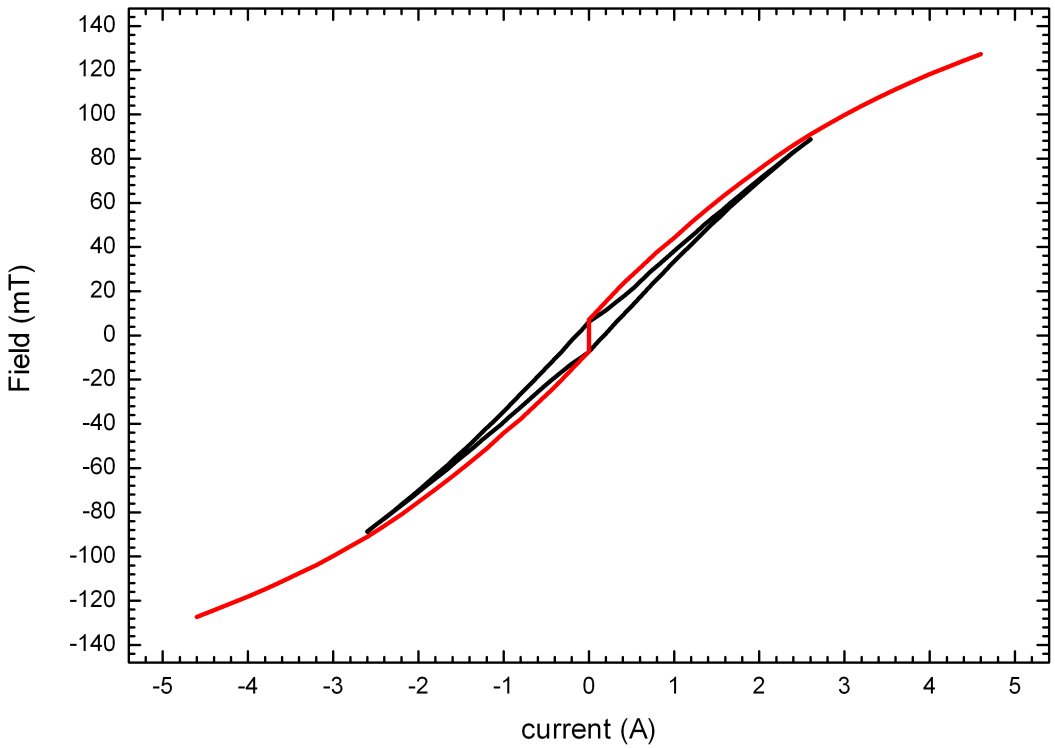

Figure 3.13: Plot of Hall probe response (black) versus the result calculated via a field calibration (red).

in Berkeley, USA. Both beamlines were similar in most regards: Light is generated by packets of electrons traveling at relativistic speeds which accelerate when undergoing a change in direction caused by an end station insertion device. An elliptical polarization undulator (EPU) insertion device (figure 3.14) provides polarization control, followed by a monochromator to select the wavelength. The end chamber of both consisted of a vacuum chamber integrated with an octupole electromagnet. The magnets consist of eight soft iron pole pieces with water cooled copper windings. Samples were mounted on copper sample holders at the end of continuous flow liquid helium cryostats. The x-ray absorption was measured via the sample drain current due to electrons ejected from the sample via the $\sim$ 99% [41] of recombination processes which result in the emission of an Auger electron. These Auger electrons scatter inelestically to produce a small but measurable secondary electron yield current which is directly proportional to the x-ray absorption. The electron yield in nanoamps was amplified and the resulting voltage converted to counts per second using a voltage to frequency converter. A similar methodology was used to record the signal from a gold mesh placed just before the end station, which was then used to normalize the signal and remove any unwanted beam intensity or monochromator dependencies. Electron yield measurements have the

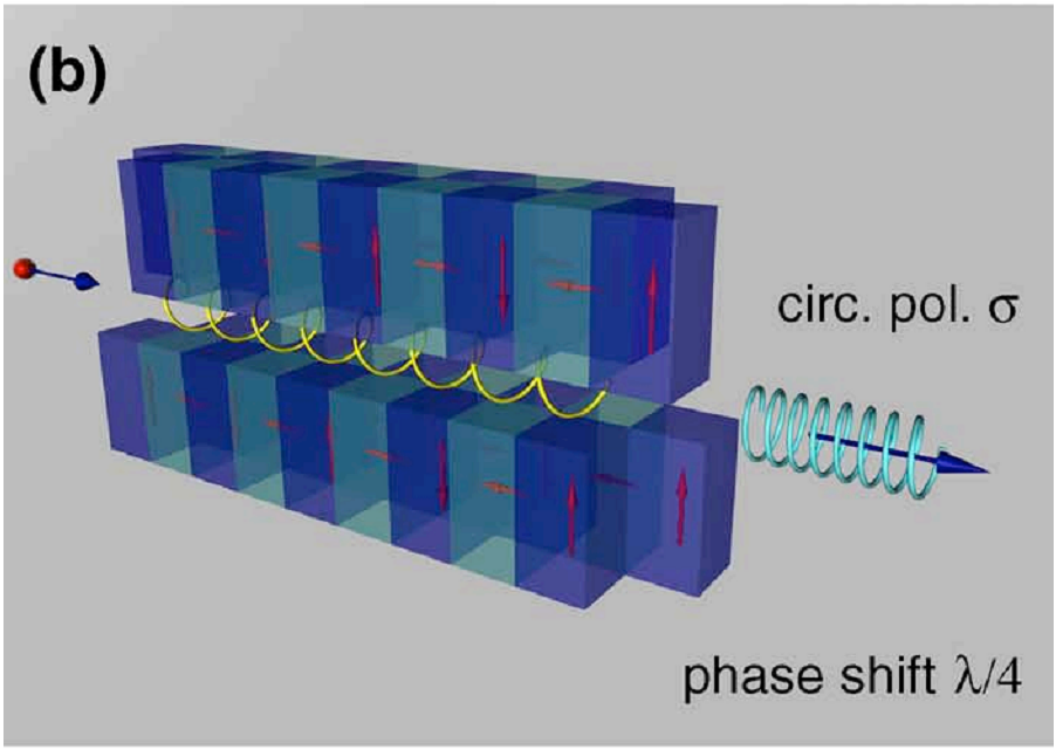

Figure 3.14: Diagram of EPU, after [42]

advantage over photon yield measurements of delivering a significant degree of surface sensitivity.

The octupole magnet in operation at the ALS is described in detail elsewhere [43]. The octupole configuration allows for the generation of sustained fields of up to 700 mT in any direction, and has a field uniformity of better the 1% for a 5 mm radius at the center of the chamber. The MAXLAB magnet was of a similar configuration, with similar theoretical performance, but at the time of measurement, problems with corrosion caused by the cooling water on some of the pole pieces necessitated the running of the system on 4 pole pieces. This resulted in a maximum usable field of 400 mT, and caused some field uniformity issues. The use of a three dimensional Hall probe to calibrate the used field geometries mitigated these issues to a large extent.

The sample geometry used during XMCD measurements is shown in figure 3.15. The x-ray beam travels in the $-z$ direction. The sample can be rotated in the θ direction in the $y-z$ plane, and the magnetic field can be rotated in both θ and ϕ directions. The sample is generally mounted with the steps running parallel to the x direction.

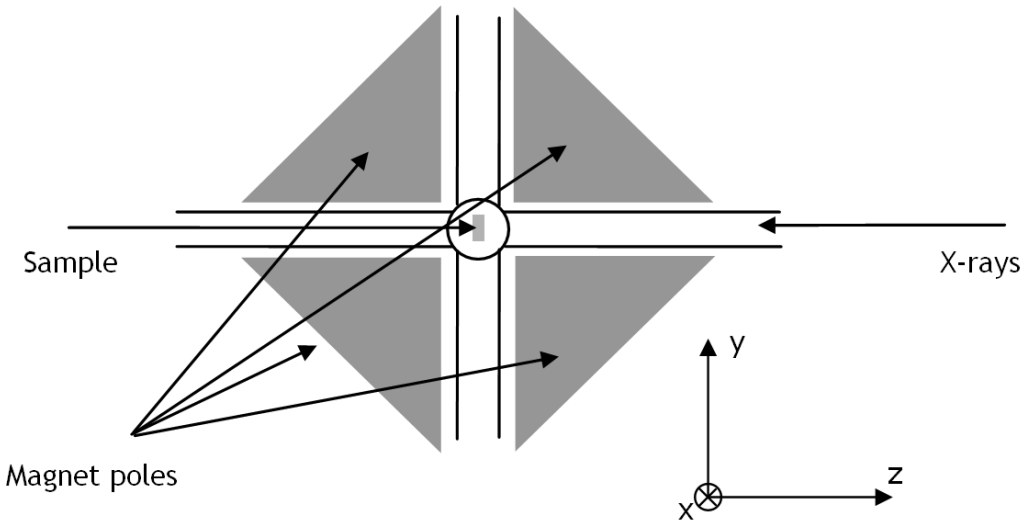

Figure 3.15: Diagram of sample configuration for XMCD measurements. θ is an angle in the $z - y$ plane, while ϕ is the angle in the $x - z$ plane.

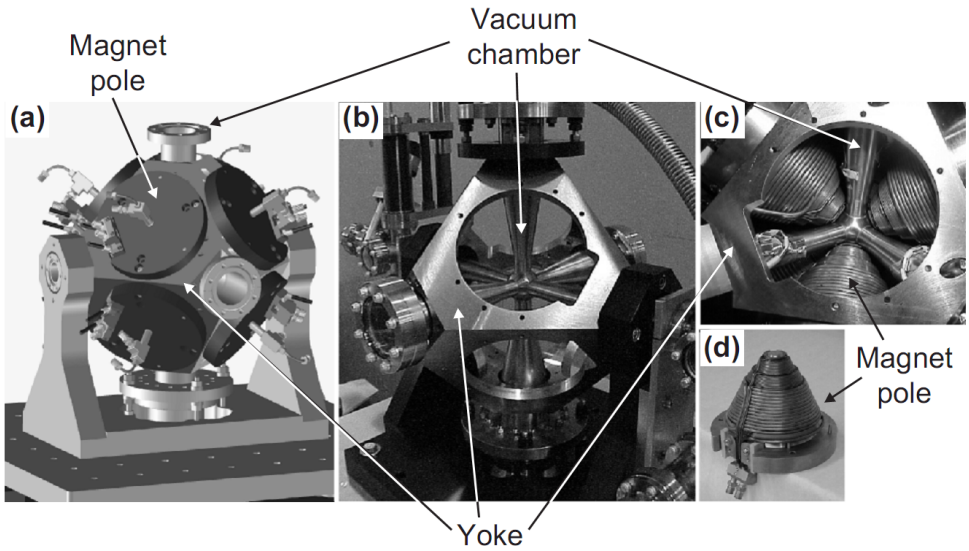

Figure 3.16: Diagram of octupole magnet and chamber used at ALS (the MAXLAB magnet is of similar design), after [43]

3.5 MOKE

MOKE is a widely used technique for measuring the response of optically thick magnetic films, and has been extended to measure optically thin films using focused single wavelength lasers and either intensity or polarization modulation techniques in conjunction with lock-in amplifiers. These surface MOKE (SMOKE) measurements [44] are well understood, and have been applied to a range of magnetic thin film systems. MOKE has gained wide usage due to its relative ease and low cost, and its ability, as with all optical techniques, to probe surfaces in a range of environments, and buried layers.

Reflection anisotropy spectroscopy (RAS) is a very sensitive normal incidence polarized reflectance linear optical technique that probes the difference in reflectance between two orthogonal directions from a sample. RAS has been mainly used to characterize semiconductor surfaces and interfaces, although its high sensitivity and ability to measure in both vacuum and liquid environments has led to its use in a range of metallic, electrochemical and organic thin film systems [34]. RAS can be used in systems consisting of isotropic substrates to measure the optical response of anisotropic surfaces and interfaces, since the RAS response of an isotropic medium is zero. Hermann *et al.* have shown how RAS can be used to probe ultra-thin magnetic films [45]. A RAS system measures the complex reflectivity difference from an anisotropic surface or interface on an isotropic substrate. This is achieved using a PEM at normal incidence. While the source of the complex reflectivity in a RAS measurement and a MOKE measurement is different, the signal manifests in exactly the same way: the reflected light has undergone a complex rotation in its polarization. As such, a RAS setup is functionally similar to a PEM based MOKE setup, such as that described by Sato [33]. The main difference is in the focus on spectral information adopted by RAS: broadband light sources, detectors and monochromators are utilized to obtain measurements over the entire optical spectra, and the measured signal is normalized against the mean reflectance in order to remove energy dependencies from the light source and other components. Since a RAS setup utilizes a normal incidence setup, it probes only the component of the magnetization normal to the sample surface (discussed in section 2.3). It is shown in section 5 that RAS-MOKE has sufficient sensitivity to probe, spectroscopically, less than a monolayer of ferromagnetic material provided the easy axis of magnetization does not lie in the surface plane. It is thus particularly sensi-

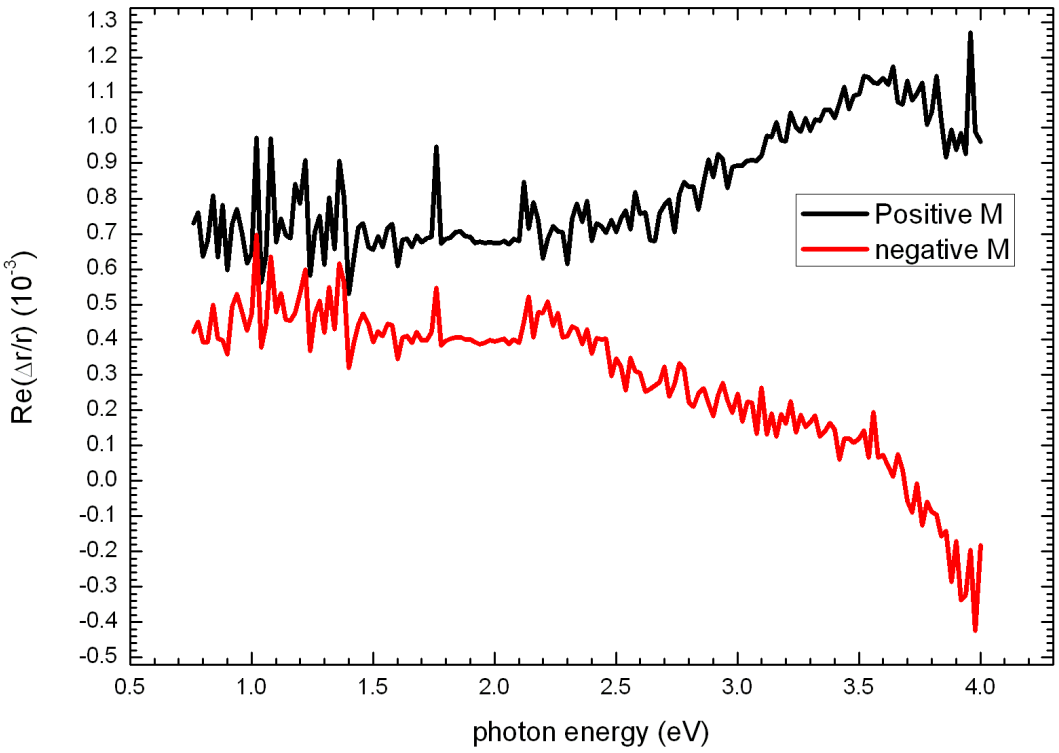

Figure 3.17: Spectral response of a 6ML Au/0.78 ML Co/Pt(997)sample for a constant field applied in 2 opposite directions. Both spectra include magnetic and structural contributions.

tive when exploring the technologically important materials that exhibit perpendicular magnetic anisotropy (PMA), and has the additional advantage of offering spectroscopic information about the magnetic response.

Since the RAS signal and MOKE signal both manifest as a change in the polarization state of the reflected light, a methodology is required to distinguish between the magnetic and structural components of a recorded spectra. This is accomplished by taking advantage of the symmetry of the magnetic response when the magnetization direction is reversed, in a similar manner to that employed in an XMCD measurement (section 3.4). Since the magnetic response inverts when the magnetization direction is reversed, the magnetic contribution to the signal can be extracted by recording 2 spectra with the sample magnetized in opposite directions (figure 3.17). The magnetic signal is then the difference between these two spectra, while the RAS signal is the sum (figure 3.18). Hysteresis measurements are done at a fixed wavelength, which is chosen based on signal-to-noise considerations.

In general, a PEM based RAS system consists of a broad-band lamp, an input polarizer, a PEM, the sample, an output polarizer, a monochromator, and some form

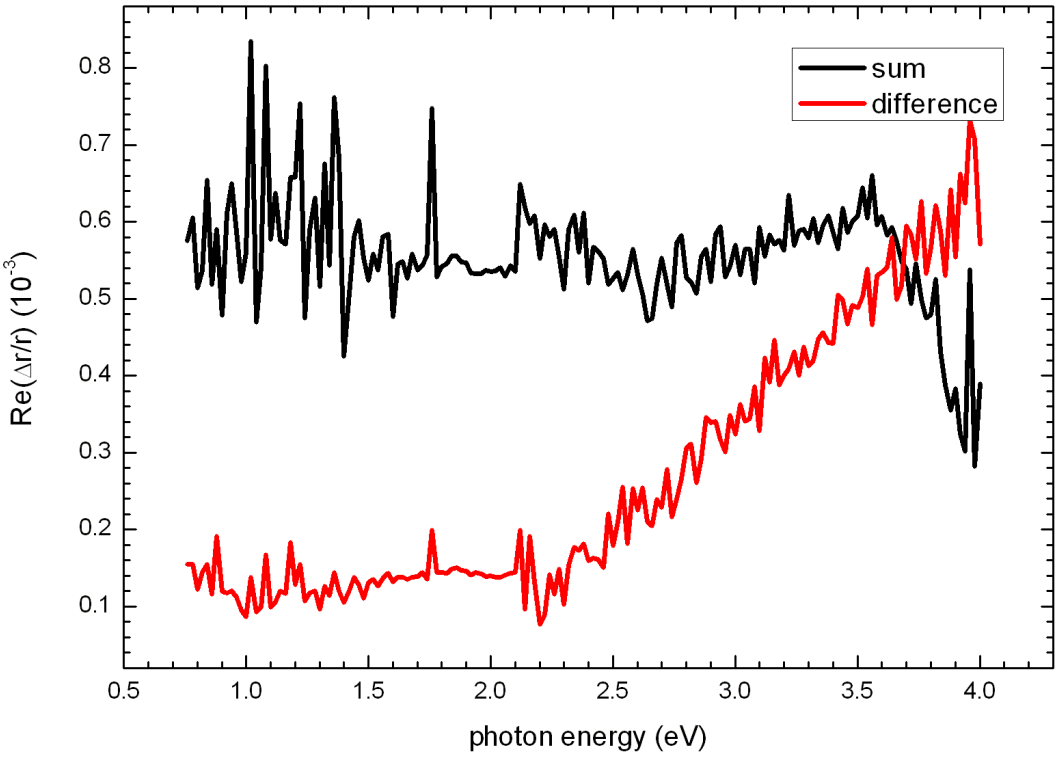

Figure 3.18: sum and difference of figure 3.17. The sum shows no structure below ∼3.5 eV, while the difference shows an increase through the visible into the UV. The error in the zero line offset in a RAS measurement may be as much as $\sim 1 \times 10^{-3} \equiv 1$ RAS unit.

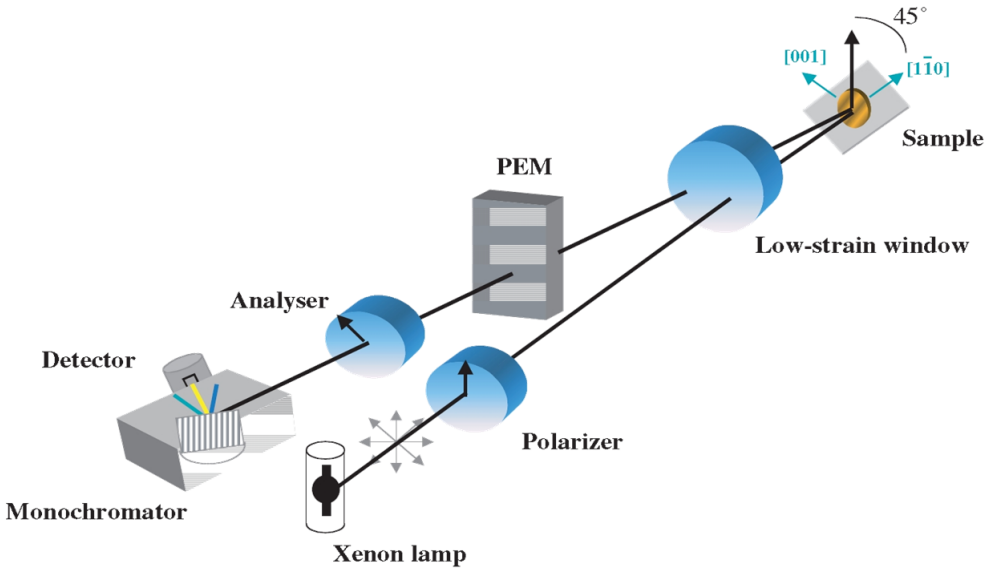

Figure 3.19: Diagram of RAS setup, after [34]

of detector (figure 3.19). The signal at the detector is then split into an AC component and a DC component, which correspond to the reflectance anisotropy signal and the mean reflectance. The AC signal is read via a lock-in amplifier. The RAS system is controlled via a Labview program which sets the PEM retardation voltage and the monochromator, measures the detector signal, applies any required corrections and records the RAS signal to an ASCII file.

There were two RAS systems used in the course of this work: a smaller system which had a spectral range of 0.76 eV to 5 eV, and a larger system with a range of 0.42 eV to 5 eV (figure 3.20). Both of these systems are functionally very similar, with the extended spectral range of the larger system requiring a number of differences: the transmitting optics were made of MgF_2 rather then quartz due to absorption in the IR, a larger three grating monochromator was needed over the two grating monochromator of the smaller system, and while the smaller system used a two detectors (Si and InGaAs), an additional detector (InAs) was required on the large system to cover the entire range. Filter wheels are included on both systems to remove second order effects in the monochromator. The only additions required for MOKE measurements were the electromagnet and some minor changes to the control program. It should be noted that both RAS systems were built with measurements on silicon in mind, and as such, the actual useful range for metallic samples and magnetic measurements depend on the reflectivity of the sample and the form of the spectral magnetic response.

As well as spectral MOKE and hysteresis loops measurements, the RAS-MOKE

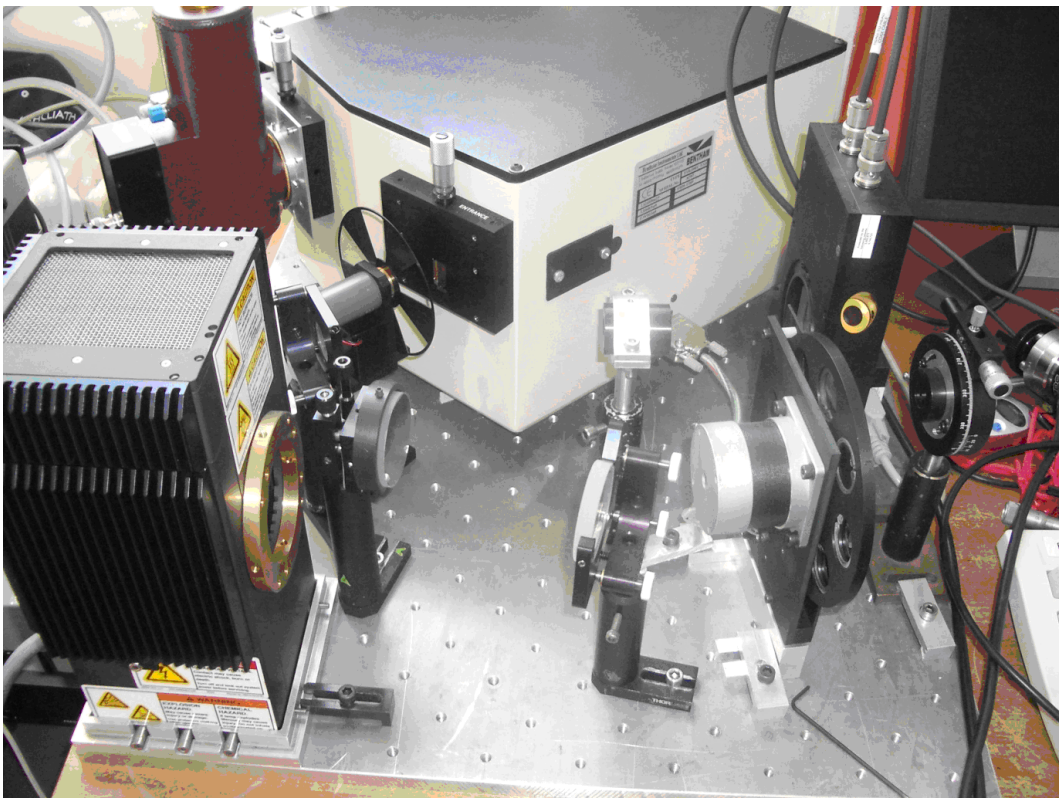

Figure 3.20: Picture of larger RAS setup.

setup in combination with the quadrupole magnet allowed for field rotation experiments. If a field of constant magnitude, which is above the coercive field of the sample, is rotated in a plane while the MOKE response is measured, the resulting plot of the MOKE response versus field angle can give information on the easy axis direction of the sample, in addition to hysteresis information.

3.6 MSHG

As discussed in section 2.4, there are two main measurement geometries; rotating sample and rotating polarization, both of which can be made at various angles of incidence. In situations where sample motion is difficult, such as in a vacuum chamber or optical cryostat, it can be advantageous to use polarization rotation. This typically involves rotating the polarization direction of the input (output) light, while keeping the sample and output (input) polarizer in a fixed position.

Regardless of geometry, SHG measurements have a number of common requirements. The main requirement is that of a laser with sufficient peak power such that a measurable second harmonic response is generated without perturbing or damaging the sample: very short laser pulses with high peak powers are required. A Coherent

(Coherent inc. Santa Clara, USA) Mira Ti-sapphire femtosecond laser pumped by a Verdi 5 W continuous wave LBO laser was used to seed a Coherent inc. RegA regenerative amplifier, which was pumped by a Verdi 10 W LBO laser. The Mira produces laser pulses of ∼150 fs length at a repetition rate of 76 MHz and an average power of 700 mW at 800 nm. The average spectral width of the pulses is ∼12 nm, and the average pulse energy is in the nanojoule range. The amplified pulses are of ∼200 fs length at a repetition rate of 200 kHz with average power of 1 W. The energy per pulse is in the microjoule range, which allows for a significant second harmonic response, while the average energy is low enough that the sample does not undergo significant heating effects.

Even with these large peak powers, only one SH photon is generated for every $\sim 10^{14}$ input photons and photon counting techniques are required to achieve good signal-to-noise. This is achieved using a photon counting photomultiplier tube (PMT) and a photon counter. Measurements are carried out in the dark, and care must be taken in ensuring that the first harmonic light is properly removed before the PMT, as it can easily swamp the signal. It is also important that only signal from the sample enters the PMT, and any SH light generated in optics is removed. As such, care must be taken in the placement of any non-reflective optics, and a filter should be used before the sample to remove any potential SH signal generated in the input optics. Another consideration is that, since SHG is highly symmetry dependent, high quality polarizers with an extinction coefficient of at least 10^{-4} should be used to ensure that there is no cross leakage between the different polarization components.

Figure 3.21 shows the setup used to measure MSHG. The RegA beam goes through a Glan-Taylor polarizer which has an extinction coefficient of 10^{-5} and is set for maximum transmission. A halfwave plate mounted in a computer controlled stepper motor allows for rotation of the polarization. The beam is then directed through a 45° dielectric mirror onto a silvered focusing mirror of 50 cm focus length, which produces a spot size at the sample position of ∼200 μm. The sample is positioned in the center of a quadrupole magnet on an aluminium sample holder with an embedded Hall probe (Honeywell SS94A2D). An OG550 Schott glass filter removes any second harmonic generated in the polarizer and halfwave plate. For a normal incidence geometry, a dichroic mirror is set at a 45° angle to the beam. The dichroic mirror transmits the first harmonic light reflected from the sample back to the focusing mirror, while reflecting the second harmonic generated at the sample through the output optics. The

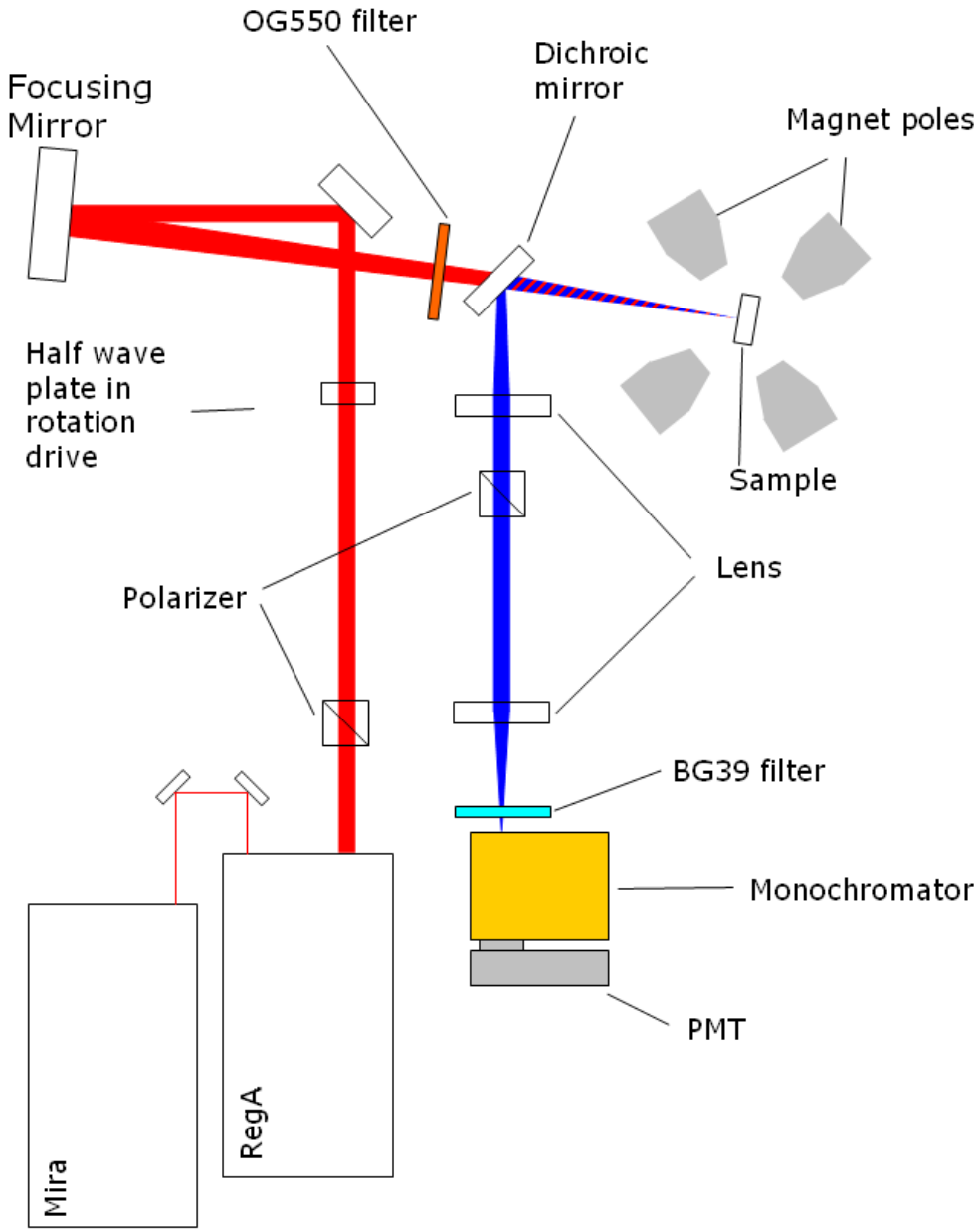

Figure 3.21: Diagram of a polarization rotation normal incidence MSHG setup.

output optics consist of a lens to re-collimate the light, a second Glan-Taylor polarizer to select the output polarization, and a lens to focus the beam onto the entrance slit of a monochromator. The output optics are aligned by introducing a BBO crystal into the beam after the dichroic mirror. This generates a visible amount of second harmonic light along the same beam path as that of the sample second harmonic signal. A side-on photon-counting PMT (Hammamatsu R1527P) mounted on the exit slit of the monochromator collects the second harmonic photons, which are discriminated and counted using a computer controlled photon counter (Stanford Research SR400). A Labview program is then used to set the halfwave plate and magnet, and read the resulting counts from the photon counter.

4 XMCD of Au-capped Co nanowires on Pt(997)

4.1 Overview

As discussed in section 2.2, the XMCD signal is measured by taking the difference between two x-ray absorption spectra taken with opposite magnetization or light polarization. However, by taking the average of these two spectra, one obtains the magnetization independent absorption spectrum. This spectrum has two main uses: the shape of the spectrum gives information on the oxidation state of the Co, and the difference between the post- and pre-edge background level is required in the sum rules to separate the spin and orbital moments. For the Au-capped Co nanowire system, the small amount of magnetic material, together with the capping layer meant that the Co signal was very small compared to the background. This meant that fluctuations in the background, which would be inconsequential for thick magnetic films or bulk samples, were of a similar size to the Co edge signals, which made background subtractions impossible. Figure 4.1 shows the variation between five separate scans recorded one after the other on a six atom wide Co wire capped with nine monolayers of Au. This varying background made determination of the constant C, which is required for the separation of the spin and orbital moments, impractical. In terms of the Co oxidation state, however, these scans were useful in confirming that the Co had not oxidized, and as such, that the capping layer had successfully protected the Co from the atmosphere. Figure 4.2 shows typical oxide and pure metal Co spectra, alongside measured spectra for comparison. This allows an upper limit of 10% to be placed on the possible oxidation of the capped Co wire samples. The spectra for the six and nine monolayer capping thicknesses were reproducible over a period of several months, which, when combined with the AES evidence of oxide-free UHV growth, is good evidence that the capped Co wires are not significantly oxidized during the course of these measurements.

Although the variable background made it impossible to determine the sum-rule constant C from the XAS scans, it had little effect on the recorded asymmetry. This was due to the method of data recording employed: at each energy position, the field was switched from positive to negative, and points for both cases were recorded. These points were then subtracted to obtain the magnetization asymmetry. Since the variations in the background happened over relatively long time periods, this method of recording the asymmetry on a point by point basis removed any background variations

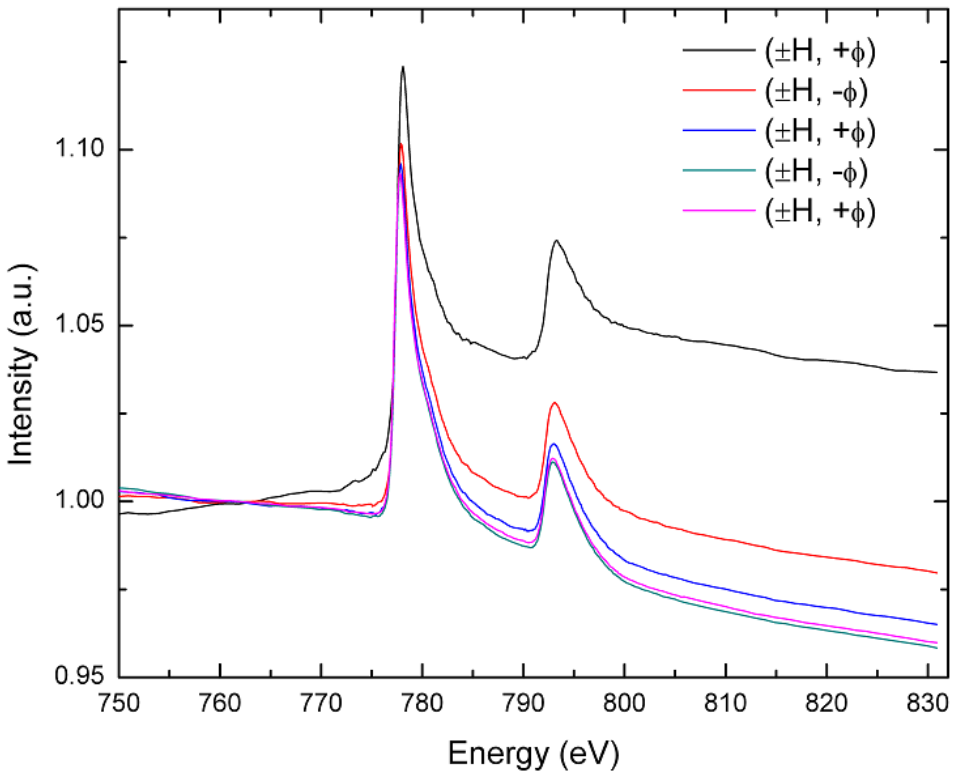

Figure 4.1: Graph of five normalized, magnetic field averaged XAS spectra recorded on a six atom wide Co wire sample capped with nine monolayers of Au. The spectra were taken one after the other with polarization switched between scans. The shape of the background changes from scan to scan, after [30].

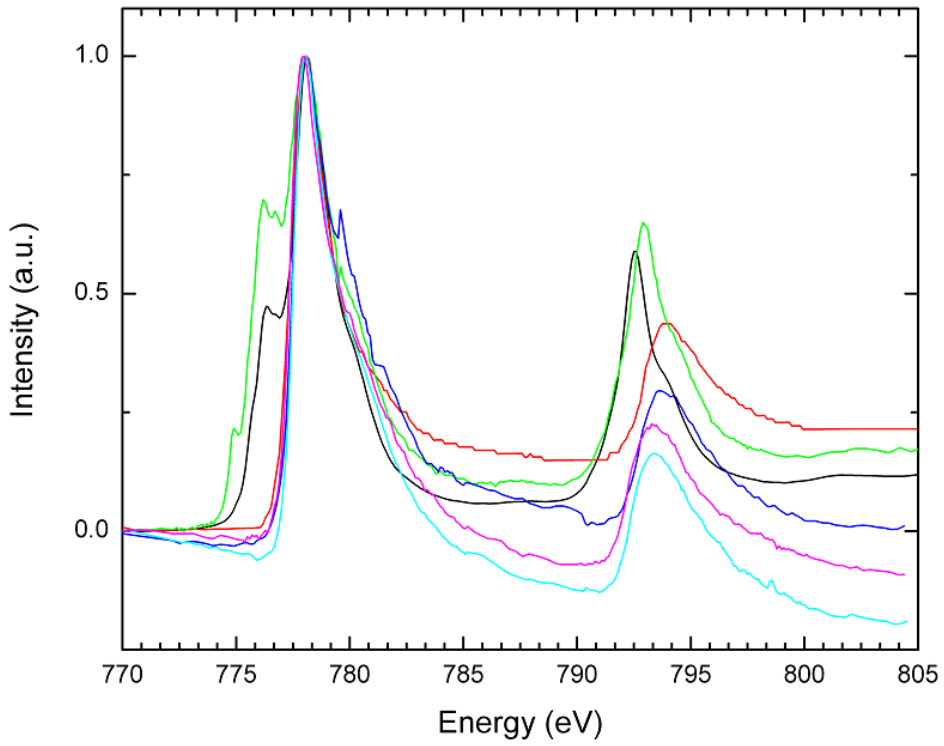

Figure 4.2: Co metal (red), CoO (green) and Co_3O_4 (black) XAS spectra compared with measured XAS spectra for a three atom wide Co wires capped with three (blue), six (cyan) and nine (magenta) monolayers of Au. All spectra are normalized to the L_3 edge, after [30].

from the asymmetry measurements. As such, the bulk of the analysis was based on the asymmetry measurements rather than the XAS spectra. Hysteresis measurements were also possible due to the reduced amount of time required to measure a hysteresis loop compared to an XAS scan. While the saturation asymmetry was inconsistent at times, the coercivity proved to be reproducible, which allowed field angle versus coercivity plots to provide easy axis information, and an interesting temperature dependence in the coercivity to be observed.

4.2 Sample 1: 3/6 atom wide Co wires capped with 3/6/9 monolayers of Au

The first sample measured consisted of six different patches; two different Co coverages, each with three different Au cap thicknesses (figure 3.6). The Co coverages used correspond to three atom wide and six atom wide wires. All data presented were processed in the same way:

1. XMCD spectra were determined from the magnetization asymmetry, and in all cases at least one positive polarization (right-circularly polarized) and one negative polarization (left-circularly polarized) spectra was recorded, to confirm consistency.

2. Spectra were smoothed using a five point adjacent averaging method.

3. A linear fit was done to pre- and post-edge regions, where no dichroism should be observed, and this linear fit was subtracted for the scans.

4. The sum rules were applied to each spectra individually, and all values for the orbit-spin moment ratio quoted are averaged across all spectra, with the quoted error being the standard deviation.

Figure 4.3 shows recorded XMCD spectra for three and six atom wide wires for the three different capping thicknesses, with all scans scaled to the L_3 edge. The six wire scans were taken at room temperature, while the three atom wire scans were taken at 79 K. While there is a visible difference in the L_2 edge intensity between the three atom wires and the six atom wires in figure 4.4, the capping layer thickness appears to have little effect on the XMCD response. Using the sum rules described in section 2.2, the orbit-spin moment moment ratios were calculated (figure 4.5). It is observed that

Table 1: Comparison of uncapped and capped orbital moments.

System	m_L Gambardella	System	m_L Our results
Co(0.39 ML)/Pt(997)	0.37 ± 0.04	Au(3/6/9 ML)/Co(0.39 ML)/Pt(997)	0.38 ± 0.02
Co(1 ML)/Pt(997)	0.31 ± 0.04	Au(3/6/9 ML)/Co(0.78 ML)/Pt(997)	0.28 ± 0.05

the ratio remains constant with increasing cap thickness, but increases with decreasing wire width, an effect also seen for uncapped wires [46].

As discussed previously, the experimental separation of the orbital and spin moments is not possible with these measurements. However, theoretical calculations show only small variations in the spin moment below monolayer coverages [47, 48]. As such, it can be instructive to assume a spin moment of 2.03 μ_B, such that orbital moment values can be compared to other published data. Table 1 shows good agreement between measured values and the uncapped values published by Gambardella *et al.* [4]. This indicates that capping layers do not have a significant effect on the spin or orbital moment. This suggests that the wire morphology was unchanged by the capping process, as the orbit-spin moment ratio is known to be affected by the local magnetic environment in a system [49]. However, this would also suggest that the addition of a capping layer should cause a significant change in the values between the capped and uncapped samples, which is not observed. This is unusual, as the significantly modified Curie temperature, easy axis and coercivities of the capped samples reported later would suggest a large change in the spin and orbital moments. It is possible that the assumption that the spin moment is roughly 2.03 μ_B is incorrect, and large changes in the spin and orbital moment are present, but the ratio stays similar. However, this is speculative, and further measurements are required to confirm the behavior of the spin and orbital moments in the system.

In terms of the hysteretic behavior of the samples, there were two main effects measured: temperature dependencies in the measured coercivities, and easy axis directions. In terms of the easy axis measurements, there are a number of ways of measuring the easy axis direction. If the sample (or the easy axis, and therefore $\hat{M}$), is rotated in the θ direction while the applied magnetic field is kept parallel to the x-ray beam (along the z axis, see figure 3.15), then one would expect the magnitude of the asymmetry to decrease with a cosine behavior as the easy axis moves away from the z axis, due to the $\hat{k} \cdot \hat{M}$ nature of the interaction (equation 2.3). However, due to the time taken to make

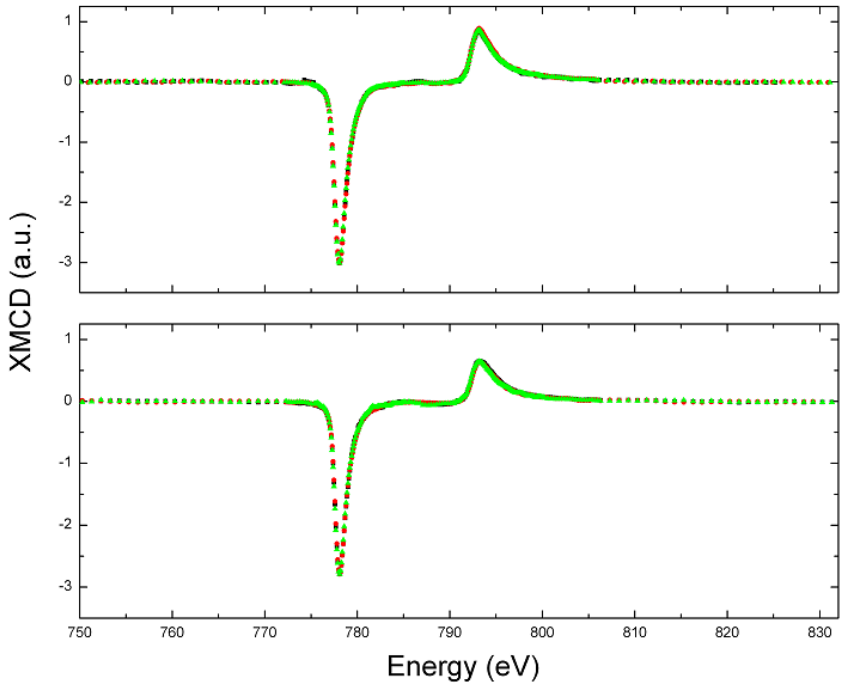

Figure 4.3: XMCD spectra of six (top) and three atom (bottom) wide Co wires capped with three (black) six (red) and nine (green) monolayers of gold.

measurements, and the previously mentioned background variations in the signal, this method was problematic for our samples. This led to the second method: if either the sample or the magnetic field is rotated in the θ direction, and hysteresis loops are taken for each angle, the coercivity should change in a predictable manner depending on the magnetization rotation mechanism of the sample. If the sample follows the Stoner-Wolfarth coherent rotation mechanism, then the coercivity should decrease as the applied field moves away from the easy axis. However, if the rotation mechanism is a domain wall motion, the applied field induces a torque in the domain wall, causing the wall to move in a direction perpendicular to the applied field. This leads to the coercivity increasing as the angle between the easy axis and the magnetic field increases ($H_c \propto 1/\cos\alpha$, where H_c is the coercivity and α is the angle between the applied field and the easy axis) [3, 28]. This is based on domain walls experiencing a torque because the magnetization direction in the wall is not aligned with the applied field direction:

$$T = \mu_0 \hat{M} \times \hat{H} \tag{4.1}$$

Since the coercivity of a measured loop is less affected by drifts in the background, this gives a method for determining the easy axis of our samples. There is one other method, which is the field rotation method also used in RAS-MOKE experiments

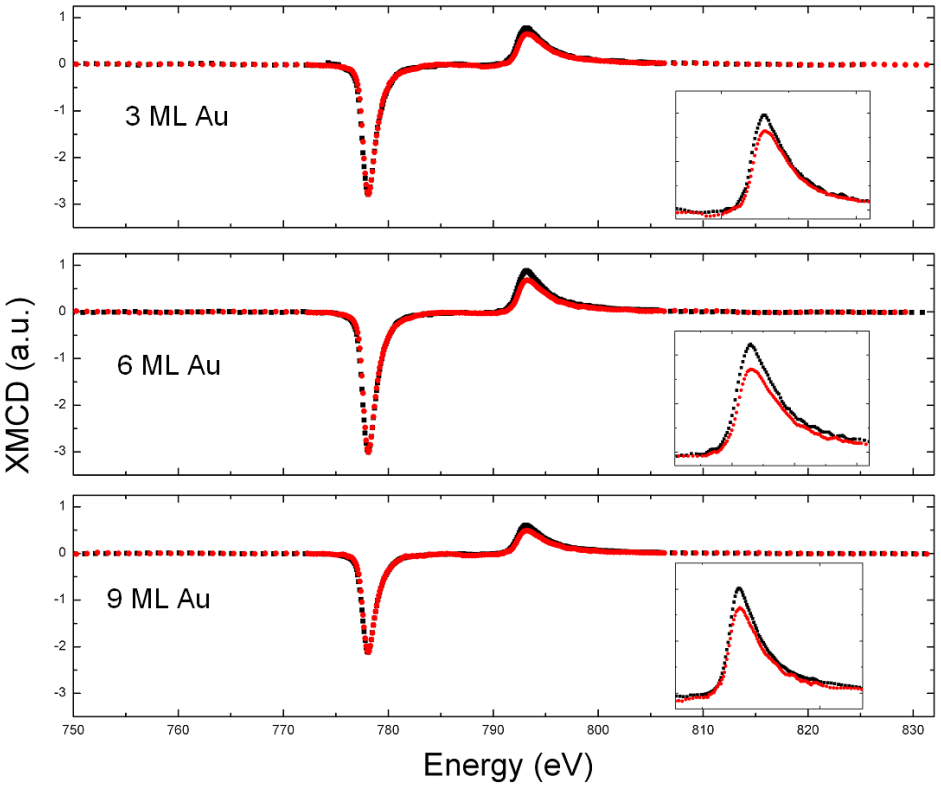

Figure 4.4: XMCD spectra of six (black) and three atom (red) wide Co wires capped with three (top) six (middle) and nine (bottom) monolayers of gold. All spectra are scaled to the L_3 edge. The three atom wires show a consistently smaller dichroism at the L_2 edge (insets).

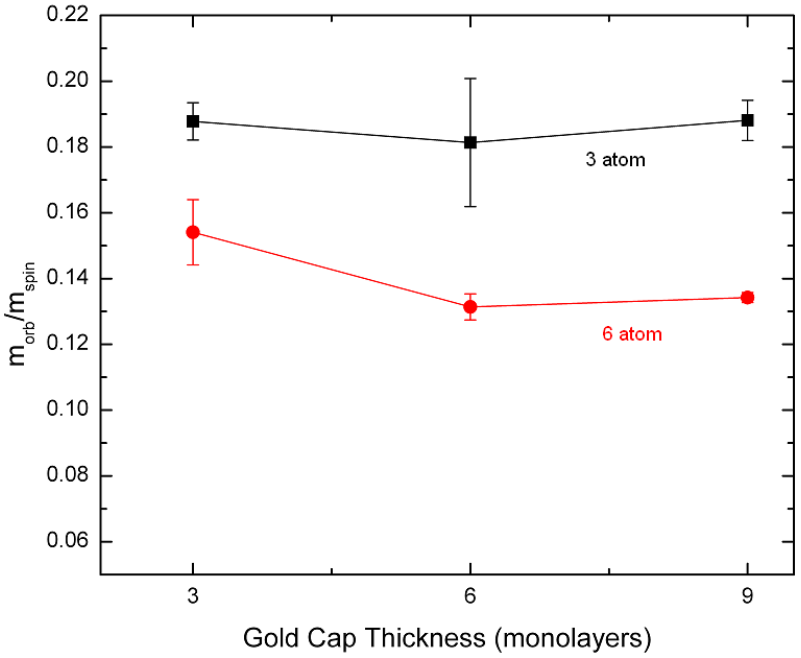

Figure 4.5: Calculated orbital to spin moment ratios for the three atom wire (black) and six atom wire (red) versus capping thickness.

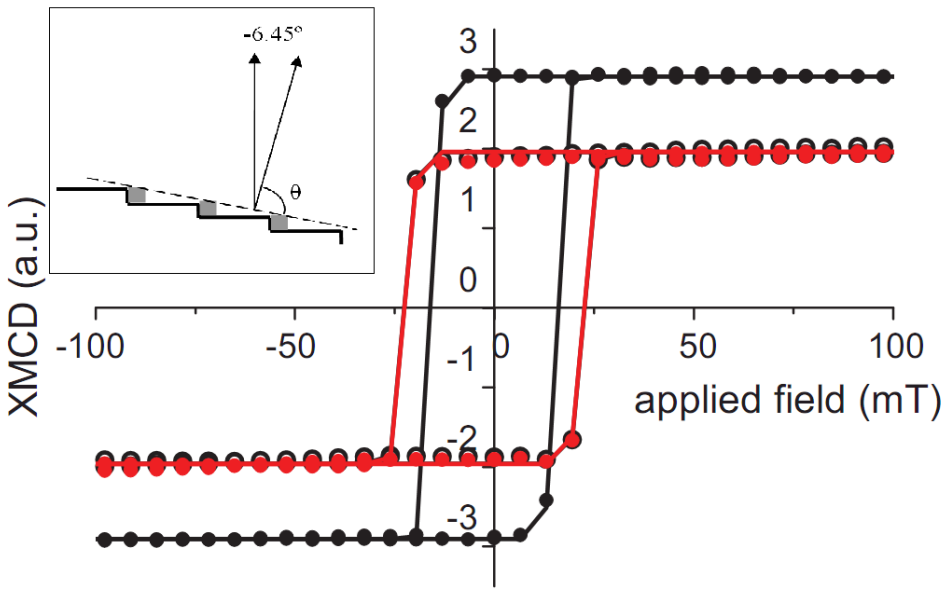

Figure 4.6: Graph of three hysteresis loops measured on a six wire sample capped with six monolayers of Au. Loops were recorded at the L_3 edge. Loops were taken with the sample rotated around θ by -6° (filled black circles) -51° (filled red circles) and +39° (open black circles). Inset shows side on view of sample, with surface and terrace normals.

(section 3.5). While this method can give quite good XMCD results at times, it is limited by the fact that it requires that the field direction is swept through the plane of the sample. This causes large Lorentz force suppression of the total electron yield signal, which effectively amplifies any discontinuities or spikes in the signal, which can make it difficult to obtain clean results.

Figure 4.6 shows three separate hysteresis loops taken by rotating the sample in the θ direction while maintaining the field in the z direction. The wires were aligned parallel to the x direction. It can be seen that as the sample is rotated, the saturation asymmetry decreases, while the coercivity increases. It is also observed that there is a symmetric behaviour around the -6° point. This is consistent with the magnetization changing by domain wall motion, with an easy axis of ∼-6° from perpendicular. Figure 4.7 shows coercivity versus applied field angle for measurements which were made by measuring hysteresis loops with the applied field at fixed angles from the z direction while keeping the sample at normal incidence to the beam. The resulting hysteresis loops were then fitted using a generalization of equation 2.28 to extract coercivity

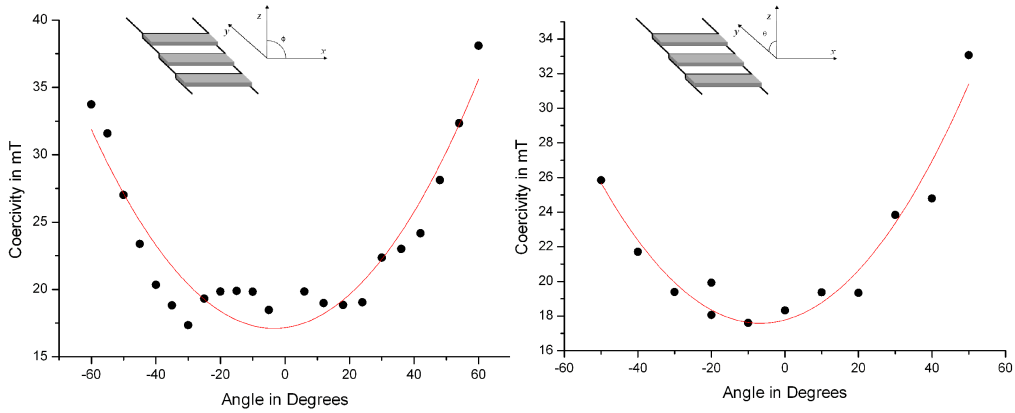

Figure 4.7: Graph of measured coercivity versus magnetic field angle (black points) with cosine fit (red line) for a six wire sample capped with six monolayers of Au. Field was rotated in a plane parallel (left) and perpendicular (right) to the wires, with the x-ray beam at normal incidence to the sample. Data were extracted from hysteresis loops taken at the L_3 edge. The fits produced an easy axis direction of -3° ± 2° (left) and -7° ± 2° (right).

values:

$$X^{\pm}(H) = -X_{sat} + \frac{2X_{sat}}{1 + exp[-s(H \mp H_c)]} \tag{4.2}$$

where the H is the applied field, s is the softness, H_c is the coercivity, and X_{sat} is the saturation value of the particular parameter being measured (proportional to the magnetization, M).

For these measurements, the saturation asymmetry was the same as the angle between the x-ray wave vector, $\hat{k}$ and the magnetization, $\hat{M}$ stayed constant. However, since the component of the applied field which lay in the direction of the easy axis changed with the applied field angle, an increase in the coercivity was observed as the angle between the easy axis and applied field changed. The field was rotated through two planes, one parallel to the wires, and one perpendicular to them. Both data sets were then fitted with a cosine function. The resulting fits complement the sample rotation data, showing the easy axis canted slightly away from the surface normal in the plane perpendicular to the wires.

Since the angle of ∼-6° found in both measurements matches closely with the angle between the terrace normal of the Pt(997) and the surface normal (6.45°, figure 1.5), it suggests that the easy axis is normal to the sample terrace planes. This is in contrast with the findings of Gambardella *et al.* [46], who found that even for a 1.3 monolayer

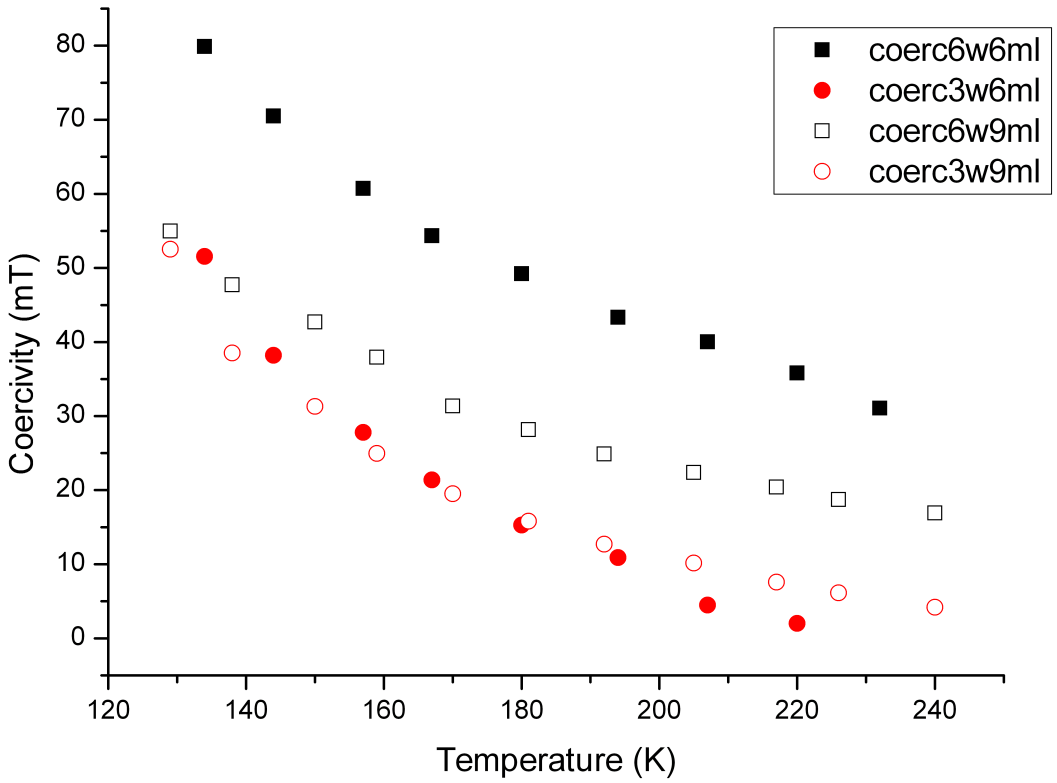

Figure 4.8: Graph of measured coercivity versus temperature for four samples: three wire, six monolayer (closed circle); three wire, nine monolayer (open circle); six wire, six monolayer (closed square); and six wire, nine monolayer (open square).

coverage of Co, the easy axis was tilted by seven degrees from the terrace normal (perpendicular to the surface). This suggests that the capping layer is modifying the MAE to favor an easy axis along the terrace normal direction. Similar behavior was observed in sample rotation measurements across capping thicknesses, and also for the three wire six monolayer patch.

Figure 4.8 shows plots of coercivity versus temperature for four different samples. The first important observation is the relatively high temperature at which a ferromagnetic state is observed. While an uncapped 1.3 monolayer sample has a reported Curie temperature below 262 K [46], the capped six wire sample, which corresponds to a coverage of 0.78 monolayers, is ferromagnetic at room temperature. Similarly, the capped three wire samples show ferromagnetic behavior below 200 K, compared to the uncapped case, where ferromagnetism was only observed below 10 K. Another important observation is that of an apparently super-paramagnetic phase in the three wire sample at room temperature (figure 4.9). Similar behaviour has been seen in a range of discontinuous small scale magnetic structures, such as granular Co/Au multilayers [50], magnetic oxide particles dispersed in polymer matrix [51, 52], dilute magnetic

semiconductors [53–55] and uncapped magnetic nanowire systems [46, 56, 57]. A super-paramagnetic system occurs when groups of ferromagnetic atoms couple via a short range exchange coupling, forming a "giant spin" or spin block. Since the coupling between spin blocks is weak, the system will have no long range magnetic ordering when there is no external field, but can be easily aligned under an external magnetic field. This manifests as magnetization curves which have relatively large saturation values, but have zero coercivity and remanence. Since the spin blocks are undergoing random thermally activated spin flips, this process can be characterized by a relaxation time. When the measurement time of the magnetization curve is comparable to or shorter than this relaxation time, the curve will show a finite coercivity and remanence. The temperature at which this occurs is referred to as the blocking temperature, T_b. Thus, the sample will show ferromagnetic behaviour below T_b, and super-paramagnetic behaviour above T_b, with the Curie temperature, which corresponds to the loss of the short-range magnetic order, occurring at a higher temperature still. Similar results are found in section 4.3. A large temperature dependence of the coercivity is also observed. In terms of trying to model this temperature dependence, there are a number of different approaches, which will be discussed in section 4.3. Figure 4.8 shows clearly, however, that the capping layer thickness has a large effect on the coercivity of the 6-wire system.

4.3 Sample 2: 1/2/3/4 atom wide Co wires capped with 6 monolayers of Au

The second sample consisted of four different patches on a Pt(997) substrate: 1,2,3,4 atom wide Co wires, all capped with a six monolayer Au cap (figure 3.6). Figure 4.10 shows the XMCD asymmetry spectra for the four and three atom wide wires. Application of the sum rules via the method described in section 4.2 yielded values of 0.39 ± 0.04 and 0.38 ± 0.01 for the orbit-spin moment ratio for the four and three wire samples respectively. The value for the three wire value agrees with that found in section 4.2 within error, confirming reproducibility between samples. The small difference between the two values for the four and three wire patches also agree with results published by Gambardella *et al.* [46] which found only small changes in the orbital moment in this coverage regime for uncapped wires. Unfortunately, signal-to-noise ratios became a significant problem with the two and one wire samples, even in

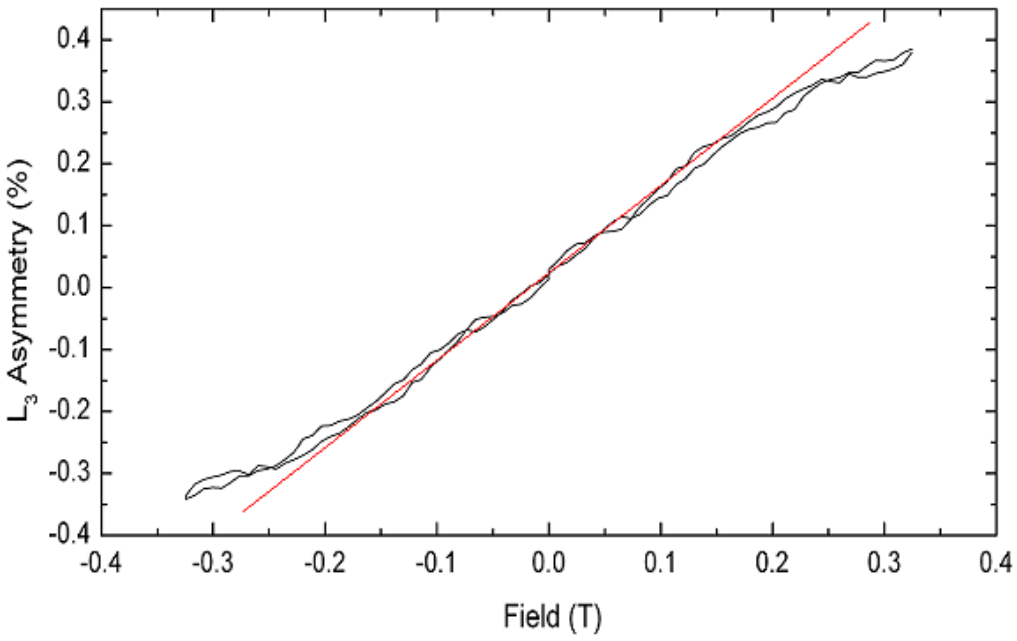

Figure 4.9: Magnetization curve measured at room temperature for the three wire sample capped with six monolayers Au. The curve shows zero coercivity and remanence, but still shows significant curvature under an applied field, consistent with a super-paramagnetic phase.

asymmetry measurements. Figures 4.11 and 4.12 show best obtained XMCD scans for one wire and two wire samples capped with six monolayers of Au at normal incidence. The total asymmetry at the L_3 edge is significantly smaller than those found in the three or four wire case. This could be due to a number of effects, including a change in easy axis direction or a reduced overall magnetization. It is also possible that the wires were in a super-paramagnetic phase, even at the lowest temperature, and the field applied (500 mT) was insufficient to saturate the sample. The noise levels were such that hysteresis measurements were not possible, and as such, very little information about these samples could be obtained. A number of quick scans were done at a range of temperatures, however, which do show a reduction of the L_3 peak on the two wire sample as the temperature approaches 100 K (figure 4.13), which is not seen in the one wire sample (figure 4.14). While this information is far from conclusive, it does suggest that the two wire sample has a lower transition temperature, whether it is a blocking temperature or Curie temperature, than the one wire sample.

Figures 4.15 and 4.16 show easy axis determination plots using the field rotation method recorded at 130 K for the three wire patch, and room temperature for the four wire patch respectively. The fits agree with the findings for the three and six

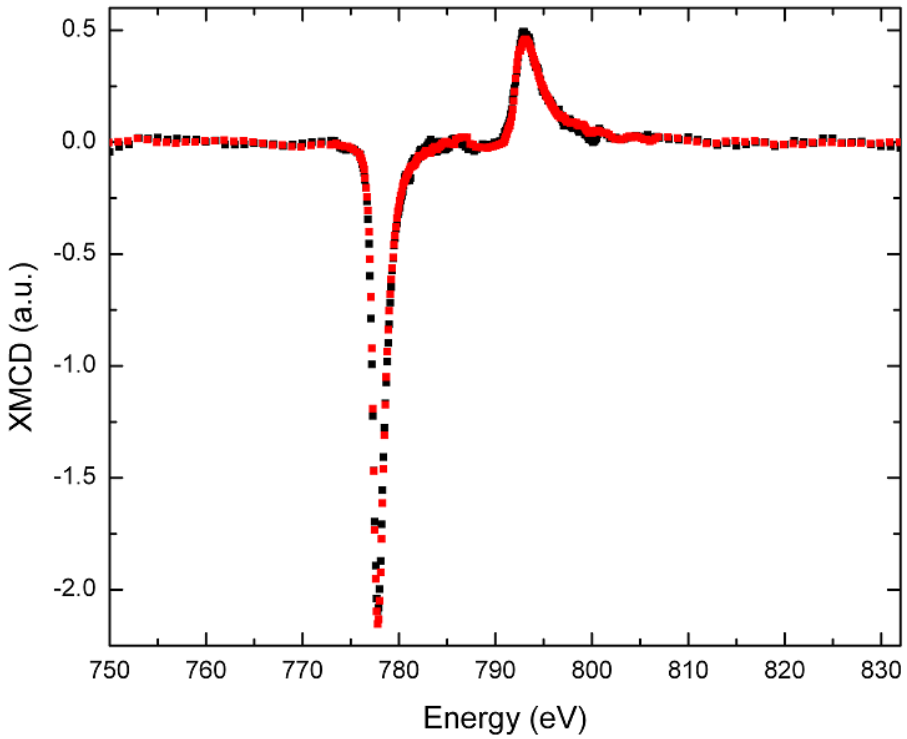

Figure 4.10: Graph of XMCD asymmetry for four (black) and three (red) atom wide wires capped with six monolayers of Au. Both scans were scaled to the L_3 edge.

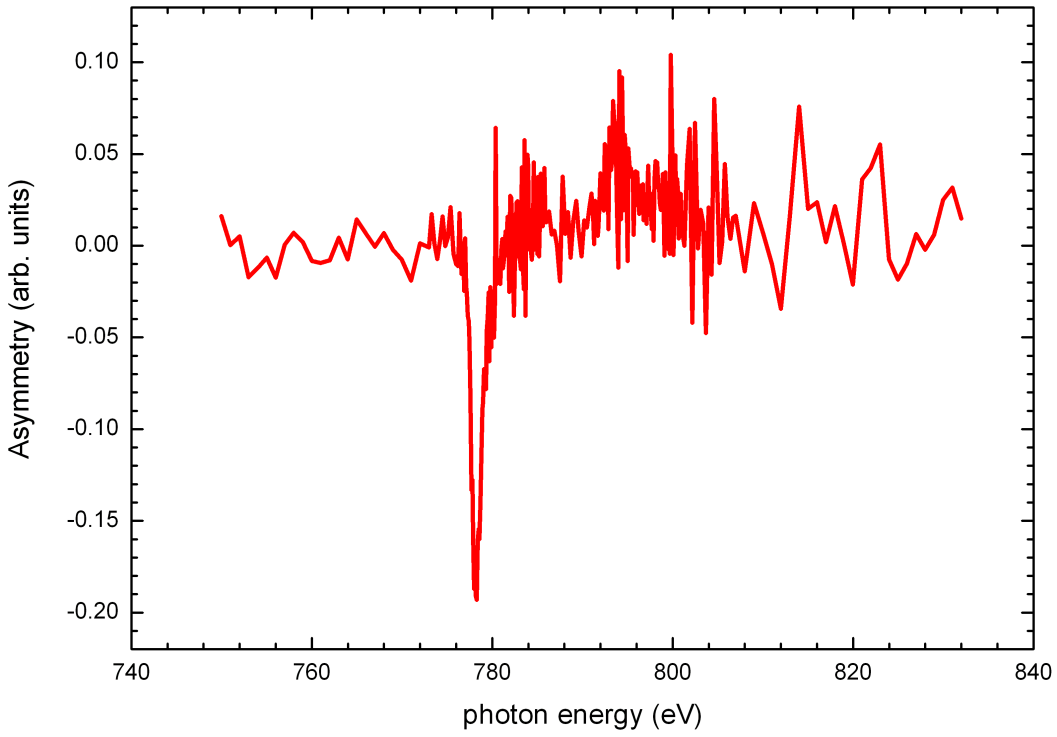

Figure 4.11: Best measured XMCD scan for the one wire sample capped with six monolayers of Au, measured at 60 K with an applied field of 500 mT. The scan was at normal incidence, with a positive beam polarization.

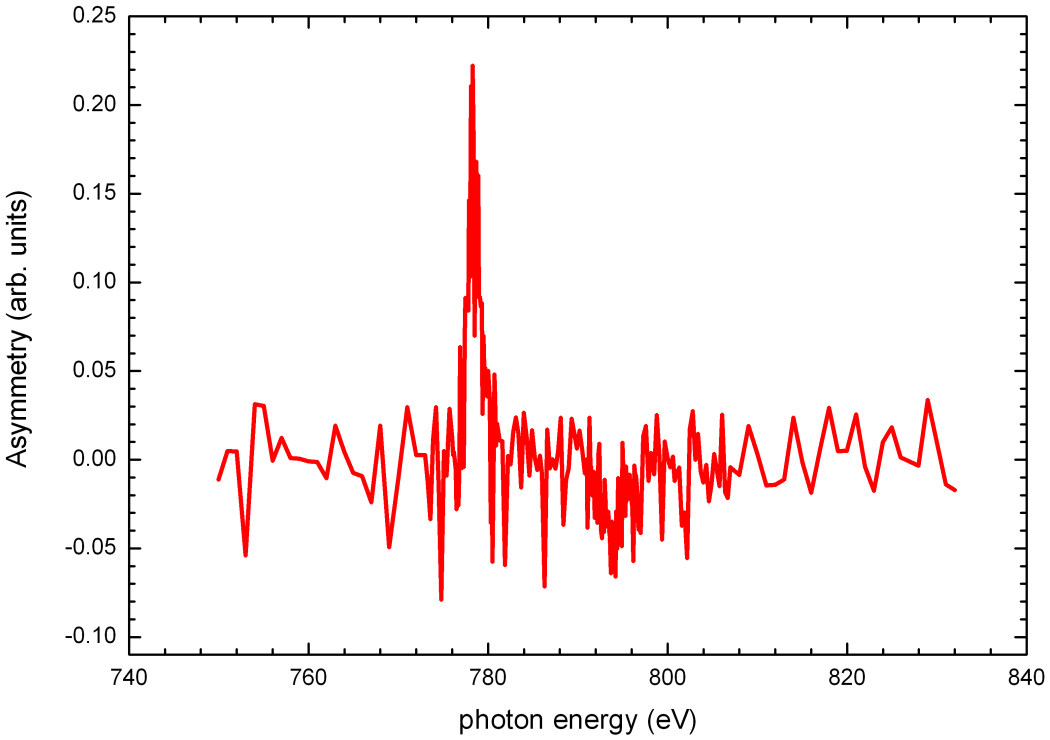

Figure 4.12: Best measured XMCD scan for the two wire sample capped with six monolayers of Au, measured at 70 K with an applied field of 500 mT. The scan was at normal incidence, with a negative beam polarization.

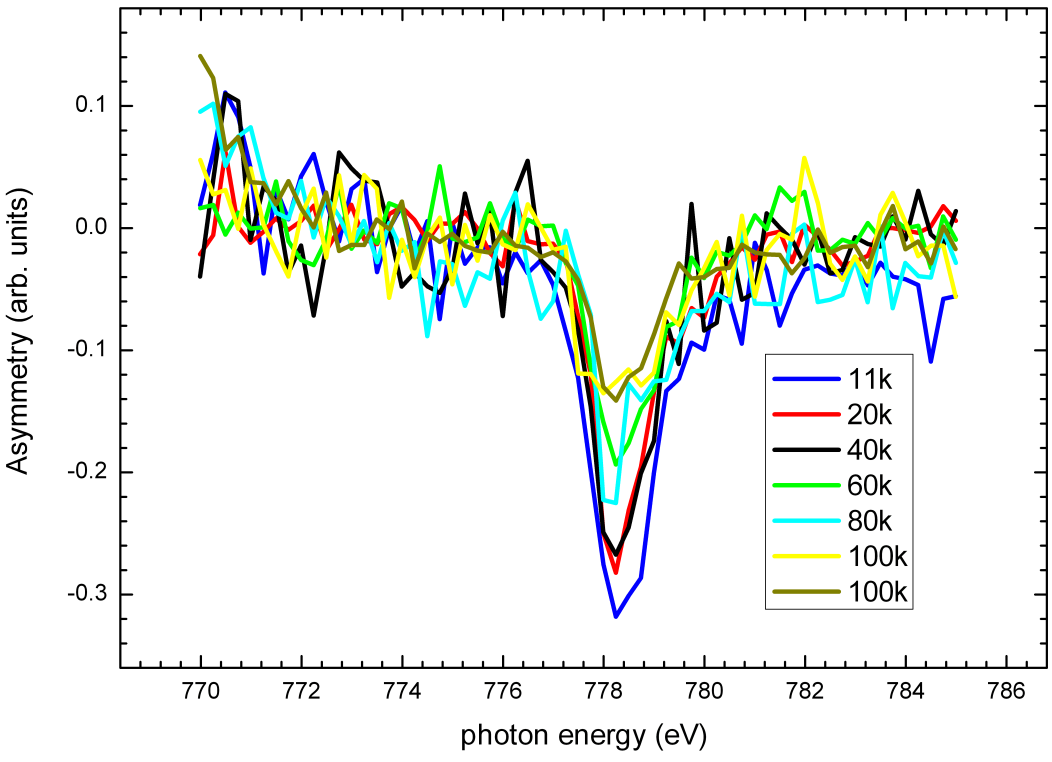

Figure 4.13: Graph of XMCD scans taken at a range of temperatures for the two wire sample. The scans were taken at normal incidence with a magnetic field of 500 mT.

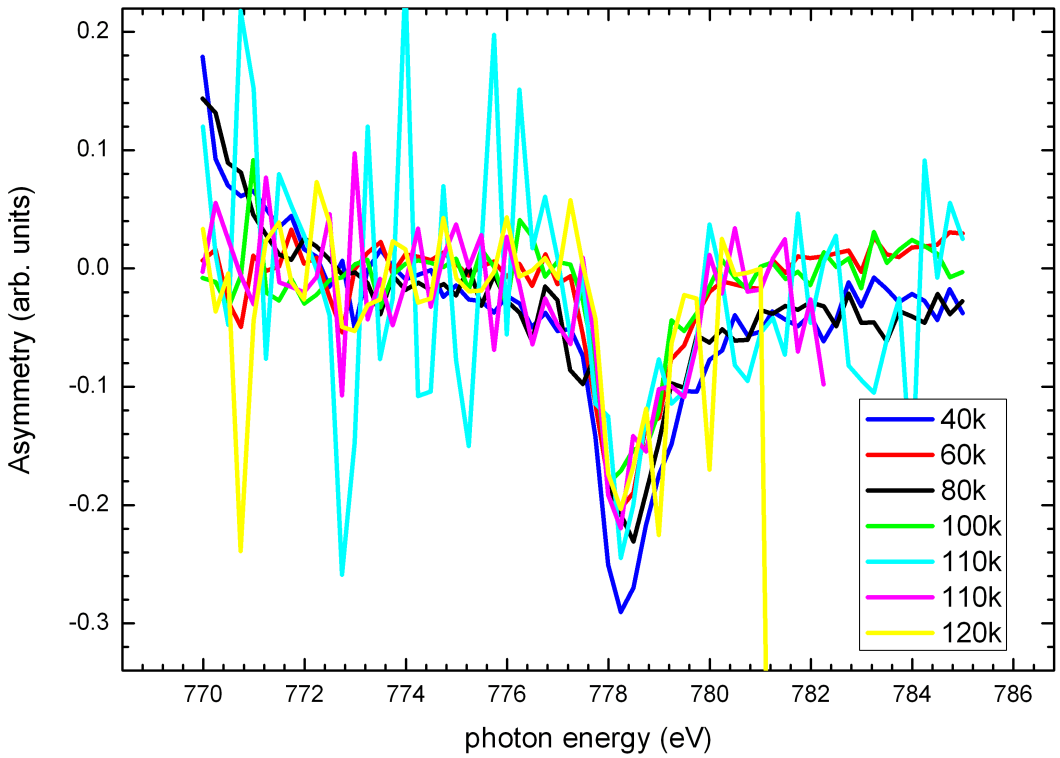

Figure 4.14: Graph of XMCD scans taken at a range of temperatures for the one wire sample. The scans were taken at normal incidence with a magnetic field of 500 mT.

wire samples, with the easy axis aligned to the (111) terrace normal within error. Additionally, a field rotation experiment was carried out on the four wire patch at room temperature (figure 4.17), which obtained results consistent with the coercivity versus angle fits (details of the fit will be discussed in section 5) Figure 4.16 shows a departure from the cosine fit that appears to be outside the experimental scatter. It is likely that this is due to calibration issues of the multipole magnets at very small fields. An example of the possible errors involved is shown for the calibration of the quadrupole magnet (figure 3.13).

Comparing these results to the uncapped wires measured by Gambardella *et al.* show large differences. Specifically, the four atom wide wire, when uncapped, has an easy axis tilted +61° from the terrace normal. While the three wire easy axis was not published, the two wire sample also had an easy axis tilted by +60° from surface normal. Since the large easy axis angles are attributed to a changes in the MAE, this suggests that the capping layer is having a large effect on the MAE of the system.

The coercivity versus temperature scans show similar behaviour to that observed in the three wire/six wire sample, and again, the three wire sample shows an apparently super-paramagnetic phase, suggesting the presence of a spin block system. As

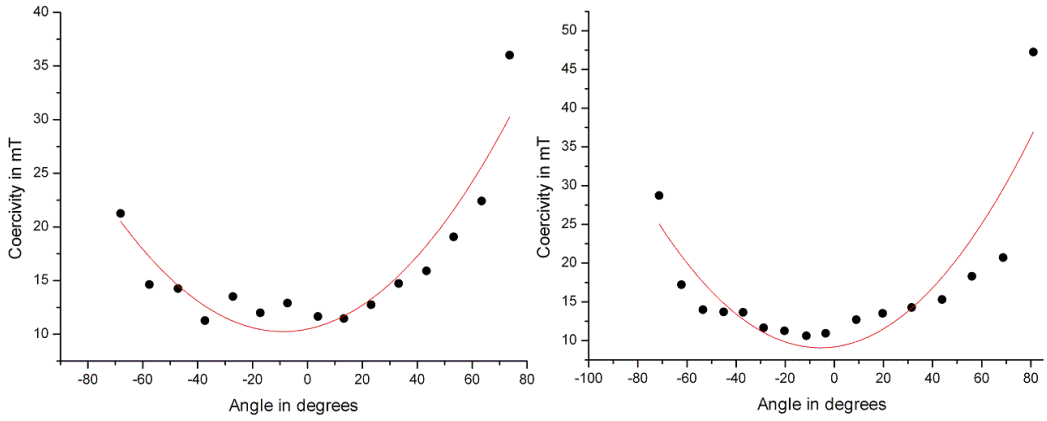

Figure 4.15: Graph of coercivity versus applied field angle for the three wire sample, capped with six monolayers of Au. The field is swept parallel (right) or perpendicular (left) to the wires. The red line shows the cosine fit, which produces values of -6° ± 4° and -9° ± 4° for parallel and perpendicular respectively.

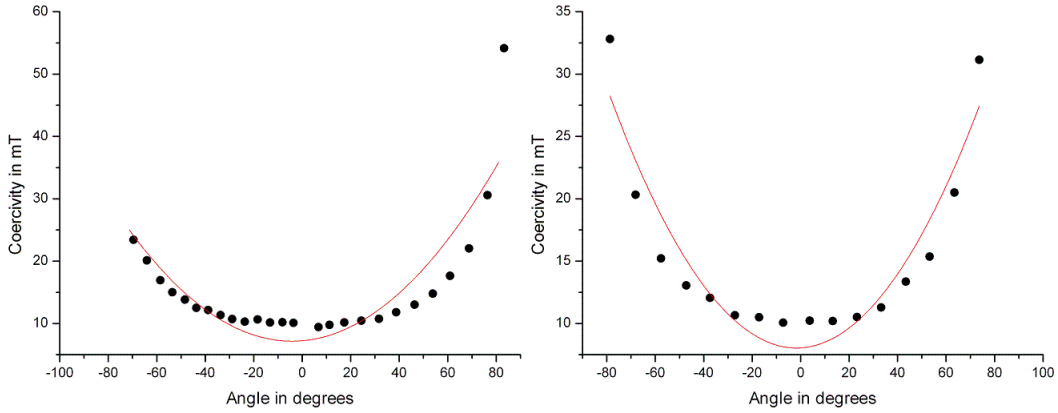

Figure 4.16: Graph of coercivity versus applied field angle for the four wire sample capped with six monolayers of Au. The field is swept parallel (right) or perpendicular (left) to the wires. The red line shows the cosine fit, which produces values of -2° ± 2° and -4° ± 3° for parallel and perpendicular respectively.

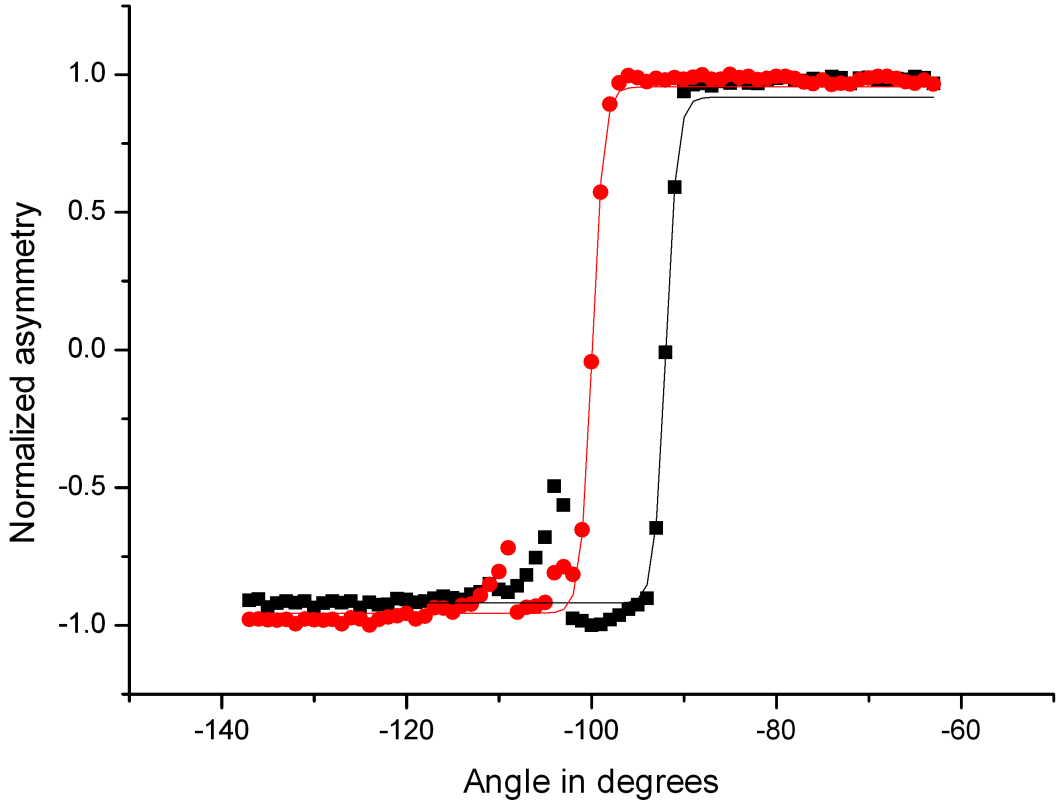

Figure 4.17: Graph of normalized asymmetry versus field rotation, showing data for scans with a fixed field of magnitude 100 mT rotated in the positive theta (red points) and negative theta (black points) directions, taken at room temperature. The field is rotated in the yz plane, while the wires are aligned parallel to the x direction. Lines indicate simultaneous fits to both data sets. The fit produced an easy axis value of -6° ± 3°, in agreement with figure 4.16.

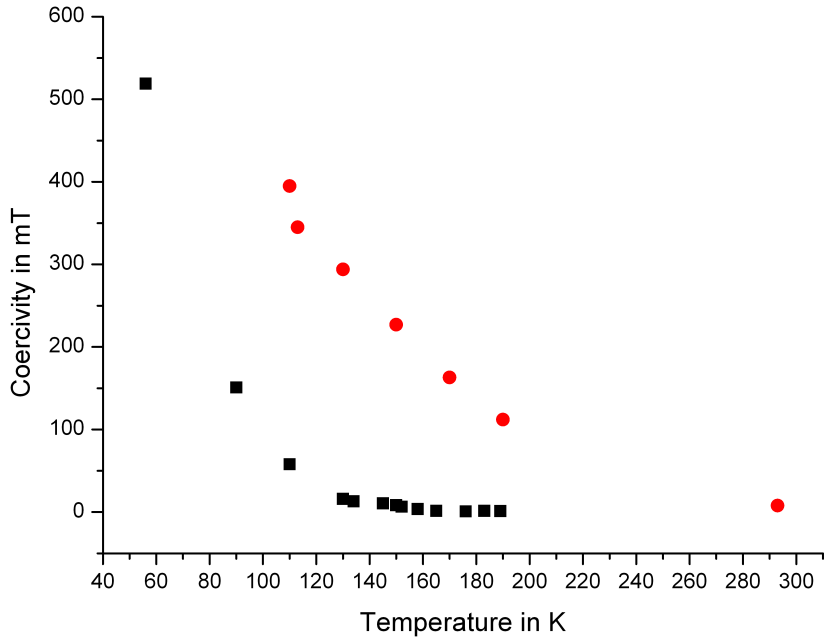

Figure 4.18: Plot of temperature versus coercivity for four wire (red circles) and three wire (black squares) samples capped with six monolayers of Au. It should be noted that above 158K, the 3 wire sample was super-paramagnetic, and hence coercivity values are zero, within error.

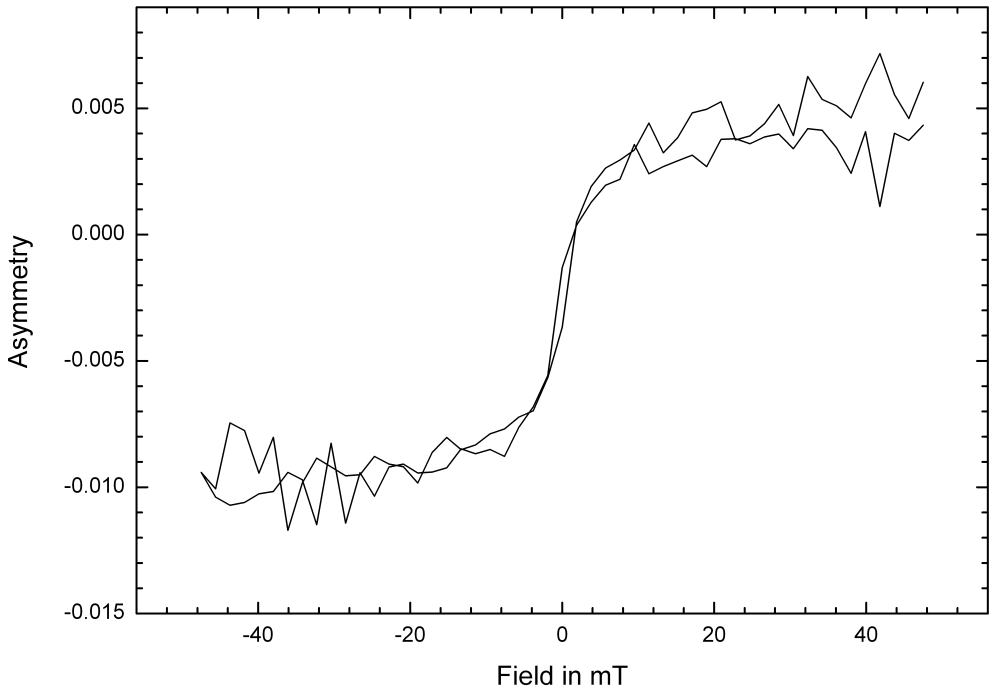

Figure 4.19: Magnetization curve for the three wire sample taken at 176 K.

discussed in section 4.2, a spin block system consists of a number of giant spins which are randomly flipped by thermal fluctuations. Cheng *et al.* [56] measured a similar temperature dependent coercivity in a system of uncapped Fe nanostripes grown on Pt(997) and applied the equation of magnetization motion provided by Glauber [58] to extract an equation for the temperature dependence of the coercivity:

$$H_c(T) = H_0 \omega \tau_0 exp\left(\frac{T_K}{T} N(T)\right) \tag{4.3}$$

Where H_c is the Curie temperature, H_0, ω and τ are constants specific to the system, T_K is related to the magneto-crystalline anisotropy constant K_1, T is the temperature and $N(T)$ is the temperature dependent spin block size. Thus, assuming that the $N(T)$ does not change much with temperature below T_b, the coercivity should show an exponential dependence with temperature, and the fit should produce values for K_1. Unfortunately, while an exponential function does produce reasonable fits to the data, the calculated values for K_1 do not make sense, varying randomly from sample to sample. The work published by Chen *et al.* had coercivity values measured over a large temperature range, from 40 K up to over 200 K. In the higher temperature regime, the exponential fit deviates from the data significantly. Most of the data sets presented here start at ∼100 K, due to limitations both in the available magnetic fields and with the cryostat available in MAXLAB. As a result, the fits are based largely on a temperature regime which shows deviation from the fit in the data presented by Cheng *et al.* The deviations could come from one of the approximations made in their model, for instance, the assumption that $N(T)$ does not have a significant temperature dependence.

4.4 Fits to Gaunt model of Coercivity versus temperature

Another approach is that proposed by Gaunt [59], who developed a model based on domain wall motion and pinning. In the course of this model, he describes two specific cases: one where the pinning sites are considered "weak" and one where the pinning is considered "strong". These two cases are defined by whether or not a pinning strength determinant, β_0 is less than or greater than 1, where $\beta_0 = 3f(8\pi\gamma b)^{-1}$, f is the maximum restoring force per pinning site, γ is the domain wall energy per unit area, and b is related to the interaction area of the pinning site. In the case of weak pinning, a linear relation is found between the coercivity and the temperature, while for the strong pinning case, there is a linear relationship between $H_c^{1/2}$and $T^{2/3}$.

Table 2: Least-squares R^2 values for fits to coercivity versus temperature data for the "weak" and "strong" pinning cases.

System	"Weak" R^2	"Strong" R^2
sample1 6w6ml	0.98	0.99
sample1 6w9ml	0.97	0.99
sample1 3w6ml	0.97	0.99
sample1 3w9ml	0.94	0.99
sample2 3w6ml	0.90	0.98
sample2 4w6ml	0.94	0.99

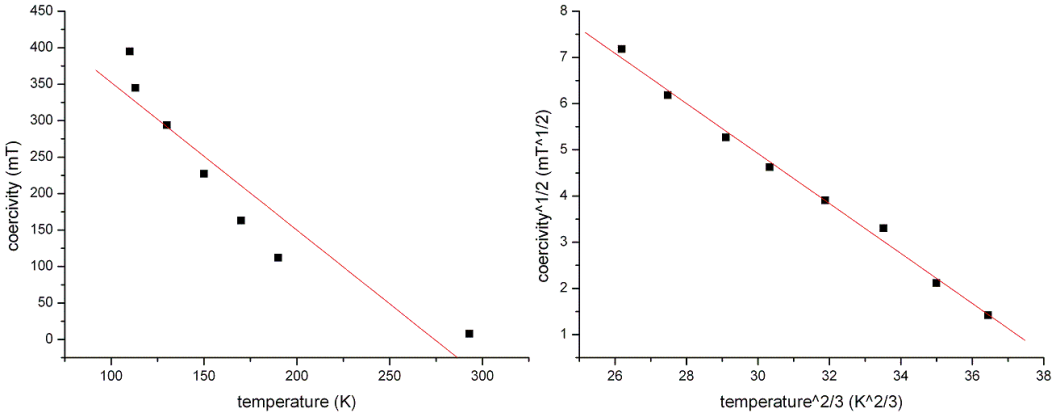

Figure 4.20: Linear fits for "weak" (left) and "strong" (right) pinning cases for the four wire, six monolayer sample.

Applying these relations to our data, the strong pinning case provides a better fit than the weak pinning case (Table 2). Unfortunately, neither can produce values which can be compared to other published results without additional information. However, this model is consistent with the measured angular dependence of the coercivity, and gives a reasonable explanation of the temperature dependence of the coercivity. Linear fits to temperature data plotted as either H_c versus T, or $H_c^{1/2}$ versus $T^{2/3}$, are shown in figures 4.20, 4.21, 4.22, 4.23, 4.24 and 4.25,.

The Gaunt model for the temperature dependence has an important implication for the samples under investigation, namely that there are many pinning sites present in the systems. Since any magnetic or structural inhomogeneity can act as a pinning site, the most likely candidate for a pinning site in the samples is a kink in the step on

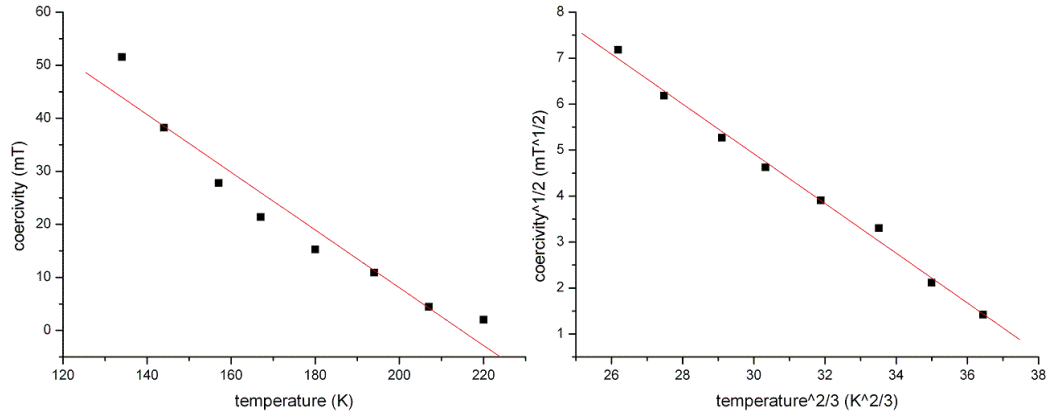

Figure 4.21: Linear fits for "weak" (left) and "strong" (right) pinning cases for the three wire, six monolayer sample (sample 1).

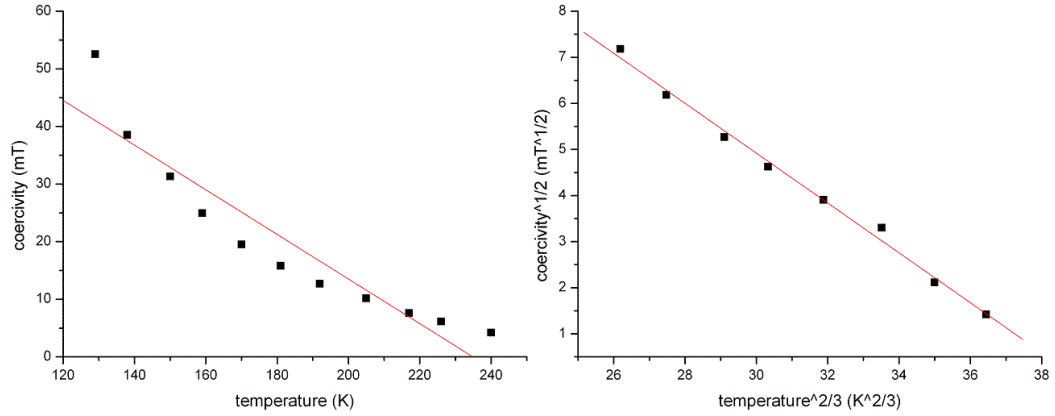

Figure 4.22: Linear fits for "weak" (left) and "strong" (right) pinning cases for the three wire, nine monolayer sample.

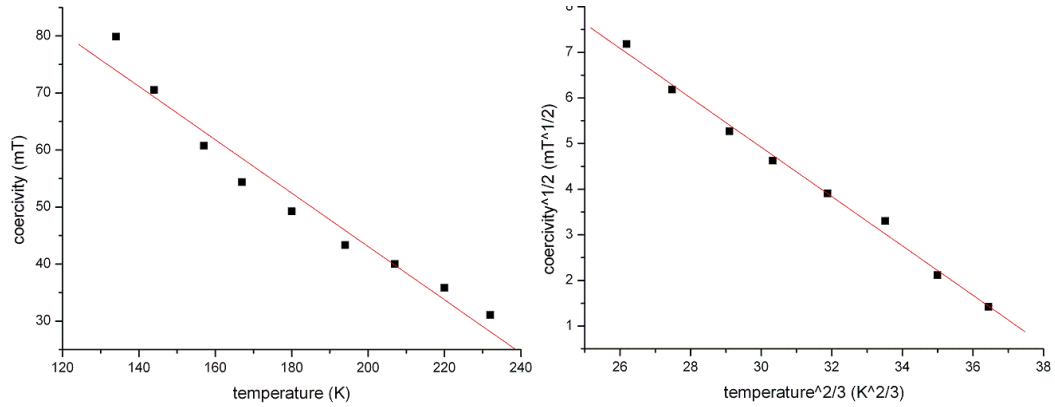

Figure 4.23: Linear fits for "weak" (left) and "strong" (right) pinning cases for the six wire, six monolayer sample.

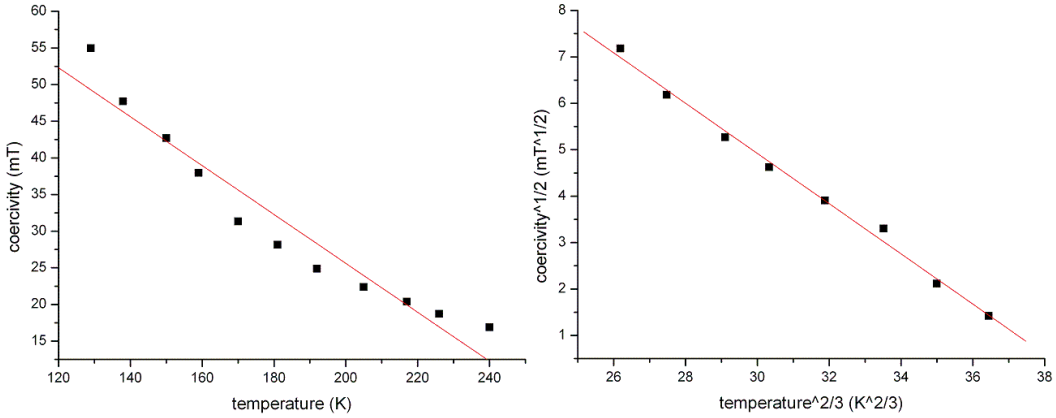

Figure 4.24: Linear fits for "weak" (left) and "strong" (right) pinning cases for the six wire, nine monolayer sample.

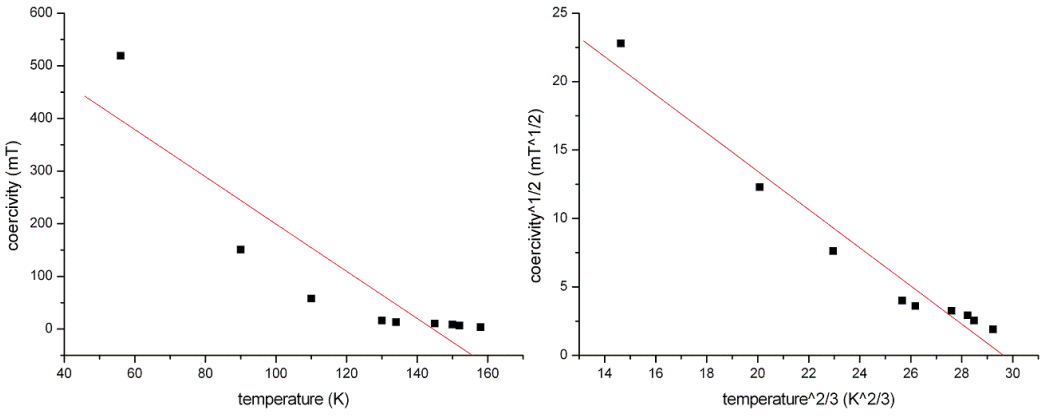

Figure 4.25: Linear fits for "weak" (left) and "strong" (right) pinning cases for the three atom wide Co wire, capped with six monolayers Au (sample 2).

the Pt substrate, and thus also in the nano wire. Since energetic considerations would suggest that the domain walls would move along the wires, and since there were no signs of contamination in the sample preparation, step kinks would appear to be the most likely pinning site present in the samples.

These are the first results from capped Co nanowire systems and further progress in the interpretation of the results depends on determining other key parameters of these systems, particularly the exchange stiffness, A, and the anisotropy constant, K_1, as these determine, for example, the domain wall energy ($\propto \sqrt{AK_1}$). An attempt was made to measure K_1, using fields of up to 1.1 T, applied at 76° to the easy axis, but the RAS-MOKE measurement detected no decrease in saturation signal. The very high MAE values associated with the Co wire systems make measuring K_1 quite difficult.

5 MOKE of Au-capped Co nanowires on Pt(997)

5.1 Overview

MOKE studies of Au-capped Co nanowires grown on a Pt(997) substrate were conducted using a Reflection Anisotropy Spectroscopy (RAS) system and a four-pole electromagnet. Three main measurements were carried out on two different samples. Spectroscopic studies allowed measurement of both the spectroscopic MOKE and RAS signal, although little structure apart from the magnetic signal was seen. Hysteresis loops revealed the magnetic behaviour of the samples at a fixed wavelength, chosen to optimise the signal-to-noise ratio, and rotating field measurements revealed both hysteretic and easy axis information at a fixed wavelength. Sample preparation has been described previously, and data were recorded for Co coverages of 0.52 ml and 0.78 ml, corresponding to 4 and 6 atom thick wires respectively. Strain in the optical cryostat windows prevented RAS-MOKE measurements at low temperatures and so the response of the capped four and six wire samples was measured, as these were ferromagnetic at room temperature. Results were compared to XMCD measurements, and small differences between MOKE and XMCD results were observed.

5.2 MOKE of four and six atom wide Co wires, capped with six monolayers of Au

A spectroscopic scan of the six wire sample showed no significant RAS signal below 3.5 eV, and a broad MOKE signal increasing into the UV (figure 3.18). The four wire sample showed a similar response. This is probably due to the fact that, because of their generally high plasmon resonances, metals only have broad structures in the optical range. On top of this, most metals have very similar dielectric functions in the optical range, which means that optical spectroscopies can have difficulty with the measurement of small amounts of metal deposited on another metal. In terms of signal-to-noise ratio, although the MOKE response decreases for decreasing energy, the reduced noise in the 2 eV range and the broadness of the MOKE response indicate that the signal-to-noise ratio for hysteresis measurements should be best at $\sim$2 eV, and hysteresis measurements and field rotation measurements were taken at this energy. Field rotation plots for four wire and six wire samples are shown below (figures 5.1,

5.2). The least squares fitting of the data used a model curve based on equation 2.28:

$$X^{\pm}(\theta) = -X^{\pm}_{sat}\cos\theta_M + \frac{2X^{\pm}_{sat}\cos\theta_M}{1 + exp[-sH\cos(\theta - \theta_M) - H_c]} \tag{5.1}$$

where $X^{\pm}$ is the measured signal (which is proportional to M), θ is the angle between the applied field and the surface normal, θ_M is the angle between the easy axis and the surface normal, s is the stiffness, H is the magnitude of the applied field, and H_c is the coercivity. The $\pm$ denotes field rotation in positive or negative direction. The two curves were then fitted simultaneously to produce values for H_c, s and θ_M. Errors were calculated by determining the change required in a given parameter to cause a 10% change in the residual, except in the case of the easy axis, where the error was determined by a systematic error in the direction of the applied field, which was determined using a Hall probe embedded in the sample holder. The resulting error was estimated at $\pm 3°$. Fitting error proved to be insignificant in comparison. Table 4 shows the results obtained from fitting six wire and four wire samples, with the field rotated in a plane parallel or perpendicular to the wires. For comparison, the results of a similar experiment using XMCD is included (figure 4.17). A small variation could be observed in the coercivities for repeated measurements on the same sample, and the results tabled are average results from at least three data sets with the associated error. One explanation for these variations is that, since the measurements were not done concurrently, slight variations in the temperature of the room from scan to scan could have an effect. From the temperature dependence of the coercivity measured with XMCD, there may be as much as a 1 mT/K temperature dependance in the coercivity.

5.3 Comparison between MOKE and XMCD results

In order to compare the results obtained from XMCD and MOKE experiments, hysteresis curves measured with the two techniques were fitted using equation 4.2. The curves were all measured at room temperature, and at normal incidence. Figures 5.3 and 5.4 show measured curves for four and six wire samples, while table 3 shows the hysteresis and stiffness values from the fits. It is apparent that the MOKE results show consistently slightly higher coercivity values, as well as consistently lower stiffness values compared to the XMCD results. This trend is also apparent in the field rotation scans (table 4), which shows values calculated from the average of at least 3 scans for each MOKE result. The XMCD result of the one measured XMCD field rotation

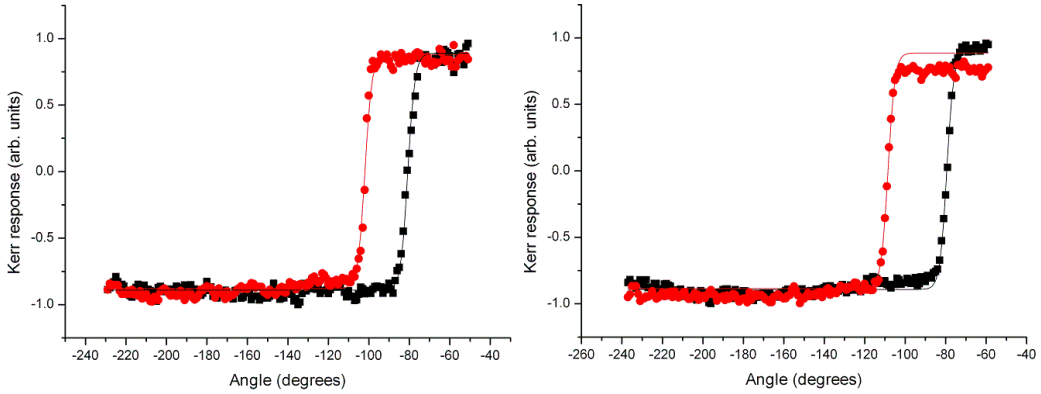

Figure 5.1: Field rotation scans in a plane perpendicular (left) or parallel (right) to the wires for four wire sample capped with six monolayers of Au. Plots show data (points) and fits (lines) for forward (black) and reverse (red) field rotation direction.

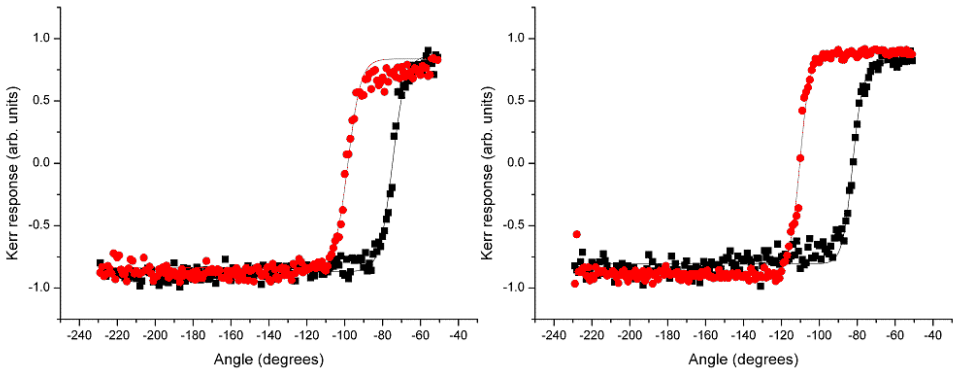

Figure 5.2: Field rotation scans in a plane perpendicular (left) or parallel (right) to the wires for six wire sample capped with six monolayers of Au. Plots show data (points) and fits (lines) for forward (black) and reverse (red) field rotation direction.

Table 3: Fitted values for MOKE and XMCD hysteresis loops

System	Coercivity (mT)	Stiffness (arb.)
MOKE 4w	13 ± 1	0.44 ± 0.05
XMCD 4w	11 ± 1	1.14 ± 0.05
MOKE 6w	18 ± 1	0.28 ± 0.05
XMCD 6w	15 ± 1	1.3 ± 0.05

scan is included for comparison. While the variations in coercivity between XMCD and MOKE measurements might be partially explained by the previously mentioned temperature dependence, the stiffness values were found not to vary significantly with temperature and so the large differences in the stiffness values must be caused by some other factor. The most obvious cause concerns what the two different techniques actually measure. While XMCD measures the magnetic response of the Co, MOKE will measure any magnetization from material within the penetration depth of the light - any induced magnetization in the Au cap or Pt substrate will be included. It is well known that induced spin polarization of Au capping layers occurs due to the interaction with magnetic Co layer [60], or in Pt due to ferromagnetic Ni layers [61]. Figures 5.3 and 5.4 highlight the difference in stiffness, while the coercivity values are relatively close. However, it should be noted that this would imply that the induced magnetization in the non-magnetic materials is switching slower then that of the cobalt, which seems counter-intuitive. Another parameter which could have an effect on the measured hysteresis loops is the time over which the loop is taken. However, the time taken for a loop was similar for both the MOKE and the XMCD measurements.

The results in tables 3 and 4 show that XMCD and RAS-MOKE produce consistent results. The easy axis direction of the capped four wire and six wire samples is perpendicular to the terrace of the Pt(997) substrate, in contrast to the uncapped structures. The XMCD measurements provide element-specific information, while the RAS-MOKE probes the total magnetic response of the system. The ease of measurement makes RAS-MOKE a powerful new tool for probing perpendicular magnetic anisotropy systems of fundamental and technological interest.

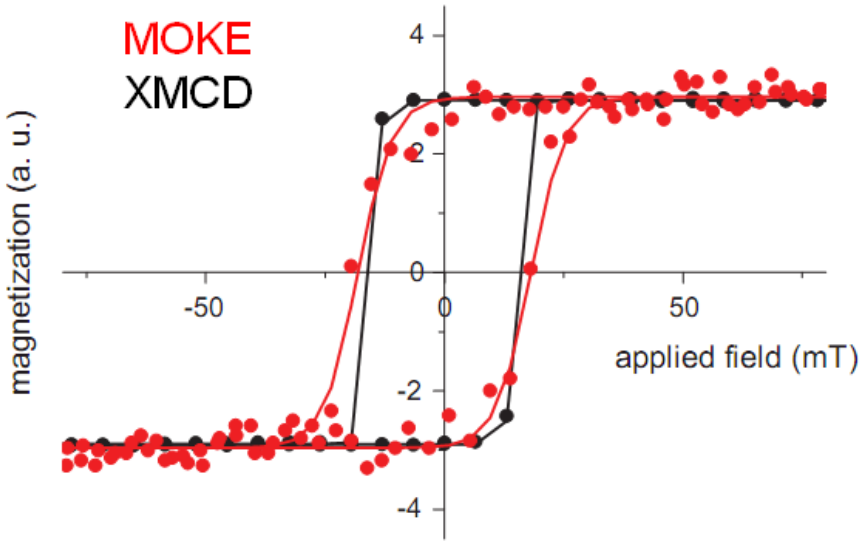

Figure 5.3: Graph of hysteresis curves measured with XMCD (black) and MOKE (red) on six wire Co sample capped with six monolayers Au. Graphs show measured data (points) and fits from equation 4.2 (lines). XMCD data were taken at the L_3 edge, while the MOKE data were recorded at 2 eV.

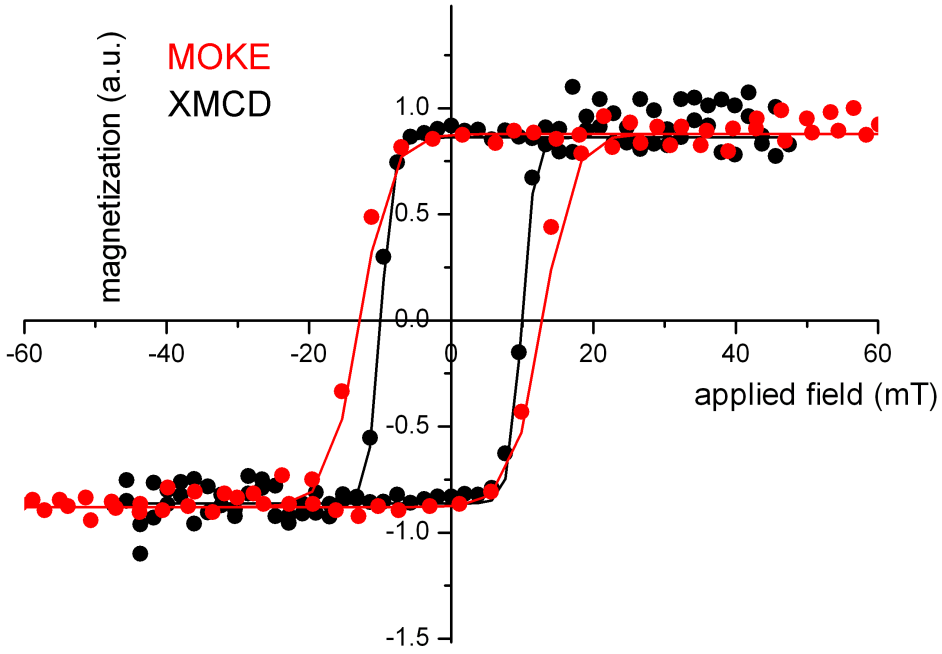

Figure 5.4: Graph of hysteresis curves measured with XMCD (black) and MOKE (red) on four wire Co sample capped with six monolayers Au. Graphs show measured data (points) and fits from equation 4.2 (lines). XMCD data were taken at the L_3 edge, while the MOKE data were recorded at 2 eV.

Table 4: Fitted values for MOKE and XMCD Field rotation scans

System	Coercivity (mT)	Easy axis angle (degrees)	Stiffness (arb.)
6wperp	19 ± 1	-6 ± 3	0.42 ± 0.05
6wpara	18 ± 1	3 ± 3	0.28 ± 0.05
4wperp	12 ± 1	-8 ± 3	0.43 ± 0.05
4wpara	12 ± 1	-1 ± 3	0.39 ± 0.05
xmcd4wperp	7 ± 1	-6 ± 3	0.93 ± 0.05

6 MSHG of Au-capped Co structures on Pt(997) and Au-capped Fe structures on vicinal W(110)

6.1 Overview

In this section, the results of MSHG studies of Au-capped Co structures on Pt(997) and Au-capped Fe structures on vicinal W(110) are presented. While both systems share many similarities, there are also a number of significant differences. The easy axis of the W(110)/Fe/Au system lies in the surface plane, perpendicular to the Fe stripes and thus RAS-MOKE provides no useful information. In contrast, while the perpendicular magnetization exhibited by the Pt(997)/Co/Au system allows RAS-MOKE measurements, the symmetry of the system is such that the MSHG signal is suppressed by crystallographic contributions. The MSHG results of L. Carroll are extended, and simultaneous fitting of hysteresis and temperature curves allows for the extraction of magnetic information from multiple regions of a nanostructured magnetic sample.

6.2 MSHG of Au-capped Co structures on Pt(997)

MSHG scans were carried out on a six atom wide Co wire capped with six monolayers of Au to investigate the possibility of measuring a magnetic response from the sample. The response from a Pt(997) system with a pseudomorphic overlayer will consist of a step contribution of 1m symmetry, and a terrace contribution of 3m symmetry. Since the samples exhibit strong perpendicular magnetic anisotropy, the magnetization is nearly along the z direction. As discussed in section 2.4, the SHG response can be

separated into a crystallographic and a magnetic contribution, χ^C and χ^M. Both the 3m and 1m symmetries will have a number of possible crystallographic and magnetic tensor components contributing to the overall second harmonic signal. These tensor elements are listed in table 5, for a system with polar magnetization (along the z axis). The number of components can be further reduced through choice of measurement geometry. Use of a normal incidence geometry will remove all z dependent components, while further components can be removed through the orientation of the output polarization. In the course of this study, two measurement geometries were used: the sample was oriented with the steps aligned parallel to the y direction, at normal incidence, with the output polarization aligned along the y direction (parallel to the steps) or along the x direction (perpendicular to the steps). The magnetic field was applied along the z direction. Since the SHG response is the coherent sum of all probed tensor components, it is not possible to separate two identical tensor components which are generated by two different symmetry groups. As a result, the tensor components present in the parallel case are: χ_{yxy}, χ_{yxxZ}, and χ_{yyyZ}. In the perpendicular case, the components will be:χ_{xxx}, χ_{xyy} and χ_{xxyZ}. It should be noted that the crystallographic components will consist of step, terrace, and capping layer contributions. For a 2mm terrace, capped with an isotropic capping layer, the crystallographic contribution is purely step related, as discussed in section 6.3. From section 2.4, the SHG intensity is given by:

$$I(2\omega;\varphi,\pm M_z) \propto \left|(A\cos^2\varphi + B\sin^2 + C\sin 2\varphi)E(\omega)^2\right|^2 \tag{6.1}$$

where A,B and C are combinations of the effective tensor components.

Scans were carried out at normal incidence with the output polarizer aligned parallel or perpendicular to the wires, which were aligned with the y axis (figure 2.6), and rotating the input polarizer angle, φ. In the process of making the measurements, a small drift in the signal during the course of the measurement was observed. The source of this roughly linear drift was hard to ascertain, but a drift in the laser power was ruled out as a cause. This drift was removed by assuming that it was linear, such that two scans taken sequentially (figure 6.1) with the input polarization rotated in opposite directions could be averaged, removing the drift. While this did indeed remover the drift, it then caused an offset in the levels of any two averaged scans (such as scans taken with the applied field in a positive and then negative direction, figure

Table 5: Non-zero tensor components for 1m and 3m symmetry, with magnetization in z direction [62, 63].

Element and symmetry	Non-zero components
χ^C 1m	$\chi_{xxx}, \chi_{xyy}, \chi_{xzz}, \chi_{xzx} = \chi_{xxz}, \chi_{yyz} = \chi_{yzy},$ $\chi_{yxy} = \chi_{yyx}, \chi_{zxx}, \chi_{zyy}, \chi_{zzz}, \chi_{zzx} = \chi_{zxz}$
χ^C 3m	$\chi_{xxx} = -\chi_{xyy} = -\chi_{yxy} = -\chi_{yyx},$ $\chi_{xzx} = \chi_{xxz} = \chi_{yyz} = \chi_{yzy}, \chi_{zxx}, \chi_{zyy}, \chi_{zzz}$
χ^M 1m	$\chi_{xyzZ} = \chi_{xzyZ}, \chi_{xxyZ} = \chi_{xyxZ}, \chi_{yxxZ}, \chi_{yyyZ}, \chi_{yzzZ},$ $\chi_{yzxZ} = \chi_{yxzZ}, \chi_{zzyZ} = \chi_{zyzZ}, \chi_{zxyZ}, = \chi_{zyxZ}$
χ^M 3m	$\chi_{xyzZ} = \chi_{xzyZ} = -\chi_{yzxZ} = -\chi_{yxzZ},$ $\chi_{xxyZ} = \chi_{xyxZ} = \chi_{yxxZ} = -\chi_{yyyZ}$

6.2). The scans for positive and negative applied field were normalized to the first peak to remove this offset. This method of normalization is valid, since the shape of the expected magnetic response is such that a rigid shift will not affect the magnetic part of the signal. Figure 6.8 shows the magnetic response for a Au-capped Fe film grown on vicinal W(110): the Co response is expected to also show differences between opposite magnetizations, either as an intensity change, or as an angular shift. Two scans for positive and negative magnetization were then recorded, and the MHG asymmetry, or contrast, $\eta(\varphi)$, calculated:

$$\eta(\varphi) = \frac{I(2\omega; \varphi, +M_z) - I(2\omega; \varphi, -M_z)}{I(2\omega; \varphi, +M_z) + I(2\omega; \varphi, -M_z)} \tag{6.2}$$

The magnetic response of the system should be visible in such a plot. Indeed, a difference is seen (figure 6.4). However, figure 6.5 shows a number of attempted hysteresis loops taken at various values of φ, around the maxima in the asymmetry. No magnetic signal is seen in these loops. This suggests that the small differences seen are due to effects other then the sample magnetization. In terms of magnitude, the asymmetry signal is very small compared to the W(110)/Fe/Au system (figure 6.8).

The lack of a detectable magnetic signal does not preclude the existence of one. Rather, it suggests that the magnetic component of the SHG response is small in comparison to the crystallographic response, such that the magnetic signal is overwhelmed. This particular system consists of a terrace crystallographic 3m symmetry contribution and a 1m symmetry step contribution. The LEED pattern exhibited by the capped

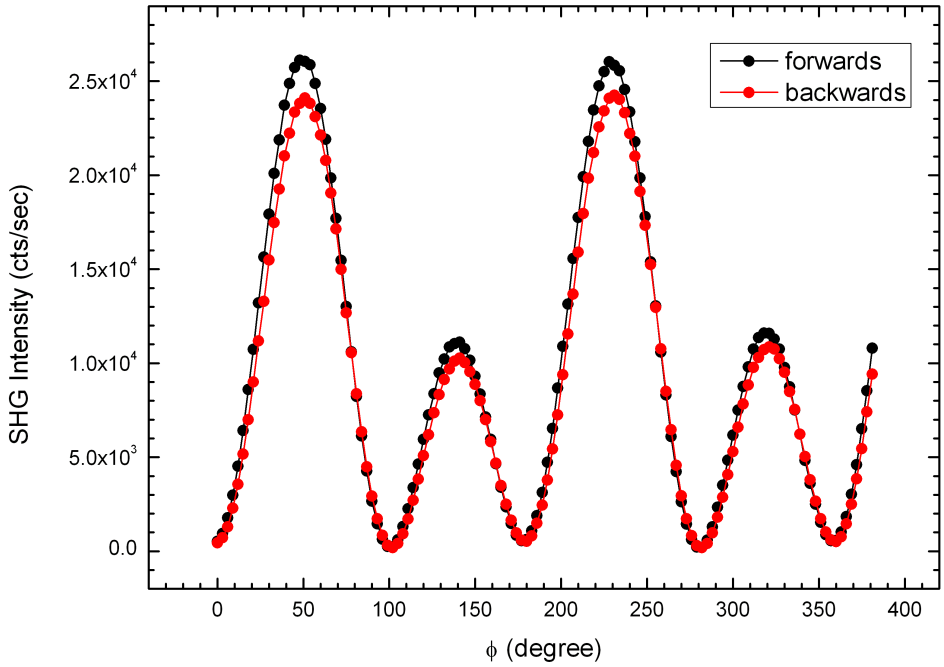

Figure 6.1: Graph of MSHG plot taken with the output polarizer perpendicular to the wires, with the input polarizer rotated in a forwards or backwards direction. The difference between the two scans is greatest for small angles, where the largest amount of time has passed between measurements of a given point.

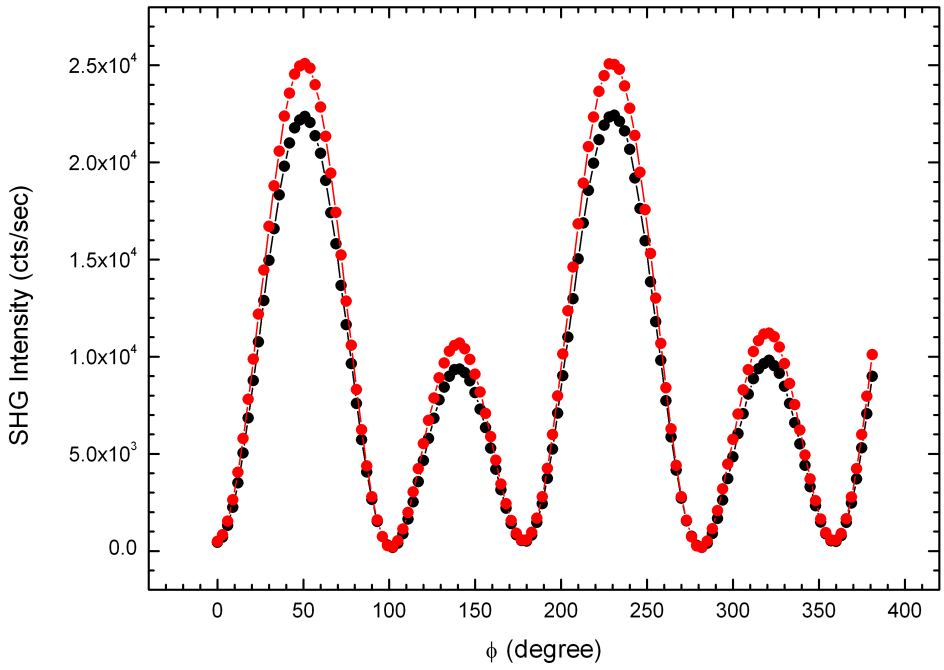

Figure 6.2: Graph of MSHG plot taken with the output polarizer perpendicular to the wires, for the applied field in two opposite directions along the z axis.

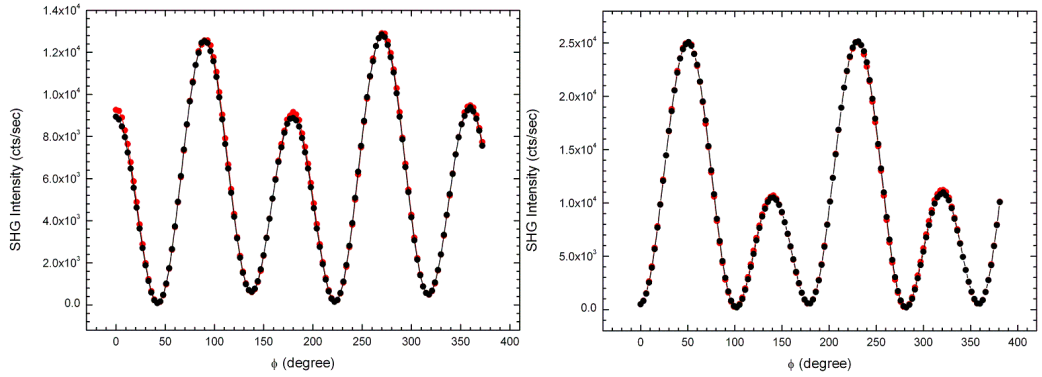

Figure 6.3: Graphs of the SHG response with the output polarizer aligned perpendicular (right) or parallel (left) to the wires. Scans were taken with the magnetic field applied in the positive (black) and negative (red) z directions.

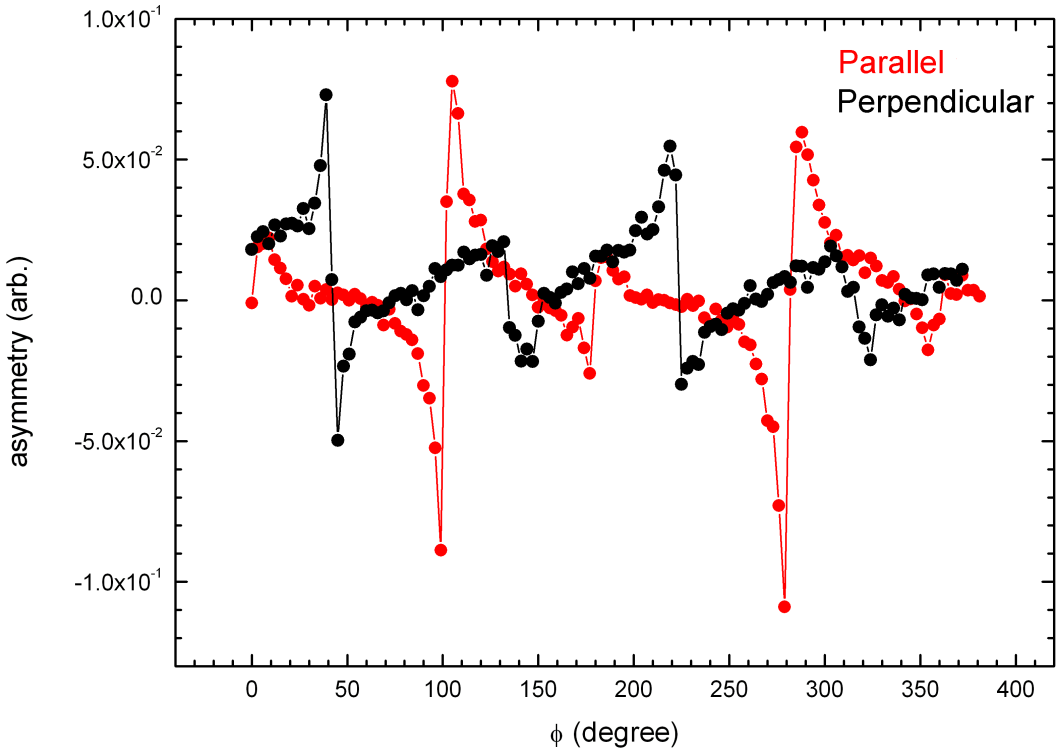

Figure 6.4: Graph of MSHG asymmetry, calculated using equation 6.2. Asymmetries for the output polarizer aligned parallel (red) and perpendicular (black) to the wires are shown.

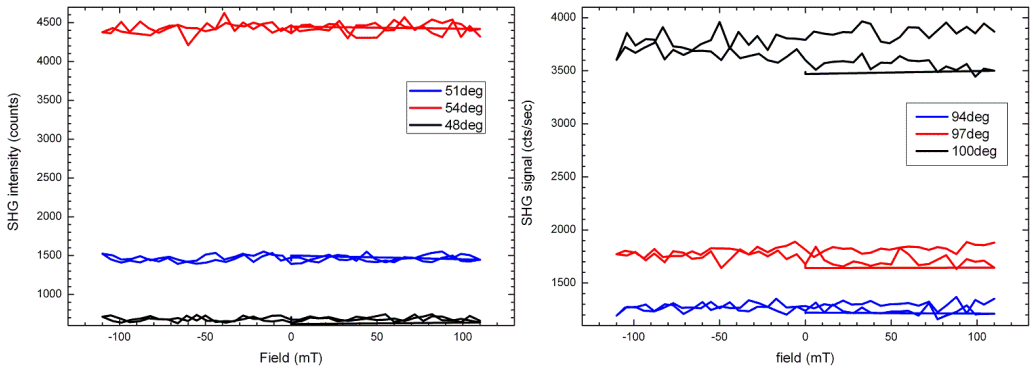

Figure 6.5: Graphs of attempted hysteresis loop measurements at a number of input polarizer angles near the maxima in the asymmetry plots, for the output polarizer perpendicular (right) or parallel (left) to the wires.

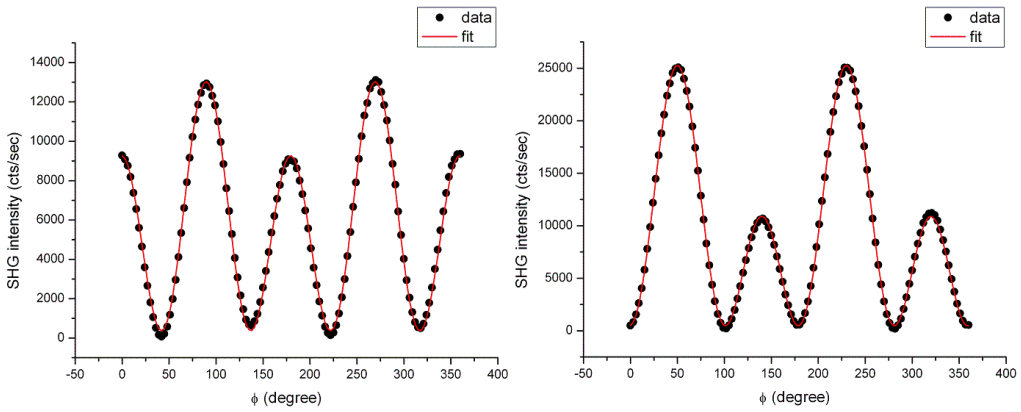

Figure 6.6: Graphs of the SHG response with the output polarizer aligned perpendicular (right), or parallel (left), to the wires: graphs show data (black points) and fits (red lines) to equations

sample after preparation indicates that the Au cap is crystalline, and that the Au/air interface may also contribute to the signal. The size of the crystallographic signal relative to the magnetic signal, when compared to a system with only a 1m step crystallographic contribution such as the system described in section 6.3, is expected to be very large. However, the data can still be fitted to determine relative sizes of crystallographic components (figure 6.6). The SHG intensity perpendicular and parallel to the wires is given by:

$$I_x(2\omega, \varphi, \pm M_Z) \propto |xxx \cos^2\varphi + xyy \sin^2\varphi \pm xxyZ \sin 2\varphi M_Z|^2 \tag{6.3}$$

$$I_y(2\omega, \varphi, \pm M_Z) \propto |yxy \sin 2\varphi \pm \{yxxZ \cos^2\varphi + yyyZ \sin^2\varphi\} M_Z|^2 \tag{6.4}$$

where χ_{ijkL} has been replaced with $ijkL$ for clarity. From equation 6.1, for I_x, $A \propto xxx$, $B \propto xyy$ and $C \propto xxyZM_Z$, while for I_y, $A \propto yxxZM_z$, $B \propto yyyZM_z$ and $C \propto yxy$. Fitting for I_x returns a value of zero for C, which shows that the magnetic component is vanishingly small. the ratio of A to B, which corresponds to $\frac{xxx}{xyy}$ is 0.84. For I_y A fits to zero, and the ratio of B to C, which corresponds to $\frac{yyyZM_z}{yxy}$ is 0.43. This is puzzling, since if the magnetic contribution was indeed nearly half the size of the crystallographic, a hysteresis curve should have been easily measurable. The only explanation for this result is the introduction of another crystallographic contribution - either a χ_{yyy} or a χ_{yxx} term. This may suggest that the mirror plane in the sample has been removed, although there has been no evidence of this detected with other techniques. Further investigation is required to determine the cause of this signal.

6.3 MSHG of Au-capped Fe structures on vicinal W(110)

Although the MSHG work on the Au-capped Co structures resulted in no appreciable magnetic signal, a relatively large magnetic signal has been measured previously from samples which consisted of Fe deposited on a vicinal W(110) crystal, which was then capped with ∼16 nm of Au [64]. The samples were prepared in a similar manner to the Co on Pt(997) samples. The vicinal W(110) single crystal, offcut 1.4° in the $[1\bar{1}0]$ direction, was cleaned by thermal cycling in 5×10^{-8} mbar of O_2 and then flashing to 2200 K until a sharp 1×1 LEED pattern was observed, with no residual C or O contamination visible with AES. Fe was then deposited onto the sample at room temperature using an e-beam evaporator, and the sample was then annealed for 5 min

Table 6: Non zero tensor components for 1m and 2mm symmetry with magnetization in the x direction, after [64].

Element and symmetry	Non-zero components
χ^C 1m	$\chi_{xxx}, \chi_{xyy}, \chi_{xzz}, \chi_{xzx} = \chi_{xxz}, \chi_{yyz} = \chi_{yzy},$ $\chi_{yxy} = \chi_{yyx}, \chi_{zxx}, \chi_{zyy}, \chi_{zzz}, \chi_{zzx} = \chi_{zxz}$
χ^C 2mm	$\chi_{xzx} = \chi_{xxz}, \chi_{yzy} = \chi_{yyz},$ $\chi_{zxx}, \chi_{zyy}, \chi_{zzz}$
χ^M 1m	$\chi_{xyzX} = \chi_{xzyX}, \chi_{xxyX} = \chi_{xyxX}, \chi_{yxxX}, \chi_{yyyX}, \chi_{yzzX},$ $\chi_{yzxX} = \chi_{yxzX}, \chi_{zzyX} = \chi_{zyzX}, \chi_{zxyX}, = \chi_{zyxX}$
χ^M 2mm	$\chi_{xxyX} = \chi_{xyxX}, \chi_{yxxX}, \chi_{yyyX}$ $\chi_{yzzX}, \chi_{zzyX} = \chi_{zyzX}$

at 800 K to produce well-ordered nanostripes. The sample was then capped at room temperature with 30-40 ML (12-16nm) of Au. Unlike the Pt(997) sample, no LEED pattern was visible after capping, indicating a disordered top Au interface. The MSHG response of a range of Fe thicknesses (3 ML, 2 ML, 1 ML, 0.75 ML, 0.5 ML, 0.25 ML) was measured and, using a simplified normal incidence geometry to limit the number of contributing tensor components, magnetization curves were measured. For some samples, two unique curves were seen, depending on the polarization of the incident light. These curves were extracted using the methodology described in section 2.4. Temperature curves were also measured although, due to the complex nature of the MSHG response, it was not clear how best to extract information from them. The present work is a continuation of the work carried out by Carroll [64], and relates to the simultaneous fitting of magnetization curves and temperature curves measured by Carroll in order to extract information on properties such as Curie temperatures, hysteresis and softness values for multiple magnetic regions in a nanostructured sample. The magnetic response and contrast measured at 80 K are shown in figure 6.8 for a three monolayer Fe film grown on a vicinal W(110) crystal, capped with Au. The asymmetry was calculated using equation 6.2, and shows two values for φ where the asymmetry and signal-to-noise are large, at $\varphi \approx 0°$ and $\varphi \approx 90°$ (and symmetry related positions).

Figure 6.7 shows the 5 possible magnetic regions in this type of magnetic sam-

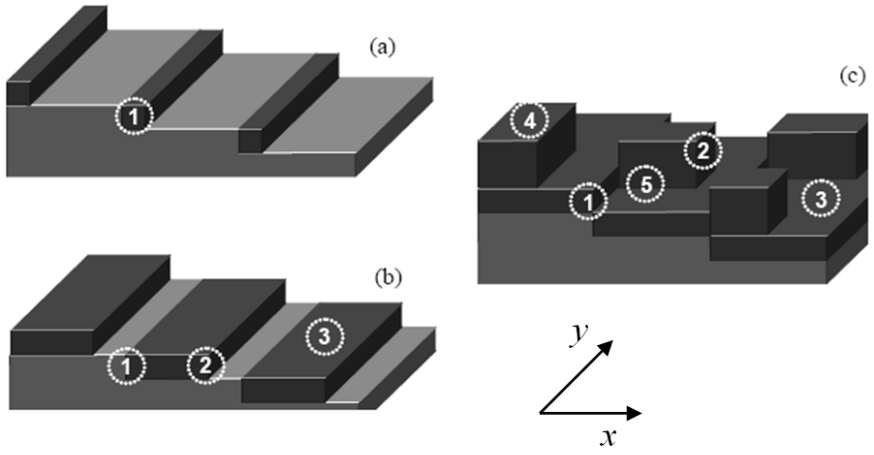

Figure 6.7: Diagram of different magnetic regions present in the nanostructured samples. Numbers denote atom which are in a unique electronic environment, after [10].

ple that could give rise to an MSHG signal. Additionally, for an integer monolayer pseudomorphic film, the substrate interface and top interface (be it a vacuum interface or a capping layer interface) have distinct electronic properties, and can therefore have distinct magnetic properties. MSHG can distinguish between these regions via their differing symmetries. In the case of the Fe on vicinal W(110), there are two distinct symmetry groups involved: terrace atoms (region 3 in figure 6.7) will have 2mm symmetry, while step atoms (regions 1 and 2 in figure 6.7) will have 1m symmetry. Additionally, it is known that the magnetization is in plane, perpendicular to the step [6–8]. Table 6 shows the non-zero tensor elements for this system. In order to simplify measurements, a normal incidence geometry was adopted, with the input polarization at an angle φ to the x axis, the steps aligned with the y axis and the magnetization along the x axis. For this measurement geometry, with the output polarization aligned with the y axis, there are only 3 tensor components which will contribute to the MSHG signal: χ_{yxy}, χ_{yxxX} and χ_{yyyX}. χ_{yxy} will come only from areas of the sample with 1m symmetry (steps and edges), while the magnetic components can have contributions from both 1m and 2mm symmetry groups. The MSHG intensity for y output polarization for a sample with different magnetic regions, n, for this experimental configuration can be written as:

$$I_y(2\omega;\varphi,\pm M_X) \propto \left| \sum_{(n)} yxy^{(n)} \sin 2\varphi \pm \{yxxX^{(n)} \cos^2\varphi + yyyX^{(n)} \sin^2\varphi\} M_X^{(n)} \right|^2 \quad (6.5)$$

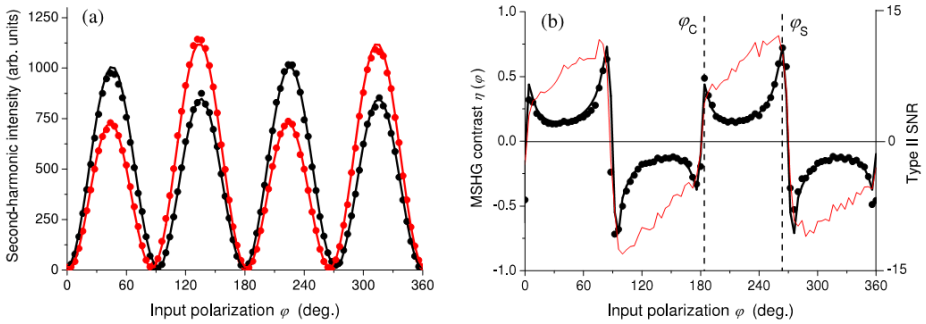

Figure 6.8: Graphs of (a) MSHG response for field in the positive x (black) and negative x (red) directions. (b) Asymmetry (black line) and signal-to-noise (right, red line) calculated from (a). Results are from a 3ml Fe film grown on a vicinal W(110) crystal, capped with Au and measured at 80 K, after [10].

where χ_{ijkL} has been shortened to $ijkL$ for simplicity. For centrosymmetric hysteresis loops, the difference signal, $\Delta I_y^{\pm}$, using the second method described in section 2.4, can be written as:

$$\begin{aligned}\Delta I_y^{\pm}(2\omega;\varphi,H) &\equiv I^{\pm}(2\omega;\varphi,H) - I^{\mp}(2\omega;\varphi,-H) \\ &\propto 4\sin 2\varphi\cos^2\varphi \sum_{n,n'} |yxy^{(n)}||yxxX^{(n')}|cos(\Delta\theta_{yx}^{nn'} M_X^{\pm(n')}) \\ &+ 4\sin 2\varphi\sin^2\varphi \sum_{n,n'} |yxy^{(n)}||yyyX^{(n')}|cos(\Delta\theta_{yy}^{nn'} M_X^{\pm(n')})\end{aligned} \tag{6.6}$$

where I^+ has H increasing from an initial negative value, I^- has H decreasing from an initial positive value, and $\Delta\theta_{yi}^{nn'} = \theta_{yxy}^{n} - \theta_{yiiX}^{n'}$, where θ is the complex phase factor of the tensor components [10]. It is now apparent that choosing φ close to 0° or 90° will limit the magnetic contributions to a single component per region, $yxxX^{(n')}$ and $yyyX^{(n')}$, respectively. Hysteresis loops extracted in this manner can then be fitted with equation 5.1. As is found in the case of MOKE measurements, the absolute magnetization cannot be determined from such a measurement without additional information, but both the stiffness, s and the coercivity, H_c can be found. If two loops measured at close to 0° or 90° are not identical, bar a scaling factor, then the signal must be a result of two different responses from two different magnetic regions. The expressions for asymmetry of these two polarization cases, $\varphi \approx 0°$ and $\varphi \approx 90°$, can be written as:

$$A_{\varphi\approx 0} \equiv \frac{I_y^+ - I_y^-}{I_y^+ + I_y^-}$$

$$= \frac{4\varphi \sum_{n,n'} |yxy^{(n)}||yxxX^{(n')}| \cos(\Delta\theta_{xx}^{nn'}) M^{(n')}}{4\varphi^2 \sum_{n,n'} |yxy^{(n)}||yxy^{(n')}| \cos(\Delta\theta_{yxy}^{nn'}) + \sum_{n,n'} |yxxX^{(n)}||yxxX^{(n')}| \cos(\Delta\theta_{yxxX}^{nn'}) M^{(n)} M^{(n')}} \tag{6.7}$$

$$A_{\varphi\approx \frac{\pi}{2}} = \frac{4(\frac{\pi}{2} - \varphi) \sum_{n,n'} |yxy^{(n)}||yyyX^{(n')}| \cos(\Delta\theta_{yy}^{nn'}) M^{(n')}}{4(\frac{\pi}{2} - \varphi)^2 \sum_{n,n'} |yxy^{n}||yxy^{(n')}| \cos(\Delta\theta_{yxy}^{nn'}) + \sum_{n,n'} |yyyX^{(n)}||yyyX^{(n')}| \cos(\Delta\theta_{yyyX}^{nn'}) M^{(n)} M^{(n')}} \tag{6.8}$$

Equations 6.6, 6.7 and 6.8 can be used, simultaneously, to fit two hysteresis loops, taken at φ close to 0° and 90°, and a temperature dependence curve, where the asymmetry, η, is recorded as the temperature is varied around the Curie temperature [13]. The contribution from the different regions to the temperature curve can be extracted assuming, as a first approximation, that the Curie transition has a sigmoidal shape, with a "stiffness" parameter, σ. Table 7 shows the results of simultaneous least-squares fitting for five different regions: a single region on a 0.25 ML Fe film, two regions on a 0.75 ML film and two regions on a 2 ML Fe film. The errors given were calculated as the deviation in a given value required to cause a 5% deviation in the residual.

Figures 6.9, 6.10 and 6.11 show that simultaneous loops and temperature dependent fits can be obtained. This indicates that the temperature dependence of the tensor components are either small or largely canceled between the numerator and denominator in equations 6.7 and 6.8. The figures and table 7 show that two magnetic regions can be identified for the 0.75 ML Fe and the 2 ML Fe coverages. For 0.75 ML Fe, the opposite phases of the tensor components produce a partial cancellation of the MSHG signal, which is removed as the sample temperature increases above $\sim$ 140 K, the effective Curie temperature of region 1. This accounts for the increase in signal, prior to the decrease at higher temperatures. This is not observed for the 2 ML Fe sample because the phases are of the same sign.

It is interesting to speculate on the origin of the two magnetic regions. It appears possible that MSHG allows magnetic step and terrace sites to be distinguished. This would explain two regions for the 0.75 ML Fe and the 2 ML Fe (the latter grows layer by layer). For 0.25 ML Fe, it may be that either the signal-to-noise ratio is not good enough, or that the temperature was too high to identify a second region. For 0.75 ML Fe, if the two "regions" correspond to intra-wire and inter-wire coupling, then the

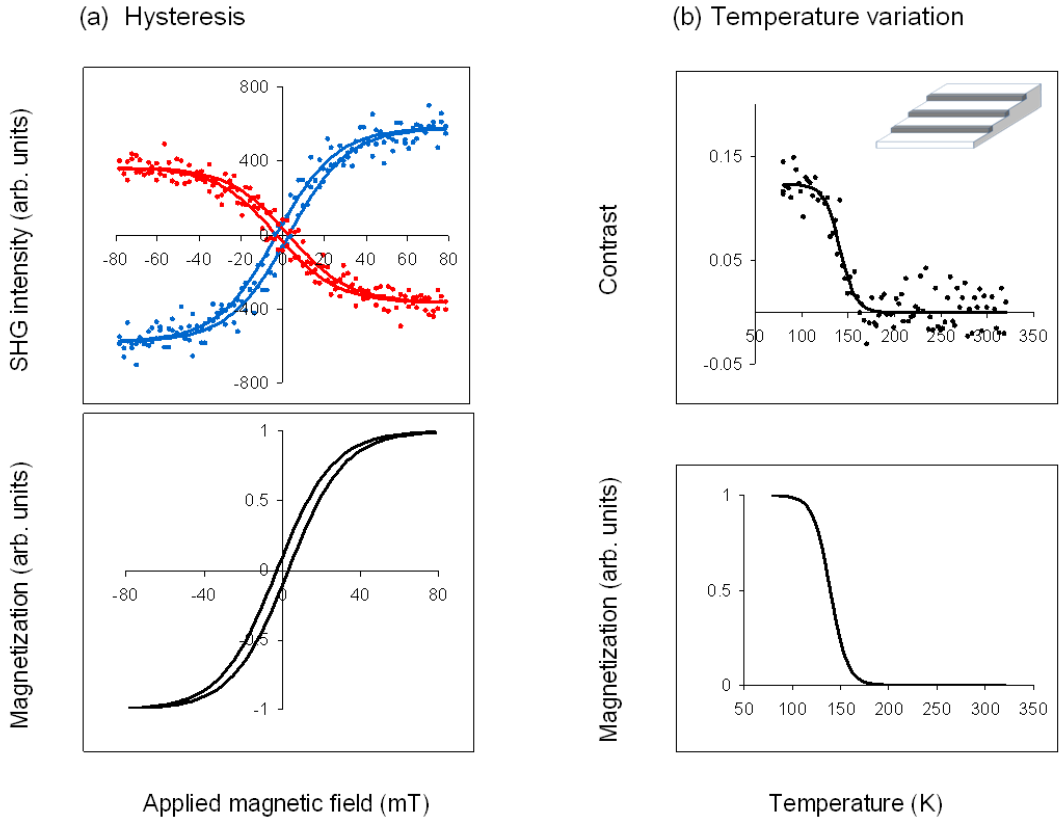

Figure 6.9: (a) NI MSHG y-polarized intensity difference, ΔI_y, at 80 K and fits (solid lines), together with the resulting hysteresis curve (below), from Au-capped 0.25 ML Fe films grown on vicinal W(110): $\varphi \approx 90°$ (red),$\varphi \approx 90°$ (blue) (b) Temperature variation of the MSHG contrast and simultaneous fit, together with extracted magnetization curve (below). Inset: schematic of 10 atom wide Fe stripes grown out from the step edge (capping by Au not shown).

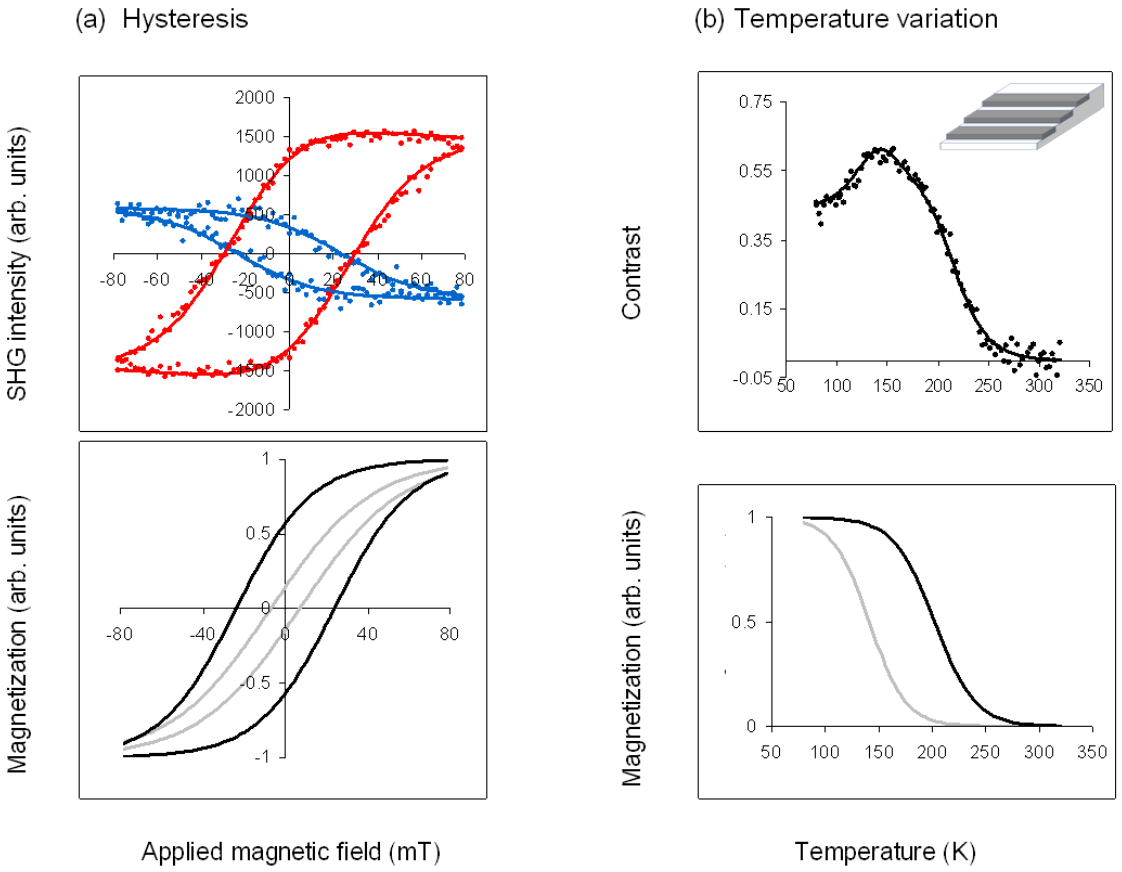

Figure 6.10: (a) NI MSHG y-polarized intensity difference, ΔI_y, at 80 K and fits (solid lines), together with the resulting hysteresis curves (below), from Au-capped 0.75 ML Fe films grown on vicinal W(110): $\varphi \approx 90°$ (red),$\varphi \approx 90°$ (blue) (b) Temperature variation of the MSHG contrast and simultaneous fit, together with extracted magnetization curves (below). Inset: schematic of 30 atom wide Fe stripes grown out from the step edge (capping by Au not shown).

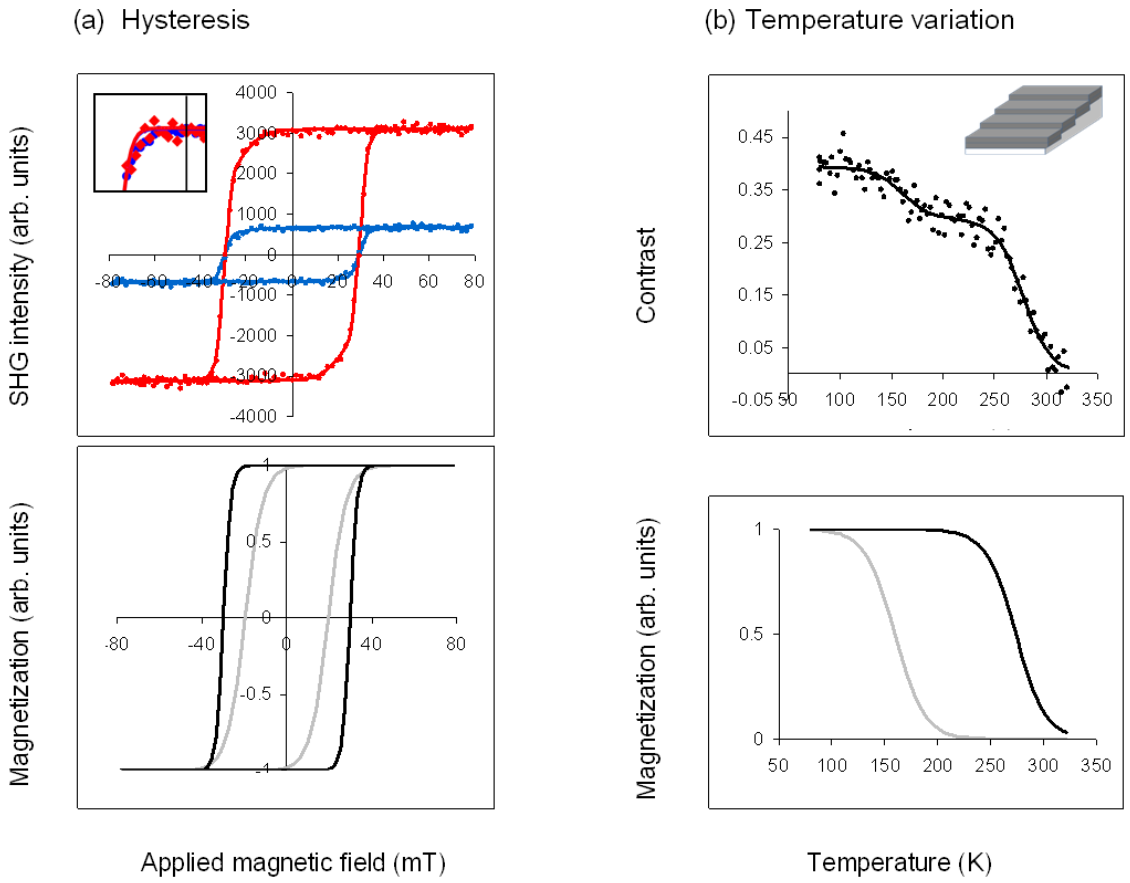

Figure 6.11: (a) NI MSHG y-polarized intensity difference, ΔI_y, at 80 K and fits (solid lines), together with the resulting hysteresis curves (below), from Au-capped 2 ML Fe films grown on vicinal W(110): $\varphi \approx 90°$ (red),$\varphi \approx 90°$ (blue). The inset is an enlarged view, showing the difference between the fits for two angles. (b) Temperature variation of the MSHG contrast and simultaneous fit, together with extracted magnetization curves (below). Inset: schematic of 2 ML Fe coverage (capping by Au not shown).

Table 7: Fitted values of the parameters for the three samples. The estimated error in the last figure is given in parenthesis. The coercivity was measured at 80 K.

	0.25 ML Fe	0.75 ML Fe	0.75 ML Fe	2.0 ML Fe	2.0 ML Fe
	1^{st} component	1^{st} component	2^{nd} component	1^{st} component	2^{nd} component
$yxxX$	$0.19(1)e^{i68(1)^\circ}$	$0.03(1)e^{i140(3)^\circ}$	$0.00(1)e^{i44(3)^\circ}$	$2.67(2)e^{i34(1)^\circ}$	$0.2(2)e^{i0(15)^\circ}$
$yyyX$	$0.17(1)e^{i102(1)^\circ}$	$0.12(1)e^{i157(1)^\circ}$	$0.16(1)e^{i99(1)^\circ}$	$0.10(1)e^{i84(1)^\circ}$	$0.018(2)e^{i38(5)^\circ}$
H_c mT	3(1)	24(1)	7(2)	30(1)	20(1)
s mT^{-1}	0.07(1)	0.05(1)	0.04(1)	0.6(1)	0.2(1)
T_c K	140(10)	202(3)	141(5)	274(4)	160(10)
σ K	9(5)	19(2)	17(3)	14(4)	10(10)

2 ML Fe sample should only show a single region. Theoretical modeling is required at this stage to make further progress.

7 Conclusions and future work

7.1 Conclusions

The magnetic properties of Au-capped Co nanowires and nanostripes were probed using XMCD, RAS-MOKE and MSHG. A capping layer of at least six monolayer was found to protect the underlying Co structures from atmospheric contamination for periods of months, while a three monolayer cap provided protection from atmosphere for a period of weeks. The capping layer was also found to greatly enhance the Curie temperature of the Co structures, compared to published measurements of uncapped samples. The samples were grown in UHV conditions using MBE, and the ordering and cleanliness of the preparation procedure was confirmed using LEED and AES.

XMCD was used to determine the orbit-spin moment ratio for six and three atom wide wires capped with 3, 6 and 9 monolayers of Au, and four atom wide wires capped with six monolayers of Au. The experimentally obtained values agreed, within error, with values published for uncapped samples, which suggests that the capping layer had no measurable effect on the orbit-spin moment ratio. XMCD was also used to measure the hysteresis behaviour at a range of temperatures and plots of coercivity versus applied field angle were used to determine the easy axis orientation of the samples. All samples measured were found to have the same easy axis orientation, $\sim$-6° from the surface normal. Since the angle between the surface normal and terrace normal on Pt(997) is -6.4°, it was concluded that the easy axis was aligned with the terrace normal. Published results, where the easy axis angle differed greatly between samples with different Co coverages in uncapped samples, suggests that the contribution of the Au capping layer to the MAE of the samples is responsible for this alignment. The coercivities of the samples were found to have a non-linear temperature dependence, and possible explanations for this were explored. For the three wire samples capped with 6 ML of Au, a super-paramagnetic phase was observed at room temperature, while the sample became ferromagnetic below $\sim$ 160 K. All measured samples showed a temperature dependent coercivity in their ferromagnetic phase. This temperature dependence was consistent with a strong pinning model of domain walls in the samples. A kink in the substrate steps was suggested as a possible pinning site responsible for the temperature dependence. Due to signal to noise issues, only a small amount of data was collected on the two and one atom wide wires. However, remarkably

high Curie temperatures of at least 120 K and 100 K for the one and two atom wide wires, respectively, are suggested. A significant capping layer thickness effect was also observed in the coercivity data, which confirms the expectation that the capping layer thickness will have a large effect on the magnetic properties of the samples below ten monolayers, via the RKKY interaction.

RAS-MOKE measurements were carried out at room temperature on the six and four atom wide Co wires capped with six monolayers of Au. No useful RAS signal was detected from the samples. Field rotation measurements using a quadrupole electromagnet allowed simultaneous measurement of the easy axis, coercivity and stiffness of the samples. The measured easy axis data agreed with that found by XMCD. Significant variations were found between the stiffness measured by MOKE and that found by XMCD. While the coercivity may be affected by differing ambient temperatures between different measurements, the stiffness values are not affected by temperature. As such, the differing stiffness values were attributed to the fact that, while XMCD will measure only the response of the Co atoms, the MOKE effect will include contributions from any induced magnetization in the Au capping layer or the Pt substrate.

MSHG studies were attempted on 6 atom wide Co wires capped with six monolayers of Au. A normal incidence geometry was adopted in order to reduce the number of second order susceptibility tensor components contributing to the signal. However, no magnetic signal was detected. This was attributed to very large 3m crystallographic tensor components overwhelming the magnetic contributions. The strong crystallographic signal was fitted to determine the relative contributions of the tensor components.

MSHG measurements made previously [64] were used to simultaneously fit hysteresis loops and temperature curves to isolate the response of two magnetic regions in a single sample of Fe deposited on vicinal W(110) capped with Au. Unlike the Pt(997)/Co/Au system, only step sites contribute to the crystallographic signal in these measurements, due to the normal incidence geometry and the 2mm symmetry of the terrace sites. Careful selection of the input polarization then allowed for separation of hysteresis loops and Curie curves from different magnetic tensor components, with different contributions from Fe atoms of different symmetries.

In conclusion, RAS-MOKE and MSHG have been shown to have sufficient sensitivity to provide complementary information about capped magnetic nanostructures. RAS-MOKE is particularly well adapted to probing PMA systems, while MSHG works

well for the Au/Fe/W(110) samples, no measurable signal was detected in the Au/Co/Pt(997) system. Capping with a non-magnetic metallic layer has a large effect on the magnetic properties of Co atomic wires, in particular producing a dramatic increase in Curie temperature, which may be of technological importance.

7.2 Future work

While the studies revealed a rich magnetic behavior in the Au-capped Co nanowires, a number of experimental factors prevented the study of the smallest wires, of one or two atom thickness. For the XMCD measurements, signal-to-noise ratios became an issue. While the situation may be improved slightly by the use of thinner capping layers, a better option would be the use of a fast EPU system to allow the use of a lock-in amplifier to greatly improve the SNR. Beamline BL39XU in the Spring-8 facility in Japan currently has such a system, while a similar beamline is planned at Soleil, France. This would allow easy axis and hysteresis measurements to be carried out on the one dimensional single atom wires, which would be of great interest. In terms of extending the existing measurements, Fujisawa *et al.* [57] measured the temperature dependence of the super paramagnetic magnetization curves for a monatomic Fe wire grown on a Au(778) substrate. Fitting of these curves allowed calculation of the spin block size for a range of temperatures, and the resulting temperature dependence was then attributed to one dimensional behaviour. Similar studies could easily be carried out on the Au-capped Co wires. Also, the proposed Gaunt model for the coercivity versus temperature dependence could be tested by extending the range of the data to lower temperatures. Additionally, Gambardella *et al.* [46] measured the easy and hard axis super paramagnetic curves of uncapped Co wires using XMCD to determine the MAE per Co atom for the system. This was not possible due to the magnitude of the field available at ALS and MAXLAB, but would be a useful measurement in the capped system.

In terms of the RAS-MOKE measurements, the main limitation was the magnetic field induced strain signal from the fused silica window of the optical cryostat. The SNR of the room temperature measurements, and the fact that the easy axis in all measured systems is near to the sample surface normal suggests that RAS-MOKE offers the possibility of detailed temperature scans of capped Co nanowires to complement and contrast with the XMCD measurements, if the problem can be solved.

While the SHG measurements of the capped Co wires showed no magnetic signal, it is likely that this is due to the large contributions to the crystallographic signal from the terrace and the capping layer. While it should be possible to produce an isotropic capping layer by increasing the thickness, this would still not remove the terrace contributions, and would reduce the already low SNR in XMCD measurements. A better option would be to explore other measurement geometries in the hope of finding a setup which increased the ratio of the magnetic components to the crystallographic components, such that the magnetic components can be measured. Another alternative is to look at other substrates. If monatomic ferromagnetic wires could be grown on a substrate with 2mm symmetry (like the Fe/W(110) system), then MSHG can provide information unavailable from other techniques due to its symmetry dependence.

In extending the existing measurements, further studies of capping layer thickness of the magnetic properties of the wires would be valuable. Growth of a wedge of Au as a capping layer would allow the effect of very small changes in capping layer thickness to be measured. Temperature dependent measurements in the region of the Curie temperature values are needed, and such measurements may be too time consuming for XMCD measurement. RAS-MOKE combined with a good optical cryostat would be ideal in this instance. Measurement of wires grown on samples with different vicinal offcut angles would also be interesting, as this would give information on the strength of the inter-wire coupling. Also, intentionally introducing higher kink densities in the substrate steps (by, for example, mis-cutting a Pt(997) crystal slightly in the direction parallel to the steps), and measuring the effect on the coercivity at different temperatures could also test the Gaunt model for the temperature dependence of the coercivity. Another possibility is the use of SPEM or spin polarized PEEM to image the domain structure of the thicker wires. This could indicate where the domain walls are being pinned, and also give some information on the inter-wire coupling.

8 Acknowledgments

First of all, I would like to acknowledge the help and support of my supervisors, Prof. John McGilp and Dr. Cormac McGuinness. I would also like to acknowledge the contributions of Daniel McNally, with whom the XMCD measurements were carried out, and Lee Carroll, who conducted the MSHG work on the W(110)/Fe/Au samples. I would also like to acknowledge the help of all the co-workers in the surface science groups in Trinity, past and present: Niall McAlinden, Lina Persechini, Chris Smith, Dr. Nikolaos Peltekis, Dr. Karsten Fleischer, Dr. Julie Jacob and Dr. Sandhya Chandola. I would like to acknowledge the help and support of my girlfriend Michelle, my parents Anne and John, and my family and friends over the course of my thesis work. Finally, I would like to acknowledge the funding from Science Foundation Ireland, and the beamline scientists, Dr. Elke Arenholz and Dr. Marco Liberati at the ALS, and Dr. Iwona Kowalik , Dr. Dmitri Arvanitis and Dr. Matts Björck at MAXLAB.

9 Relevant Publications

J.F. McGilp, L. Carroll, K.Fleischer, J.P. Cunniffe, S. Ryan. Magnetic second harmonic generation from interfaces and nanostructures. *Journal of Magnetism and Magnetic Materials,* v 322, n 9-12, p 1488-1493 2010.

J.P. Cunniffe, D.E. McNally, M. Liberati, E. Arenholz, C. McGuinness, J.F. McGilp. X-ray magnetic circular dichroism and reflection anisotropy spectroscopy Kerr effect studies of capped magnetic nanowire. *Physica Status Solidi B,* v 247, n 8, p 2108-12 2010.

L. Carroll, K. Fleischer, J.P. Cunniffe, J.F. McGilp. Magnetic second-harmonic generation from the terraces and steps of aligned magnetic nanostructures grown on low symmetry interfaces. *Journal of Physics Condensed Matter,* v 20, n 26 2008.

L. Carroll, J.P. Cunniffe, K. Fleischer, S. Ryan, J.F. McGilp. Temperature-dependent magnetic second-harmonic generation from Fe nanostructures grown on vicinal W(110). *Physical review B,* in production.

References

[1] P. Grünberg, R. Schreiber, Y. Pang, M. B. Brodsky, and H. Sowers. Layered magnetic structures: Evidence for antiferromagnetic coupling of Fe layers across Cr interlayers. *Phys. Rev. Lett.*, 57(19):2442–2445, 1986.

[2] M. N. Baibich, J. M. Broto, A. Fert, F. Nguyen Van Dau, F. Petroff, P. Etienne, G. Creuzet, A. Friederich, and J. Chazelas. Giant magnetoresistance of (001)Fe/(001)Cr magnetic superlattices. *Phys. Rev. Lett.*, 61(21):2472–2475, 1988.

[3] J.M.D. Coey. *Magnetism and Magnetic Materials*. Cambridge University Press, 2010.

[4] P. Gambardella, A. Dallmeyer, K. Malti, M.C. Malagoli, W. Eberhardt, K. Kern, and C. Carbone. Ferromagnetism in one-dimensional monatomic metal chains. *Nature*, 416(6878):301 – 4, 2002.

[5] H.J. Elmers. Ferromagnetic monolayers. *International Journal of Modern Physics B*, 9(24):3115–3180, 1995.

[6] H.J. Elmers, J. Hauschild, H. Höche, and U. Gradmann. Submonolayer magnetism of Fe(110) on W(110): Finite width scaling of stripes and percolation between islands. *Physical Review Letters*, 73(6):898–901, 1994.

[7] J. Hauschild, H.J. Elmers, and U. Gradmann. Dipolar superferromagnetism in monolayer nanostripes of Fe(110) on vicinal W(110) surfaces. *Physical Review B (Condensed Matter)*, 57(2):677 – 80, 1998.

[8] M. Pratzer, H.J. Elmers, M. Bode, O. Pietzsch, A. Kubetzka, and R. Wiesendanger. Atomic-scale magnetic domain walls in quasi-one-dimensional Fe nanostripes. *Physical Review Letters*, 87(12):127201 – 1, 2001.

[9] L. Carroll, K. Fleischer, and J.F. McGilp. Optimizing the magnetic contrast in the optical second-harmonic response of capped magnetic nanostructures grown on vicinal surfaces. *Physica Status Solidi C*, 5(8):2645 – 8, 2008.

[10] L. Carroll, K. Fleischer, J.P. Cunniffe, and J.F. McGilp. Magnetic second-harmonic generation from the terraces and steps of aligned magnetic nanostructures grown on low symmetry interfaces. *Journal of Physics Condensed Matter*, 20(26), 2008.

[11] J.F. McGilp, L. Carroll, and K. Fleischer. Extracting the hysteresis loops of magnetic interfaces from optical second-harmonic intensity measurements. *Journal of Physics: Condensed Matter*, 19(39):396002 (13 pp.) –, 2007.

[12] J.F. McGilp, L. Carroll, and K. Fleischer. Determining magnetization curves using optical second-harmonic generation. *Physica Status Solidi C*, 5(8):2653 – 6, 2008.

[13] J.F. McGilp, L. Carroll, K. Fleischer, J.P. Cunniffe, and S. Ryan. Magnetic second-harmonic generation from interfaces and nanostructures. *Journal of Magnetism and Magnetic Materials*, 322(9-12):1488 – 1493, 2010.

[14] J. Thiele, R. Belkhou, H. Bulou, O. Heckmann, H. Magnan, P. Le Fevre, D. Chandesris, and C. Guillot. EXAFS study of the crystallographic structure of cobalt thin films on Pt(111). *Surface Science*, 384(1-3):120 – 8, 1997.

[15] D. Weller, A. Carl, R. Savoy, T.C. Huang, M.F. Toney, and C. Chappert. Structural transitions and magnetic anisotropy in ultrathin Co wedges on Pt(111) investigated with the magneto-optical Kerr effect. *Journal of the Physics and Chemistry of Solids*, 56(11):1563 – 6, 1995.

[16] F. Lopez-Urias, J. Dorantes-Davila, and H. Dreysse. Co ultra-thin films on Pd(111): magnetic anisotropy of the Co/Pd interface. *Journal of Magnetism and Magnetic Materials*, 165(1-3):262 – 4, 1997.

[17] P. F. Carcia, A. D. Meinhaldt, and A. Suna. Perpendicular magnetic anisotropy in Pd/Co thin film layered structures. *Applied Physics Letters*, 47(2):178–180, 1985.

[18] N. Sulitanu. Structural origin of perpendicular magnetic anisotropy in Ni-W thin films. *Journal of Magnetism and Magnetic Materials*, 231(1):85 – 93, 2001.

[19] A. E. Freitag and A. R. Chowdhury. Magnetic properties of Fe/Tb multilayers with large Fe layer thickness. *Journal of Applied Physics*, 85(8):4696–4698, 1999.

[20] K. Hyomi, A. Murayama, Y. Oka, and C.M. Falco. Misfit strain and magnetic anisotropies in ultrathin Co films hetero-epitaxially grown on Au/Cu/Si(111). *Journal of Crystal Growth*, 235(1-4):567 – 571, 2002.

[21] C. S. Shern, J. S. Tsay, H. Y. Her, Y. E. Wu, and R. H. Chen. Response and enhancement of surface magneto-optic Kerr effect for Co-Pt(111) ultrathin films and surface alloy. *Surface Science*, 429(1-3):L497 – L502, 1999.

[22] Y.E. Wu, C.W. Su, F.C. Chen, C.S. Shern, and R.H. Chen. Capping effect in magnetic properties of Ag ultra-thin films on Co/Pt(111). *Journal of Magnetism and Magnetic Materials*, 239(1-3):291 – 3, 2002.

[23] P. Gambardella, S. Rusponi, M. Veronese, S.S. Dhesi, C. Grazioli, A. Dallmeyer, I. Cabria, R. Zeller, P.H. Dederichs, K. Kern, C. Carbone, and H. Brune. Giant magnetic anisotropy of single cobalt atoms and nanoparticles. *Science*, 300(5622):1130 – 3, 2003.

[24] P. Gambardella, M. Blanc, H. Brune, K. Kuhnke, and K. Kern. One-dimensional metal chains on Pt vicinal surfaces. *Phys. Rev. B*, 61(3):2254–2262, 2000.

[25] M. A. Ruderman and C. Kittel. Indirect exchange coupling of nuclear magnetic moments by conduction electrons. *Phys. Rev.*, 96(1):99, 1954.

[26] T. Kasuya. A theory of metallic ferro- and antiferromagnetism on zener's model. *Progress of Theoretical Physics*, 16(1):45–57, 1956.

[27] K. Yosida. Magnetic properties of Cu-Mn alloys. *Phys. Rev.*, 106(5):893–898, 1957.

[28] J. Stöhr and H.C. Siegmann. *Magnetism : From Fundamentals to Nanoscale Dynamics*. Springer, 2006.

[29] P. Bruno and C. Chappert. Oscillatory coupling between ferromagnetic layers separated by a nonmagnetic metal spacer. *Phys. Rev. Lett.*, 67(12):1602–1605, 1991.

[30] D. McNally. X-ray characterisation of capped low dimensional magnetic nanostructures. *Masters thesis, University of Dublin, Trinity college*, 2006.

[31] J. Zak, E.R. Moog, C. Liu, and S.D. Bader. Universal approach to magneto-optics. *Journal of Magnetism and Magnetic Materials*, 89(1-2):107 – 23, 1990.

[32] J. Zak, E.R. Moog, C. Liu, and S.D. Bader. Fundamental magneto-optics. *Journal of Applied Physics*, 68(8):4203 – 7, 1990.

[33] K. Sato. Measurement of magneto-optical Kerr effect using piezo-birefringent modulator. *Japanese Journal of Applied Physics*, 20(12):2403 – 9, 1981.

[34] P. Weightman, D.S. Martin, R.J. Cole, and T. Farrell. Reflection anisotropy spectroscopy. *Reports on Progress in Physics*, 68(6):1251 – 341, 2005.

[35] J. E. Sipe, D. J. Moss, and H. M. van Driel. Phenomenological theory of optical second- and third-harmonic generation from cubic centrosymmetric crystals. *Phys. Rev. B*, 35(3):1129–1141, 1987.

[36] R Shen Y. *The Principles of Non-linear Optics*. Wiley, 1984.

[37] R. Stolle, K.J. Veenstra, F. Manders, Th. Rasing, H. van den Berg, and N. Persat. Breaking of time-reversal symmetry probed by optical second-harmonic generation. *Physical Review B (Condensed Matter)*, 55(8):4925 – 7, 1997.

[38] M. Straub, R. Vollmer, and J. Kirschner. Surface magnetism of ultrathin Fe films investigated by nonlinear magneto-optical Kerr effect. *Physical Review Letters*, 77(4):743 – 6, 1996.

[39] L.E. Davis, N.C. MacDonald, P.W. Palmberg, G.E. Riach, and R.E. Weber. *Handbook of Auger electron spectroscopy*. Physical electronics division, Perkin Elmer corporation, USA, 1976.

[40] R. Baudoing-Savois, P. Dolle, Y. Gauthier, M.C. Saint-Lager, M. De Santis, and V. Jahns. Co ultra-thin films on Pt(111) and Co-Pt alloying: A LEED, Auger and synchrotron X-ray diffraction study. *Journal of Physics Condensed Matter*, 11(43):8355 – 8375, 1999.

[41] M.O. Krause. Atomic radioactive and radiationless yields for K and L shell. *Journal of Physical Chemistry Reference Data*, 8, 1979.

[42] L. Geiger, R. Schertle, F. Durr, and K. Rothermel. Temporal addressing for mobile context-aware communication. *Proceedings of the 2009 6th Annual International Mobile and Ubiquitous Systems: Networking; Services, MobiQuitous. MobiQuitous 2009*, pages 1 –10, 2009.

[43] E. Arenholz and S. O. Prestemon. Octupole magnet for soft X ray magnetic dichroism experiments: Design and performance. *Synchrotron radiation instrumentation: Eighth International Conference on Synchrotron Radiation Instrumentation*, 705(1):1170–1173, 2004.

[44] Z.Q. Qiu and S.D. Bader. Surface magneto-optic kerr effect (SMOKE). *Journal of Magnetism and Magnetic Materials*, 200(1):664 – 678, 1999.

[45] T. Herrmann, K. Ludge, W. Richter, K.G. Georgarakis, P. Poulopoulos, R. Nunthel, J. Lindner, M. Wahl, and N. Esser. Optical anisotropy and magneto-optical properties of Ni on preoxidized Cu(110). *Physical Review B (Condensed Matter and Materials Physics)*, 73(13):134408 – 1, 2006.

[46] P. Gambardella, A. Dallmeyer, K. Maiti, M.C. Malagoli, S. Rusponi, P. Ohresser, W. Eberhardt, C. Carbone, and K. Kern. Oscillatory magnetic anisotropy in one-dimensional atomic wires. *Physical Review Letters*, 93(7):077203 – 1, 2004.

[47] R. Wu, C. Li, and A.J. Freeman. Structural, electronic and magnetic properties of Co/Pd(111) and Co/Pt(111). *Journal of Magnetism and Magnetic Materials*, 99(1-3):71 – 80, 1991.

[48] M. Weinert and A.J. Freeman. Magnetism of linear chains. *Journal of Magnetism and Magnetic Materials*, 38(1):23 – 33, 1983.

[49] P. Bruno. Tight-binding approach to the orbital magnetic moment and magnetocrystalline anisotropy of transition-metal monolayers. *Phys. Rev. B*, 39(1):865–868, 1989.

[50] J. Xu, M.A. Howson, B.J. Hickey, D. Greig, P. Veillet, and E. Kolb. Giant magnetoresistance and super-paramagnetism in Co/Au multilayers. *Journal of Magnetism and Magnetic Materials*, 156(1-3):379 – 380, 1996.

[51] C.J. O'Connor, Y.-S. Lee, J. Tang, V.T. John, N.S. Kommareddi, M. Tata, G.L. McPherson, J.A. Akkara, and D.L. Kaplan. Superparamagnetism of ferrite particles dispersed in spherical polymeric materials. *IEEE Transactions on Magnetics*, 30(6 pt 1):4954 – 4956, 1994.

[52] T. Banert and U.A. Peuker. Preparation of highly filled super-paramagnetic PMMA-magnetite nano composites using the solution method. *Journal of Materials Science*, 41(10):3051 – 3056, 2006.

[53] N.J. Seong, S.G. Yoon, Y.H. Jo, M.H. Jung, C.R. Cho, J.M. Yang, D.J. Park, J.W. Lee, and J.Y. Lee. Intrinsic ferromagnetic properties of $Ti_{0.94}Fe_{0.06}O_2$,

$Ti_{0.94}Mn_{0.06}O2$ superlattice films for dilute magnetic semiconductor applications. *Applied Physics Letters*, 89(16), 2006.

[54] H. Wei, T. Yao, Z. Pan, C. Mai, Z. Sun, Z. Wu, F. Hu, Y. Jiang, and W. Yan. Role of Co clusters in wurtzite Co:ZnO dilute magnetic semiconductor thin films. *Journal of Applied Physics*, 105(4):043903 (6 pp.) –, 2009.

[55] C.A. Stowell, R.J. Wiacek, A.E. Saunders, and B.A. Korgel. Synthesis and characterization of dilute magnetic semiconductor manganese-doped indium arsenide nanocrystals. *Nano Letters*, 3(10):1441 – 7, 2003.

[56] R. Cheng, K.Y. Guslienko, F. Y. Fradin, J. E. Pearson, H. F. Ding, D. Li, and S. D. Bader. Step-decorated ferromagnetic Fe nanostripes on Pt(997). *Phys. Rev. B*, 72(1):014409, 2005.

[57] H. Fujisawa, S. Shiraki, M. Furukawa, S. Ito, T. Nakamura, T. Muro, M. Nantoh, and M. Kawai. Electronic structure and magnetism of one-dimensional Fe monatomic wires on Au(788) investigated with ARPES and XMCD. *Physical Review B (Condensed Matter and Materials Physics)*, 75(24):245423 – 1, 2007.

[58] K.H. Fischer and J.A. Hertz. *Spin glasses*. Cambridge university press, 1991.

[59] P. Gaunt. Ferromagnetic domain wall pinning by a random array of inhomogeneities. *Philosophical Magazine B (Physics of Condensed Matter, Electronic, Optical and Magnetic Properties)*, 48(3):261 – 76, 1983.

[60] F. Wilhelm, M. Angelakeris, N. Jaouen, P. Poulopoulos, E.T. Papaioannou, Ch. Mueller, P. Fumagalli, A. Rogalev, and N.K. Flevaris. Magnetic moment of Au at Au/Co interfaces: a direct experimental determination. *Physical Review B (Condensed Matter and Materials Physics)*, 69(22):220404 – 1, 2004.

[61] F. Wilhelm, P. Poulopoulos, G. Ceballos, H. Wende, K. Baberschke, P. Srivastava, D. Benea, H. Ebert, M. Angelakeris, N.K. Flevaris, D. Niarchos, A. Rogalev, and N.B. Brookes. Layer-resolved magnetic moments in Ni/Pt multilayers. *Physical Review Letters*, 85(2):413 – 416, 2000.

[62] Ru-Pin Pan, H. D. Wei, and Y. R. Shen. Optical second-harmonic generation from magnetized surfaces. *Phys. Rev. B*, 39(2):1229–1234, 1989.

[63] M. Trzeciecki and W Hbner. Group-theoretical analysis of second harmonic generation at (110) and (111) surfaces of antiferromagnets. *Applied Physics B: Lasers and Optics*, 68:473–476, 1999.

[64] L. Carroll. Optical investigations of the magnetic properties of Fe structures grown on W(110). *PhD thesis, University of Dublin, Trinity college*, 2006.